DESIGN AND FABRICATION OF GERMANIUM-BASED GUIDED-MODE RESONANCE INFRARED REFLECTORS AND GOLD-BASED NANOCAVITY PLASMONIC ARRAYS

by

DANIEL JOHN CARNEY

DISSERTATION

Submitted in partial fulfillment of the requirements
for the degree of Doctor of Philosophy at
The University of Texas at Arlington
May, 2019

Arlington, Texas

Supervising Committee:

Robert Magnusson, Supervising Professor
Nader Hozhabri
Michael Vasilyev
Weidong Zhou
Zdzislaw Musielak

DEDICATION

I dedicate this work to my wife, Lucy, and my son, Nathan. It is a parent's duty to provide as much opportunity as they can for their children, and it is the child's job to remind them why it is all worth doing. Whenever I would come home tired and frustrated, he would always be there to make me remember to keep looking forward. There is a saying that behind every successful man there is a strong woman, and here is another example, though I might modify it slightly. Lucy has stood beside me as a source of constant support and inspiration through all the hard work and frustrated nights. She never let me give up, never let me lose sight of my goal, and for that I am grateful.

ACKNOWLEDGMENTS

I would like to thank Dr. Magnusson for all of the time, advice and support he has given me throughout my stay in the Nanophotonics Device Group. Whenever it seemed like I was against a wall in my progress, he would offer his encouragement and insight and would often present a new direction from which to tackle the problem.

I would also like to thank Dr. Lee for his tireless work and support of the group. He is the grease that keeps the gears turning in the lab and is often called upon to assist with more projects than would seem possible for one person to handle. Without his help, much of this work would not have been possible.

This work would also not have been possible without the support of Dr. Hozhabri and his hard-working crew at the UTA nanofab – Mick, Dennis and Kevin. The advice and expertise they offered throughout the development of my fabrication process was invaluable and greatly appreciated.

I would like to thank Professor Svavarsson of Reykjavik University, Iceland, for providing the Au nanocup plasmonic sensors and measurement results used as the groundwork and motivation for the theoretical study presented in Chapter 5.

Lastly, I am thankful for the support and tutelage of my remaining committee members, Dr. Zhou, Dr. Vasilyev, and Dr. Musielak. My courses with them were inspiring and kept me true to the path that I complete now with this work.

ABSTRACT

DESIGN AND FABRICATION OF GERMANIUM-BASED GUIDED-MODE RESONANCE INFRARED REFLECTORS AND GOLD-BASED NANOCAVITY PLASMONIC ARRAYS

Daniel John Carney

The University of Texas at Arlington, 2019

Supervising Professor: Dr. Robert Magnusson

Design, fabrication, and measurement techniques for germanium-based guided-mode resonance infrared wideband reflectors and applications of guided-mode resonance devices for sensing and measurement applications are presented. Germanium is a versatile semiconductor with physical properties similar to silicon but optical properties that make it well suited for the infrared wavelengths. It has a high refractive index and negligible absorption in the mid to far infrared spectral region that can be used to create high field confinement necessary for wideband and high quality factor devices. Fabrication of germanium devices becomes straight-forward once the physical matters of germanium's material bonding properties and surface chemistries are accounted for. Fabrication steps are presented for the deposition of thick germanium films using sputtering or electron beam evaporation methods, patterning the films using lithographic and nano-imprinting, and etching of these films to fabricate a guided-mode resonant or other photonic device. Designs are presented for four archetypal wideband longwave infrared guided-mode resonance reflectors, and the simplest design choice is fabricated as a proof of concept. Additional fabrication techniques are demonstrated with the device that involve depositing an additional conformal layer in order to refine its spectral response. Sputtered germanium films are found to have dynamic refractive index characteristics, and a study is carried out on their optical properties. The optical properties of sputtered germanium films are studied as they are found to vary from a 4% decrease to a 15% increase in their index of refraction over bulk crystalline material depending on the deposited layer thickness. Possible mechanisms driving this variance are discussed, and the refractive index of five separate films is measured and verified using a combination of Fabry-Perot transmission measurements and resonant measurements from guided-mode resonance devices patterned into the films. The material properties of the films are studied using energy-dispersive spectroscopy and x-ray diffraction spectroscopy and are found to indicate that no unexpected material compounds are present in the films that may be contributing to the refractive index shifts. Lastly, a chapter is included studying the resonant properties of plasmonic nano-cavity arrays. The resonant response of an array of gold nanocups is analyzed to discern its physical origin and found to be closely related to research governing the transmission of light through thin metallic films perforated with aperture arrays. The resonant response is determined to be a combination of the interaction of plasmonic modes with evanescent cavity modes within the array.

Table of Contents

TABLE OF ILLUSTRATIONS

LIST OF ABBREVIATIONS

Amorphous germanium – a-Ge
Atomic force microscope – AFM
Crystalline germanium – c-Ge
Deep reactive ion etching – DRIE
Effective medium theory – EMT
Energy dispersive spectroscopy – EDS
Fabry-Perot – FP
Fourier transform infrared spectroscopy – FTIR
Guided-mode resonance – GMR
Infrared - IR
Laser interferometric lithography – LIL
Long wave infrared – LWIR
Nanophotonics Device Group – NPG
Mid wave infrared – MWIR
Near-infrared - NIR
Particle swarm optimization – PSO
Photoresist – PR
Reactive ion etching – RIE
Rigorous coupled wave analysis – RCWA
Scanning electron microscope – SEM
Surface plasmon polariton – SPP
Surface plasmon resonance – SPR
Transverse electric – TE electric-field vector is normal to the plane of incidence
Transverse magnetic – TM electric-field vector lies in the plane of incidence
X-ray diffraction – XRD
1D – One-dimensional
2D – Two-dimensional

Chapter 1 Introduction

1.1 Diffractive optics historical background

The diffraction of light was first described by the Jesuit mathematician Francesco Maria Grimaldi in his work *Physico-mathesis de lumine* in 1666. In his experiments, he observed that light incident on a pinhole would emerge from the other side in a conical trajectory, and that objects placed in the light path would cast shadows containing bands of colored light or would contain feature sizes larger than a simple linear projection of the light path through the aperture would suggest. He coined the term "diffraction" to describe this phenomenon of light bending around a corner. [1]

The discovery of the diffraction grating in which a periodic structure diffracts light into various bands is credited to the Scottish mathematician James Gregory where in a correspondence to the English mathematician John Collins in 1673 he describes the shining of light through a delicate bird's feather as creating, "a number of small circles and ovals…whereof one is somewhat white…and all the rest severally coloured." [2] Since then, the diffraction grating has become a ubiquitous tool used in the scientific community. It has uses in various biological and chemical sensors [3] [4], spectrographic imaging [5], and communications technology [6] [7], among many others.

1.2 Guided-mode resonance

Guided-mode resonance (GMR) is a phenomenon driven by light being diffractively coupled into and out from a laterally oriented optical grating waveguide structure. The waveguide will be made of a high relative index of refraction material placed between a lower index cover and substrate, and can consist of a single spatially modulated index layer, a spatially

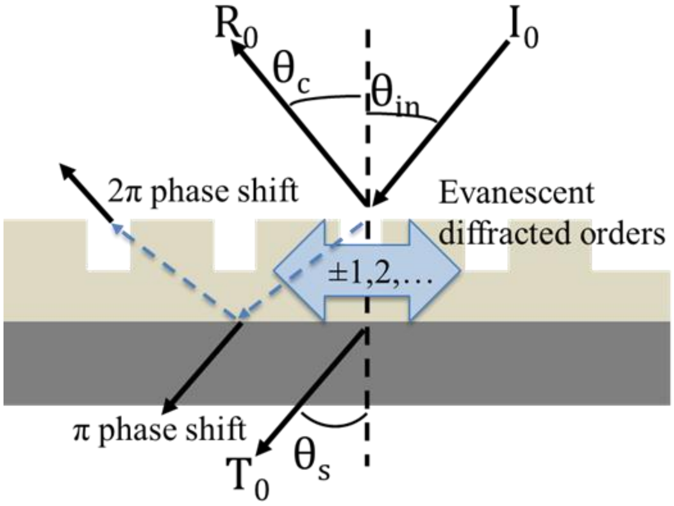

Figure 1.1 - Generic GMR device showing arbitrary angle of incidence and depicting coupled diffractive orders and resonant phase shift conditions.

modulated layer placed in contact with a homogeneous high-index layer, or a combination of multiple modulated and homogenous layers in a one or two dimensional configuration.

The defining principle of GMR is that light is diffractively coupled into waveguide modes within the structure. The shape and spectral location of these modes can be found using classical waveguide theory along with effective medium theory (EMT) to calculate the effective index of refraction of the modulated grating layers. As the coupling is also reversible process, the waveguide modes are often referred to as “leaky” modes which also leads to the term “leaky mode resonance” to describe the effect [8] [9] [10].

The resonance portion of GMR occurs when the outgoing “leaky” waves are phase matched to the incident reflected and transmitted light. A phase shift of 2π on the incident side of the device will cause the re-emitted waves to constructively interfere with the reflected light at the surface and create an enhancement of the reflected intensity. Correspondingly, a π phase shift on the transmitting side will cause destructive interference with the incident light and will diminish the transmitted intensity [11]. By tuning the physical dimensions of the device and the corresponding phase of the coupled waveguide modes, it is possible to create resonant points where 100% of the incident light is reflected.

1.3 Diffractive plasmonic elements

For decades, diffractive elements have begun to take a strong role in the field of plasmonics for use as a coupling mechanism similar to their function in GMR. Surface plasmons are electromagnetic wave surface oscillations that are coupled to the free electron cloud on a metallic substance. Traditional coupling to surface plasmons requires the use of a high-index dielectric material to slow light and momentum match it to a surface plasmon wave. This coupling relies on the evanescent tail of a totally internally reflected wave inside the prism extending out to a metallic surface held in close proximity, or by tunneling completely through a thin metallic layer deposited on the surface of the prism to excite a surface plasmon on the opposing side.

The prism coupling mechanism can be eliminated by introducing a corrugated perturbation directly on the metallic surface. By utilizing the Rayleigh anomaly, the surface corrugation can be tuned such that an emergent diffraction order just grazes the device surface

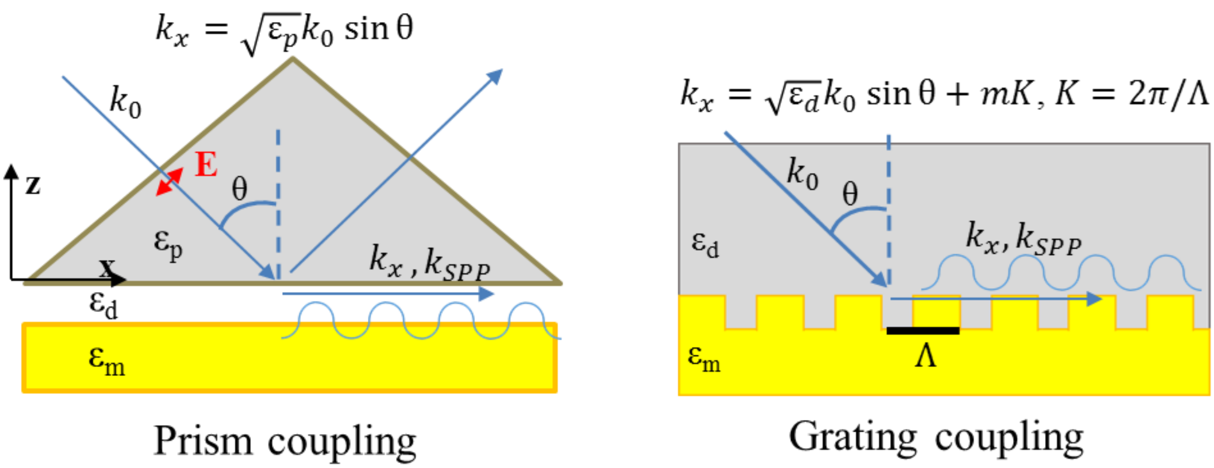

Prism coupling

Grating coupling

Figure 1.2 - Diagrams comparing prism and grating plasmon coupling methods.

and stimulates a surface plasmon. These diffracted plasmons can interact with the surface in various ways including inducing cavity resonances within the modulated structure that ultimately lead to observations such as the “extraordinary transmission” of light through thick perforated metallic films.

1.4 Nanofabrication

Nanotechnology in many ways forms the core of modern society. It is responsible for the diodes that light up the screens in our computers and hand-held devices as well as increasingly the very buildings and environment that we inhabit. It produces the CPU microchips that form the brains of our electronics, and it creates the vast array of sensors, transmitters and receivers that integrate those electronics into our world. Nanotechnology offers the promise of advances in the medical field through innovative cancer treatment and drug delivery techniques, and nanophotonic sensors are used to quickly and accurately detect chemical and biological agents.

Critical to the use and feasibility of all of these technologies is the capability to have them repeatably and reliably fabricated. The history of micro and eventually nanofabrication goes back to the 1960s with the creation of the first small-scale integrated circuits, and the same basic techniques used to create those early devices are still in use and being continually refined today. They include methods for thin film deposition using bottom up procedures such as oxidation growth or top down approaches such as ion sputtering and electron beam evaporation, pattern transfer using techniques such as UV photolithography or electron-beam lithography, and device etching methods using either wet chemicals or reactive ion plasmas. The push for new capabilities in this field also leads to a feedback cycle where increased refinements result in the ability to realize novel device designs than in turn inspire researchers to create even more refined techniques to lead to their continued improvement. In this way, the field of nanofabrication is constantly evolving to adapt to the demands of an ever increasing field of research.

Chapter 2 Germanium device fabrication

2.1 Introduction

The infrared (IR) wavelength spectrum spans from the near-IR (NIR) at 800 nm to around 1 mm in the tail end of the far infrared (FIR). Two important bands for remote sensing purposes are the mid-wave IR (MWIR) spanning from 3 to 8 μm and the long-wave IR (LWIR), also sometimes known as thermal IR, spanning from 8 to 15 μm. The importance of these bands is illustrated in Figure 2.1 [12] showing atmospheric optical transmission characteristics, where specifically the 3 – 5 μm and 8 – 13 μm bands demonstrate low atmospheric absorption and relatively high optical transparency. Photonic devices developed to function in these bands can serve in an array of long range sensing applications such as night vision and thermal imaging, satellite imaging, and emerging light detection and ranging (LIDAR) technologies that will eventually guide autonomous and self-driving vehicles.

The fabrication of IR photonic devices straddles the realm between the micro and nano scale, and relies on overlapping techniques used in both areas. Challenges arise in adapting existing processes and procedures developed for materials used in visible and NIR photonics, such as silicon, silicon dioxide, or titanium oxide, to materials suited to the IR spectral range

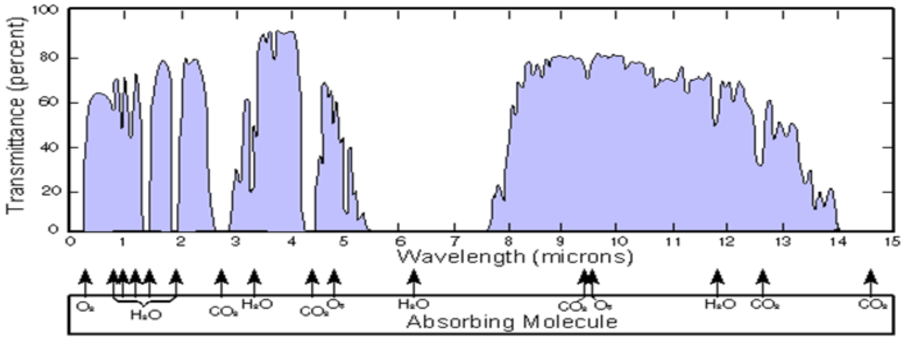

Figure 2.1 - Atmospheric optical transmission characteristics [12].

such as germanium, zinc ceramics, fluoride compounds and chalcogenide glasses. The change in scale from nano to micro photonic devices also necessitates a reevaluation of the fabrication techniques involved as while some will function with minor modifications, others will fail entirely due to physical equipment limitations. The techniques presented here have been demonstrated through repeated experimentation to offer robust solutions to the fabrication of IR scale photonic devices, and serve at stepping stones towards future work in the field. All processes developed here have been designed for use in equipment contained in the Shimadzu Institute Nano Technology Research Center (UTA nanofab) and the Nanophotonics Device Group (NDG) cleanroom.

2.2 Material selection

The first step in the design and fabrication of an IR resonant device is proper material selection. For a GMR element, the key requirement is having a high-index waveguide layer sandwiched between a low-index cladding in order to provide field confinement. While an ideal device might consist of a high-index membrane suspended in air, fabrication constraints often make this impractical which results in the more common design of a high-index material film being deposited on a low-index substrate. The design of high-efficiency GMR reflectors also requires that the materials involved be lossless, or at least nearly so, as any absorption present will translate directly to a decrease in reflection efficiency.

The search for suitable IR materials then falls into a meeting of two general optical requirements followed by a third involving processing and environmental considerations. The first two are the material’s index of refraction, desired to be high for guiding layer materials and low for cover and substrates, and optical absorption characteristics in the desired band. The third requirement examines the material toxicity, fabrication capabilities, and the final operational environment to determine appropriateness for use.

Figure 2.2 displays the index of refraction for several common IR materials [13] [14] [15] [16] [17] [18] [19] [20]. For the scope of designs considered in this work, materials were only considered which would cover the entire MWIR and LWIR bands and would be suitable for processing in the UT-Arlington nanofabrication facilities.

An initial look at the refractive indices would suggest that the fluoride compounds would make for excellent low-index substrates. However, transmission data for CaF shown in Figure 2.3 a) indicates drastic losses after 8 µm, making it unsuitable for the LWIR. SrF_2 (not shown) demonstrates a similar response with its transmission dropping after 10 µm. The next suitable substrate material pairings are the zinc-blend compounds, ZnS and ZnSe. These have higher

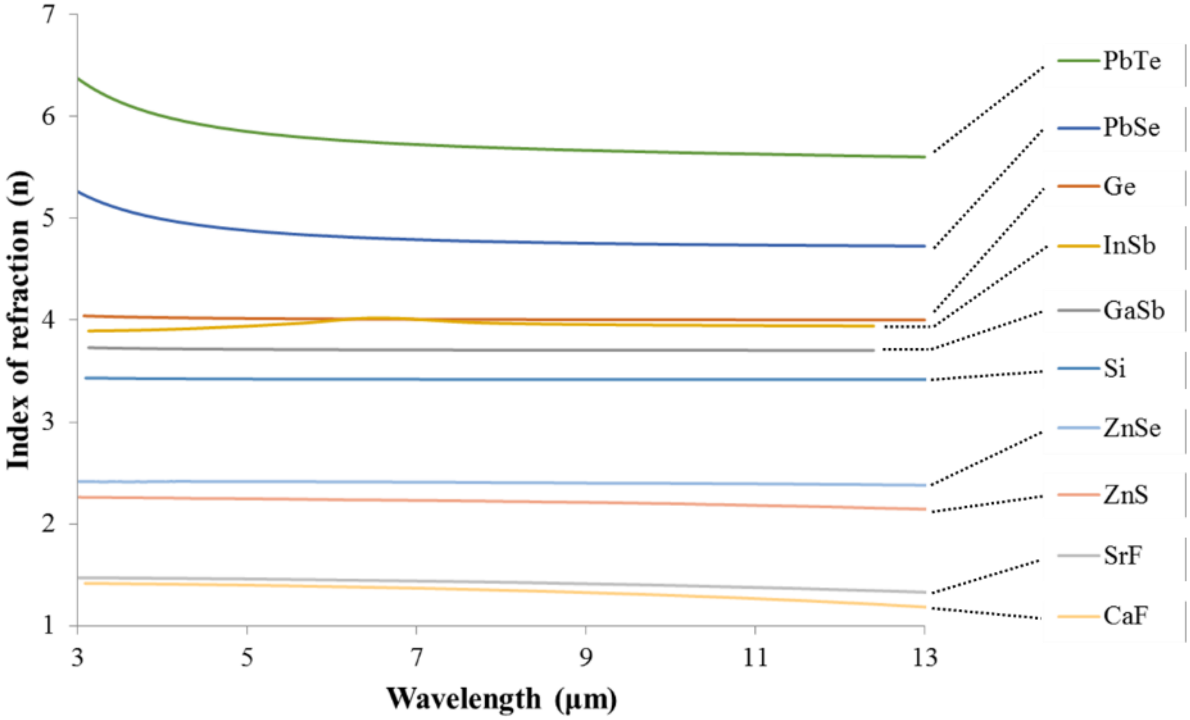

Figure 2.2 - Index of refraction for assorted IR materials [13] [14] [15] [16] [17] [18] [19] [20].

indices of refraction than CaF or SrF_2, but an examination of their transmission curves in Figure 2.3 b) & c) shows that they maintain transparency across the entire MWIR and LWIR. ZnS does start to show losses after 12 μm, but its suitability in the primary 8 to 12 μm atmospheric transparency window along with its lower index of refraction than ZnSe makes it a prime candidate for use as a device substrate. Additional benefits of ZnS include its material robustness which allows it to withstand fabrication processing steps along with a variety of operational environments.

The next step in material selection is finding a suitable high-index device layer material. Turning to the top of the list in Fig. 2.2, the lead compounds PbTe and PbSe offer very high-index values that would be ideal for highly confining waveguides with relatively thin device layers. These materials are also direct bandgap semiconductors with gap energies of 0.32 eV and 0.27 eV, respectively, corresponding to photon freespace wavelengths of 3.82 and 4.59 μm. These two materials already find use in IR photodetectors [21], and may offer further potential for photoelectric resonant devices. However, they have a strong drawback in regards to their high toxicity that would necessitate additional levels of processing and handling precautions. These complications would preclude their use in the available fabrication facilities, and as a result they were not selected for use in this work.

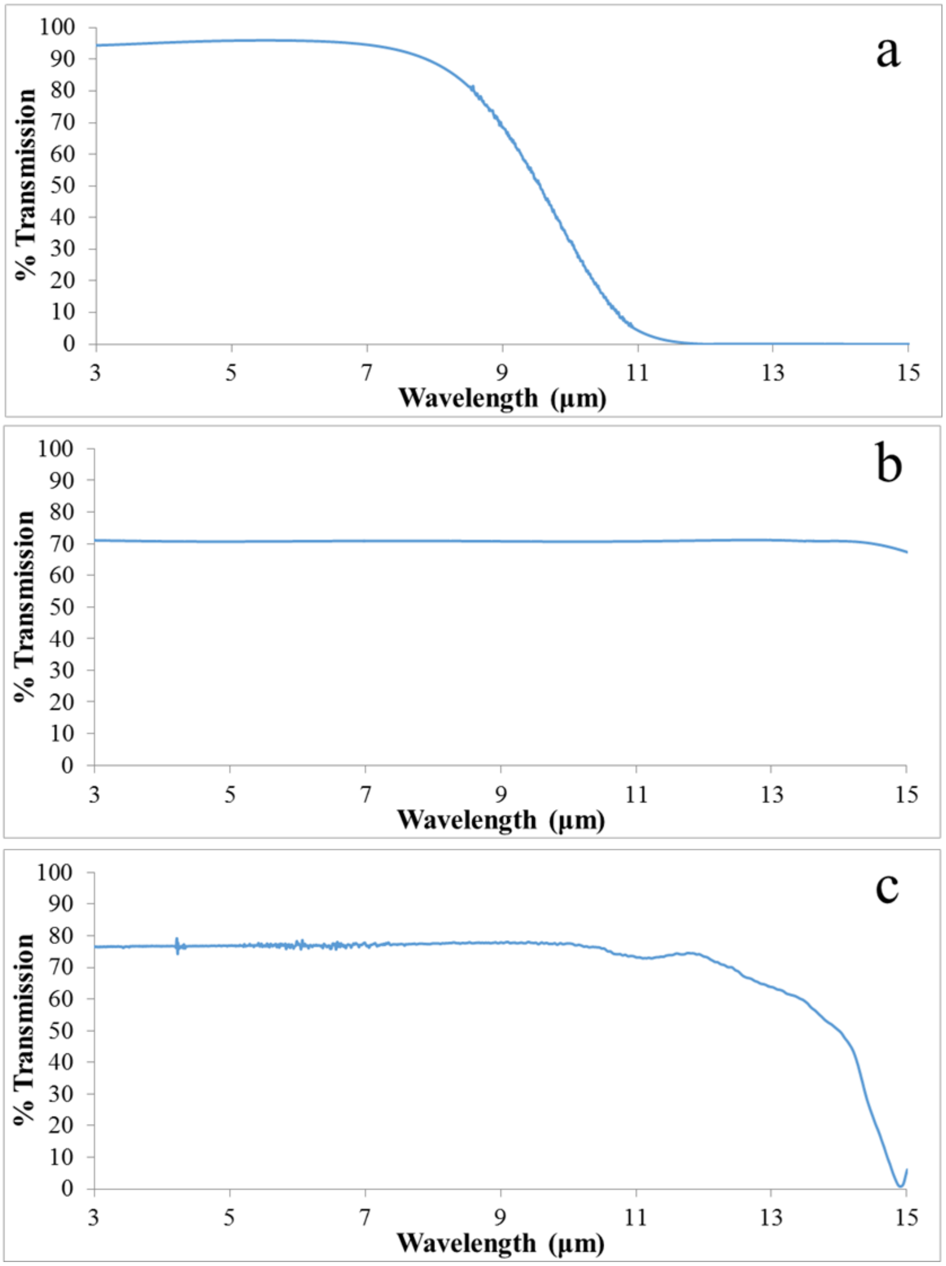

Figure 2.3 - Transmission curves for a) CaF, b) ZnSe, and c) ZnS. CaF and ZnSe data provided by www.thorlabs.com. ZnS data is from a 1mm thick window measured via FTIR.

As stated, the ideal device material has a high-index for mode confinement, but also requires a minimal amount of additional handling and processing precautions. This would allow the material to be used in the widest array of laboratory environments and would facilitate the greatest ease of fabrication and experimentation. In this regard, both silicon and germanium would seem to offer the greatest potential, and indeed, both are currently widely used in IR applications. Silicon processing at this point is also an extremely mature technology with a vast array of techniques at its disposal. Silicon also already sees use in many NIR photonic applications where it can be paired with low-index SiO_2 to create high quality factor devices. However, moving into the mid and long wave regimes necessitates the abandoning of quartz as a substrate due to its high IR absorption. The use of higher index ZnS requires the use of a higher index device layer in order to maintain field confinement, which is especially important in cases of wideband devices where multiple mode orders will be present within the device.

With this constraint in mind, germanium becomes the primary candidate for consideration in device design. Historically, germanium was the first semiconductor to be used in the fabrication of a transistor stemming from a drive to create higher resolution radar systems in the 1940s [22]. It was soon supplanted largely by silicon for transistor fabrication due to its increased stability and versatile oxides, but germanium has seen a resurgence in recent years in the field of photonics. It has been used to grow optical wires [23], improve the efficiency of IR solar cells [24] [25] [26], and in the fabrication of photodiodes [27] [28], photodetectors [29], and anti-reflective (AR) surfaces [30].

Due to its high-index and optical transparency, germanium has also seen extensive application in the mid-wave infrared [31] [32] [33] [34]. It is the next highest in index of refraction after the lead compounds, and, as it shares the same elemental group with silicon, it also shares similar chemistry, which allows for the transfer of many of the same processing techniques with only slight modifications. It also shares silicon's relative inertness and safe handling attributes, making its use in the lab a straight forward matter. Lastly, as proof of its applicability, germanium is already widely used in thin-film coatings and IR windows in the mid and long wave IR [35] [36].

2.3 Film deposition

Thin-film deposition is achieved through a variety of existing technologies depending on the desired application. Most techniques involve a form of physical vapor deposition (PVD), where source material is released by some means into a vacuum chamber where it then deposits onto a substrate. A few of the available options include thermal and electron-beam (e-beam) evaporation where molten material held in a boat or crucible releases particles in a cloud into the vacuum chamber which then thermally condense on the target substrate, DC or RF magnetron sputtering where plasma formed from an inert gas such as argon is used to physically bombard a target surface to eject atoms and deposit them on the substrate, and pulsed laser deposition (PLD) where a focused laser beam is used to eject source material into a plasma stream that condenses on the substrate surface. Sputtering deposition variations can include ion-assisted deposition where a secondary ion beam is directed towards the substrate in order to increase the implantation energy of the deposited material, and reactive sputtering where elements such as oxygen are introduced into the chamber in order to combine with the sputtered material and form a layer of the compound substance. Compound evaporation is also a possibility in chambers equipped with multiple crucibles able to be run simultaneously.

Chemical vapor deposition (CVD) is another general technique that utilizes the breakdown of volatile chemical precursors to deposit a very pure layer of desired material. CVD is often used in situations where a highly conformal layer is desired or for very thin films only a few atomic layers in thickness. Variations on CVD include thermal CVD where only the substrate is heated to induce the breakdown of the precursor and material deposition, and plasma-enhanced CVD (PECVD) where plasma is used to enhance the reaction rate.

For the body of this work, two methods are studied and applied for the deposition of germanium films: e-beam evaporation and RF sputtering. The two methods each bring their own advantages and disadvantages, and the method chosen may vary between different applications.

2.3.1 E-beam evaporation

Electron-beam (e-beam) evaporation is accomplished using the e-beam evaporator solution in the UTA nanofab. This is an automated system that provides for rapid film growth with deposition rates tested as high as 6 Å/s while requiring minimal user input after the initial deposition parameters are set. The evaporation chamber provides for fine control over the deposited film thickness via a deposition monitoring crystal. However, this lifetime of a single crystal was found to be limited to an average of 2.6 µm of film growth. Growing a film of greater thickness is possible, but requires opening the chamber to install a new crystal and results in distinct boundary layers forming within the film.

The e-beam evaporation process begins with thorough cleaning and surface preparation of the ZnS substrate. The ZnS substrates are cleaned of any surface particles or minor organic contaminants with a 15 minute ultrasonic bath immersed in acetone followed by a 15 minute ultrasonic bath immersed in isopropanol followed by a final 15 minute ultrasonic bath in DI water. The ZnS wafer is then rinsed under a flowing DI water stream and dried using compressed N_2. After drying, the wafer is placed on a 115^0 C hotplate for 60 seconds for a dehydration bake. The cleaned and dried wafer is then processed with a surface preparation step prior to film deposition.

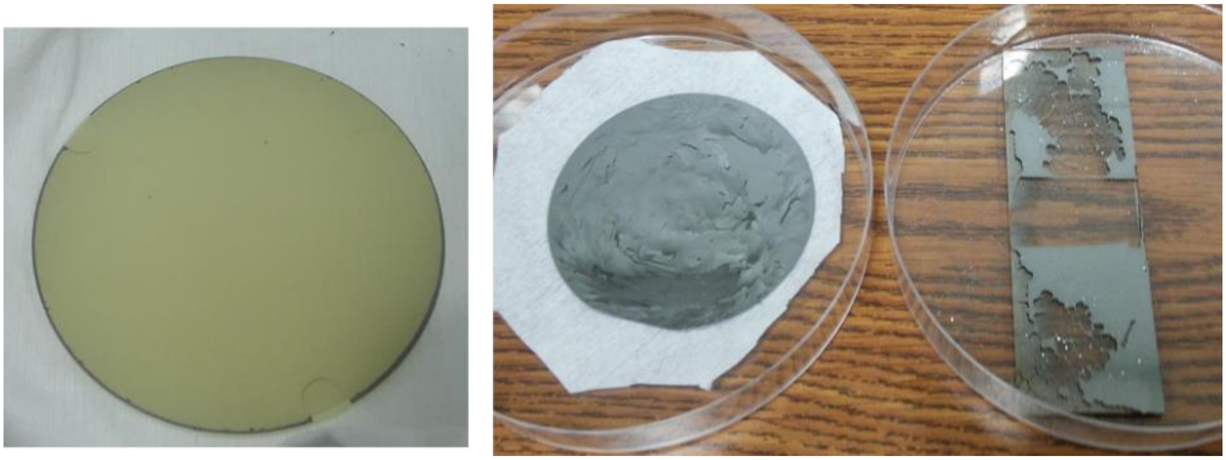

Figure 2.4 - Examples of film delamination due to inadequate surface preparation.

The purpose of the surface treatment is to address severe adhesion issues that were observed during initial testing where the evaporated films would fracture and delaminate from the ZnS surface when immersed in liquid or placed under thermal shock such as a hot plate as shown in Figure 2.4. These issues were addressed with the inclusion of two surface preparation steps.

The first step is to plasma treat the cleaned and dried wafer in the reactive ion etching (RIE) chamber by holding it under argon plasma at 200W for 120s. This step was inspired by papers demonstrating atomic-scale pitting that would occur with such treatment [37]. The surface irregularities created provide for additional binding sites and promote adhesion of the deposited layer, but are small enough (on the order of single nanometers) to have negligible effects on the IR wavelengths. Various other studies have also shown the benefits of plasma treating a substrate prior to deposition, with the role responsible for adhesion promotion being surface activation of molecular bonds [38] and the previously mentioned topological changes.

Another common step for adhesion promotion in the deposition of thin films is the inclusion of a metallic adhesion layer, often Ti or Cr. While this step suffices for semiconductor devices, the inclusion of a metallic layer would potentially interfere with optical device performance by introducing reflection and absorption losses. In place of metallics, a thin layer of Ge sputter deposited onto the substrate was found to provide the necessary additional adhesion for the evaporated films.

Sputtering produces atoms with kinetic energy an order of magnitude higher than the evaporation process, typically 1-10 eV in sputtering versus 0.1 eV for evaporation. This results in higher implantation energies and more densely packed films than are possible through thermal evaporation. The increased implantation energies result in enhanced adhesion to the underlying substrates. For the devices using e-beam evaporation as the primary deposition tool, it was found that a 20 – 40 nm layer of sputtered Ge combined with the prior Ar plasma surface treatment resulted in full adhesion of the subsequently evaporated layer. The use of Ge as the adhesion layer also eliminated the optical difficulties that would be presented if a metallic layer were used. The adhesion layer is deposited using the homebuilt sputter system in the UTA nanofab using a 75 W plasma and 3.5 mT process pressure for 300 s resulting in an approximately 40 nm sputtered layer.

After the surface preparation, the remaining Ge layer is evaporated as normal. Figure 2.5 shows the results of the evaporation process for a single layer 2 μm film and a two layer 4 μm film. In the 4 μm sample, the boundary layer is clearly visible where the deposition process had to be interrupted by opening the vacuum chamber to change out the deposition monitoring crystal. For the two-part deposition, it was found that adhesion was not a concern for the second layer, and no additional action was necessary between the two evaporations.

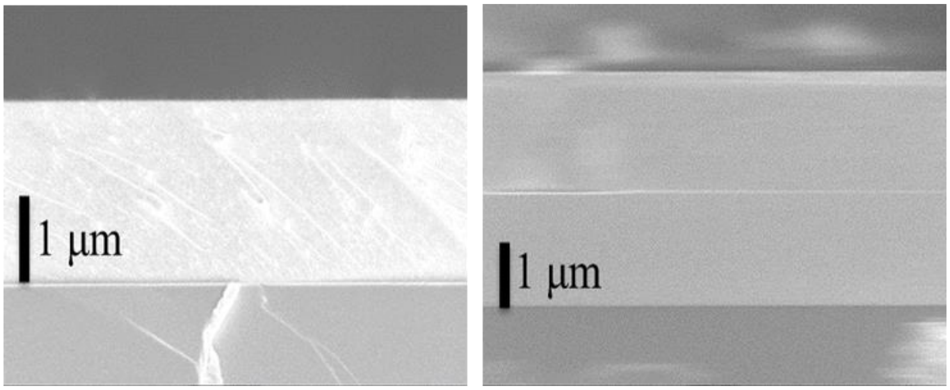

Figure 2.5 - Single and double layer evaporated films.

2.3.2 RF sputter deposition

RF sputtering is another common method of thin film deposition and two different variations were examined in the course of this work. Sputter chambers can be found in two general configurations: top-down, where the target containing the material to be sputtered is held above the substrate stage, and bottom-up with the reverse configuration. This differs from evaporative processes where only the bottom-up configuration is possible.

Initial sputtering tests were accomplished using the UTA nanofab homebuilt sputter chamber with a top-down configuration. Thermal stress was a significant issue in initial tests run at 200 W process power. Films grown at this rate were found to be limited to 300 to 400 nm in thickness before thermal strain in the film would cause it to fracture and delaminate completely from the substrate. Lowering the process power significantly to 70 W was found to mitigate this issue and allow growth of films up to 800 nm. At this point, a second issue was encountered involving the sputter chamber electrodes.

During normal operation, sputtered material will gradually and unavoidably build up on the electrode surrounding the sputter target, and the adhesion of this sputtered material becomes a limiting factor in the maximum film thickness that can be deposited. In the case of the homebuilt system, it was found that after approximately 800 nm of film deposition, the accumulated material would delaminate from the electrode and release into the vacuum chamber. Due to the top-down configuration, this material will rain down onto the deposition sample, generally ruining it for use. This delamination can be mitigated somewhat by scouring the electrode surface with an abrasive pad to remove previously deposited material followed by DI water rinse and thermal dehydration bake prior to use, but even with these steps, 800 nm was the maximum found to be able to be reliably deposited.

Using this method, a 4 μm film was deposited in a five step process by meticulously cleaning the electrode between each deposition. Process parameters for each deposition are 75 W process power, 120s pre-sputter time, 3802s sputter time, 3.5 mT process pressure, 40 mT strike pressure, 15 rpm stage rotation and $2x10^{-6}$ mT initial pump down. While the process did successfully produce the desired film thickness, the multiple steps were ultimately determined to be too unreliable and impractical for use.

A second option investigated was the Kurt-Lesker Lab18 sputter system. This equipment has the advantage of being loaded with multiple targets to allow multi-layer film deposition and has a load-lock for sample loading which allows for faster processing times. This system also uses a bottom-up configuration which results in a lower deposition rate, but carries the advantage that in the event of an electrode failure, any loose material will fall back on the sputter target and not the deposition sample.

Extended depositions at high power resulted in similar electrode delamination issues as were seen with the homebuilt sputter system. In the case of the Lab18 bottom-up configuration, the flakes of material were found to fall between the electrode and target surface resulting in a short circuit and quenching the plasma. While this would prematurely end the process, any

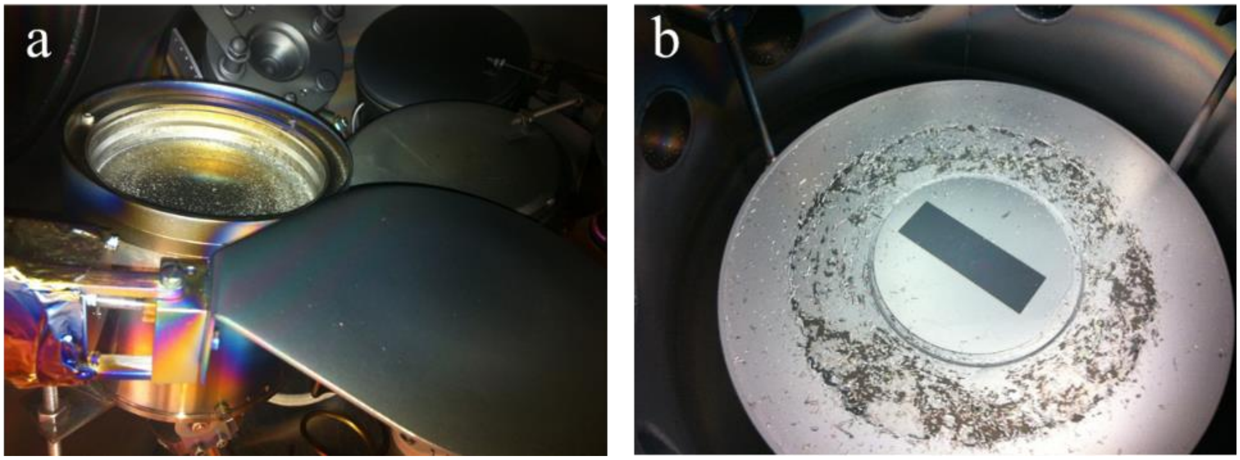

Figure 2.6 – Sputter chamber failure examples. a) delamination from electrodes in Lab18, b) debris from delamination in the homebuilt sputter chamber.

samples in the chamber were largely unaffected and could generally be salvaged. Figure 2.6 shows examples of adhesion failures within the sputter chambers. Fig. 2.6 a) shows a picture of the Lab18 target where the flaked off material is covering the target and electrode surfaces, and Fig. 2.6 b) shows an example of the problems associated with the top-down homebuilt system.

The delamination issue in the Lab18 chamber was mitigated using a combination of techniques. Lowing the process power to 150 W proved sufficient to allow for a one step 4 µm deposition, but the electrodes would fail and require cleaning after at most two such depositions. A step found to be most effective in extending the life of the electrodes was to have them arc sprayed with a metallized coating. This process creates a durable and roughened surface that promotes adhesion of the sputtered material and prevents premature failure. This technique was proven to allow for several extended depositions with a minimal amount of material delamination and no interrupting of the deposition process.

Figure 2.7 displays the results of both methods of sputter deposition. In Fig. 2.7 a) the results of a five-part deposition using the homebuilt sputter system are shown where the bands of material resulting from the separate depositions are clearly visible. In Fig. 2.7 b) the results of a single 4 µm deposition using the Lab18 system is shown along with a patterned photoresist grating on top of the film. In this case, the uniformity of the film is clearly evident.

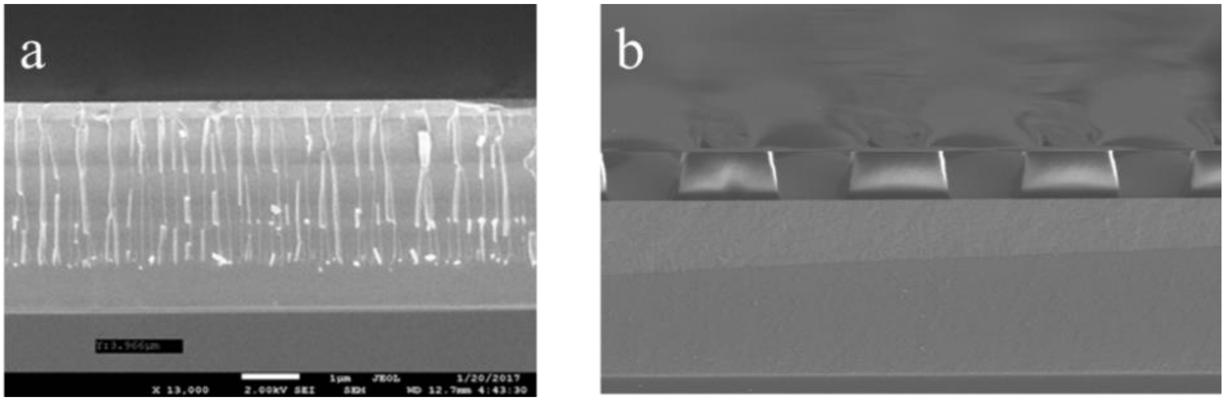

Figure 2.7 – 4 µm Ge films. a) 4 µm film deposited in five 800 nm steps using the homebuilt sputter chamber. b) 4 µm film deposited in a single step using the Lab18 bottom-up system with a patterned photoresist grating on top of the film.

2.3.3 Surface passivation

A final deposition step is used to passivate the germanium surface and to promote adhesion of the photoresist mask. Initial patterning experiments demonstrated adhesion issues between the photoresist pattern and the bare germanium films. Additionally, it was found that untreated films would begin to develop a cloudy oxidation layer on the surface that likely contributed even more to the adhesion problem as germanium oxide is a weakly water-soluble compound.

The issue was resolved with the deposition of approximately 10 nm of silicon on top of the germanium films using the Lab18 sputter system. This film encapsulates the germanium, preventing growth of the germanium oxidation layer, and the s1813 photoresist used in the patterning process readily adheres to the silicon film with no additional processing steps. Numerical simulations demonstrate that this thin Si layer also has a negligible impact on device performance. Figure 2.8 displays the effects of using the silicon coating. Figures 2.8 a) & b) show the adhesion results of a photoresist pattern without and with the Si coating, and Fig. 2.8 c) shows simulation results demonstrating the minor spectral impacts.

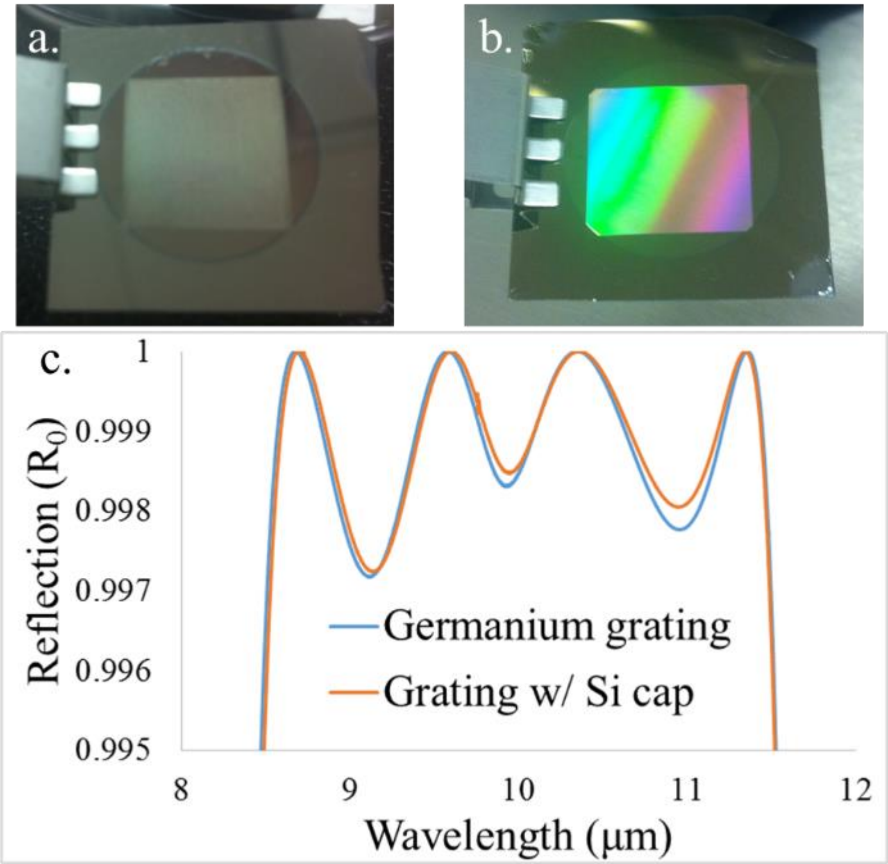

Figure 2.8 - Impacts of Si passivation layer. a) Patterned photoresist on a bare Ge film showing loss of pattern due to loss of adhesion. b) Patterned wafer employing 10 nm Si coating demonstrating excellent photoresist adhesion. c) Spectral comparison between a coated and uncoated device.

2.4 Pattern transfer

The next step in the fabrication process is the application of an etch-resist mask to the film surface. These masks can be in the form of a hardened material such as chrome or aluminum, or a polymer based soft resist. The general process for either begins with coating the surface with a material that can be induced into a state change to allow the selective removal of the resist in desired areas to expose the material underneath to be patterned. This state change is commonly induced via exposure to UV radiation, though demand for higher resolution and smaller feature sizes has pushed the development of electron-beam and even x-ray exposure techniques.

For hard masks, the resist development step is followed by a deposition-liftoff step where the mask material is deposited over the resist patterned surface, and then the metal coated resist is removed generally through the use of a solvent, leaving behind the metallic hard-mask. These masks are useful for deep etches where selectivity between polymer based resists and the etched material would not be sufficient.

2.4.1 EVG-620 contact photolithography

Mask aligner systems were among the first developed photolithography techniques and work well for features generally larger than 1 μm. They function through a one-to-one transfer of a pattern by shining light through a metallic mask patterned on a glass or quartz substrate and held in contact or close proximity to the photoresist surface. These systems usually employ mercury arc lamps to produce g (436 nm), h (405 nm), and i (365 nm) line exposure wavelengths, either all at once or in combinations using UV filters. As these systems do not employ any beam shaping optics, their effective resolution is strongly limited by diffractive effects and the contact quality and alignment between the mask and film surface.

For the devices studied in this work, an EVG-620 mask aligner system is used for the photolithography step. The light source is an Hg arc lamp containing the full g, h, and i-line spectrum. The system accepts either 5 or 7 inch masks; for this work a 5” mask is used. The photoresist used is Microposit s1813 which is sensitive to the entire g, h, and i-line spectrum.

The process begins with spin coating the wafer with s1813 photoresist. The speed and time required depend on the desired final photoresist thickness. After the initial spin coating, a lower speed edge-bead removal step is required as outlined in Fig 2.9. The wafer is spun at a reduced speed while a stream of solvent is sprayed on the edge of the wafer to wash away the bead of photoresist formed due to tensile forces. If this bead is not removed, an air gap will be formed during the following contact expose step which can cause diffractive distortion of the exposed pattern. After spin-coating and edge-bead removal, the wafer is soft baked at 115^0 C for 60 s to evaporate any remaining solvent.

The mask aligner accepts a minimum 4” wafer size, and as the samples worked with are generally much smaller than this, a carrier wafer with a developed photoresist pattern is fabricated that will serve as a placement template for the device samples. The template is prepared in a similar manner to a sample piece, only during the spin-coating step edge-bead removal is not necessary as a precise pattern transfer is not needed. After exposure and development, the general pattern of the photomask will be transferred to the carrier wafer and can then be used as a placement guide for sample pieces.

Once the carrier wafer is prepared, exposure tests need to be run to find the optimal exposure energy. A series of test samples are exposed over a range of energies in order to determine the minimum amount necessary to cleanly expose the pattern without overexposure.

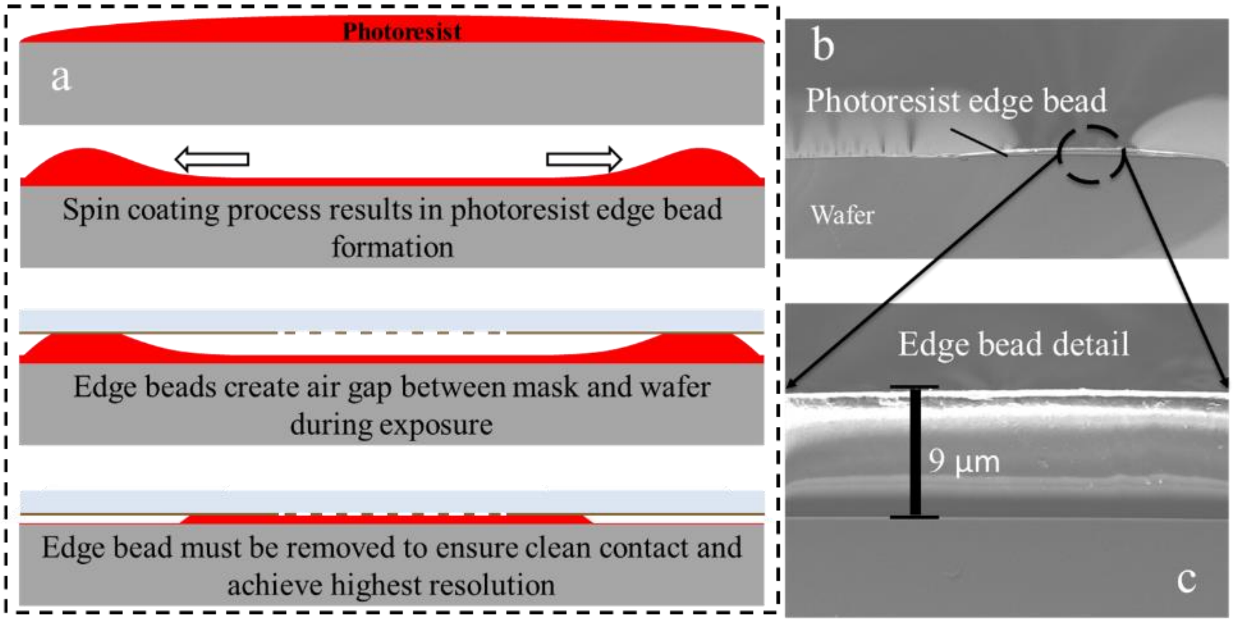

Figure 2.9 - Edge-bead formation and removal. a) spin-coating and contact exposure procedure. b) edge bead formed at the edge of the wafer. c) detailed view of the edge bead.

For the s1813 photoresist spun at 4150 rpm, the optimal energy was found to be 74 mJ/cm^2 as set in the EVG-620 system control software.

After exposure, the samples are post-exposure baked at 115^0 C for 60s to smooth any minor irregularities in the line patterns. The photoresist is then immersed in room temperature MF-321 developer for 60 s, rinsed in DI water and dried with N_2. The developed wafers can then be hard-baked at 115^0 C for an extended amount of time if desired to help harden the resist and increase the etch selectivity.

2.4.2 Diffractive double exposures

In the previous section, the removal of the edge-bead formed during the spin coating process was described as an integral part of the photolithography process. In this section, a technique is described that uses the edge-bead to create a higher resolution pattern than would ordinarily be possible with a contact aligner system.

The underlying impact the edge-bead has on contact photolithography is the air gap it creates between the mask and film. The gap creates room for diffracted light to propagate after exiting the mask, and depending on how the gap impacts the misalignment, the diffracted light can interfere across the gratings causing the formation of additional ridges and valleys, or the interference can run parallel to the gratings causing periodic islands of photoresist to remain inside the channels. Figure 2.10 shows examples of the sort of interference that can occur.

Although the diffractive interference is generally an undesirable effect, it is possible to tune the height of the edge-bead and resulting air gap such that the diffracted light constructively interferes exactly in the center of the grating ridge such that the spatial frequency of the

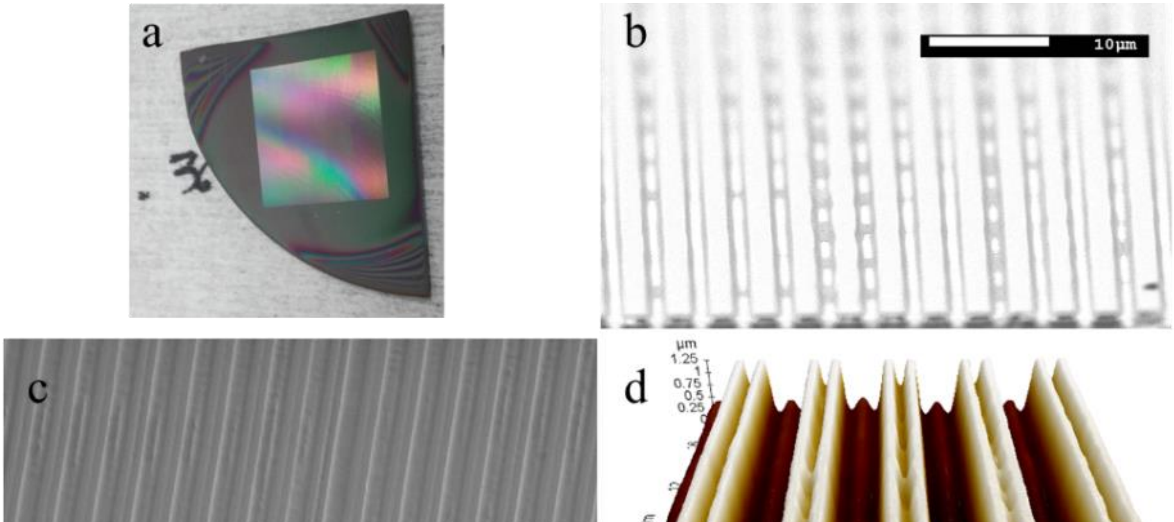

Figure 2.10 - Diffractive defects due to edge-bead induced misalignment. a) Si wafer with distorted exposure pattern. The edge-bead is apparent by the Fabry-Perot bands along the edges which indicate rapidly changing photoresist thickness. b) Diffractive interference parallel to the grating lines resulting in periodic indentations, c) & d) SEM and AFM images of the results of interference running perpendicular to the grating causing extra ridges and valleys in the pattern.

developed pattern becomes effectively doubled. This effect is geometry dependent and does require enough starting fill factor to allow for the formation of the secondary grating row.

Figure 2.11 shows exposure simulations at 436 nm exposure wavelength with and without an air gap present, and using a mask grating with a 0.66 fill factor, period Λ = 3.67 μm, and 1.2 μm photoresist thickness. Figure 2.11 a) is a field intensity simulation with no air gap. In this case, the exposure energy is concentrated along the edges of the image in line with the mask openings. In Fig. 2.11 b) the exposure is simulated using a 2.5 μm air gap between the mask and photoresist surface. In this configuration, the simulation shows diffracted energy is concentrated in the center of the image in the shadow region beneath the mask in addition to the mask openings along the edges.

Experimental verification of this effect is shown in Figure 2.12 with the results of an exposure using s1813 photoresist, a mask with the same dimensions as in the simulations, and exposure energy of 74 mJ/cm^2. Figure 2.12 a) is an AFM scan of the developed photoresist grating with a 3.67 μm period formed by contact exposure with the edge-bead removed resulting in no air gap. It is compared to Fig. 2.12 b) which is an AFM scan of a grating formed with the

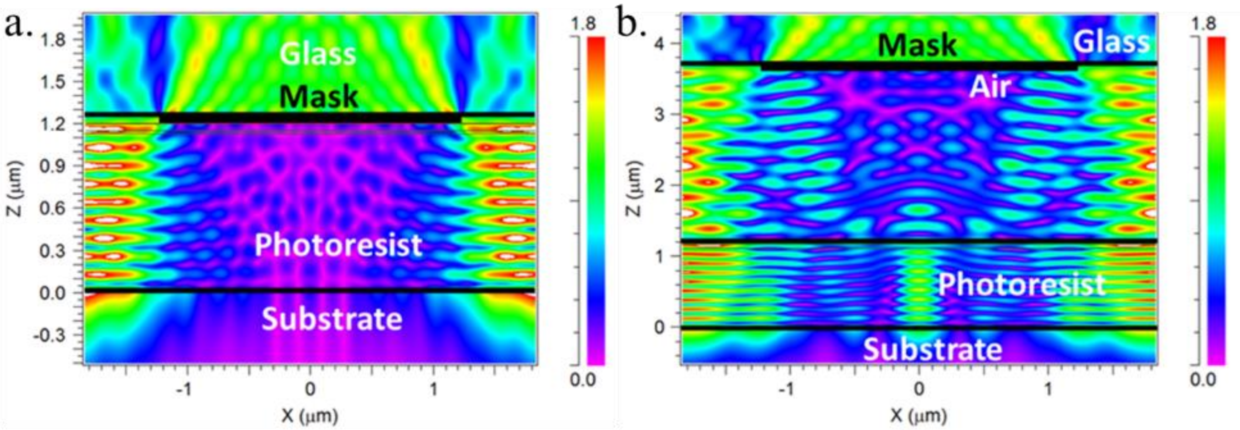

Figure 2.11 - Exposure simulations. a) 436 nm exposure field concentration with no air gap present. b) exposure simulation using a 2.5 μm air gap between the mask and surface.

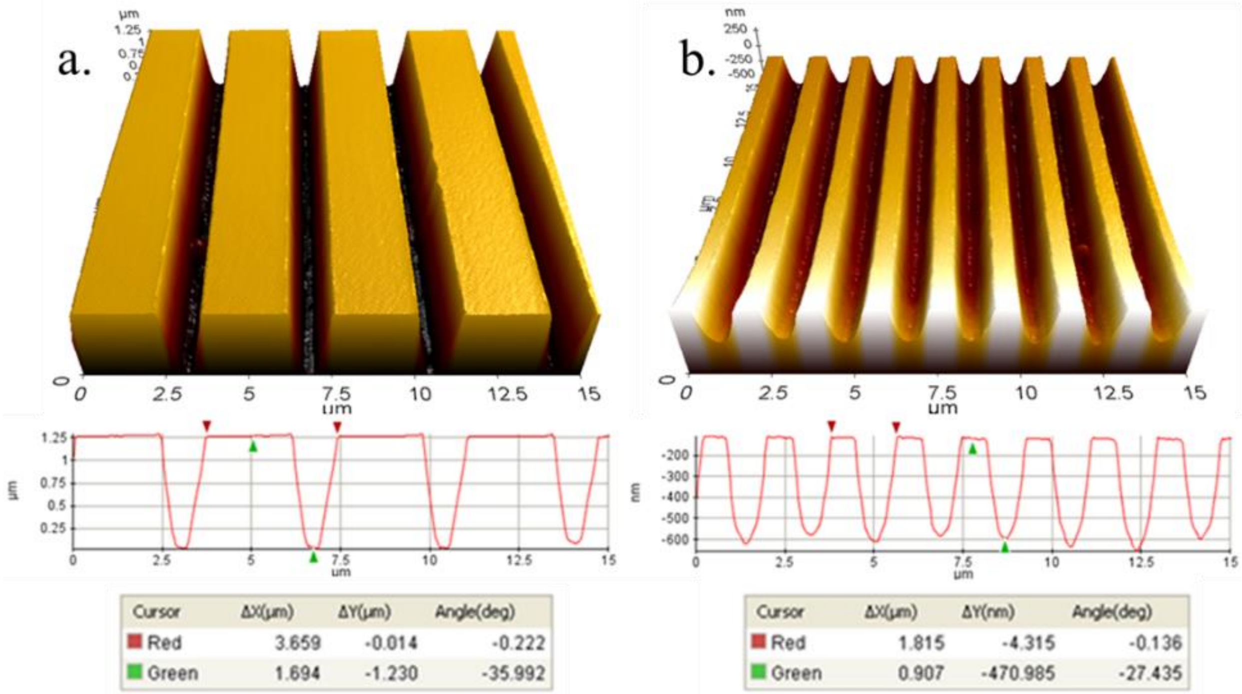

Cursor	ΔX(µm)	ΔY(µm)	Angle(deg)
🟥 Red	3.659	-0.014	-0.222
🟩 Green	1.694	-1.230	-35.992

Cursor	ΔX(µm)	ΔY(nm)	Angle(deg)
🟥 Red	1.815	-4.315	-0.136
🟩 Green	0.907	-470.985	-27.435

Figure 2.12 - Experimental demonstration of diffractive double exposure. a) Standard photoresist grating exposed with direct contact and no air gap present. b) Spatial frequency-doubled grating formed by utilizing the PR edge-bead to form an air gap between mask and PR surface.

same mask and exposure energy, but where the edge bead is retained and used to form an air gap during the exposure. As the gap cannot be directly measured during the exposures, its height is tuned by varying the contact pressure until the double grating profile is achieved upon development. The AFM scan shows that the grating period has been halved to 1.8 µm as a result of the diffracted exposure energy. The grating height in b) is also reduced from that in a), which demonstrates that the exposure energy has been split to form the secondary lines.

What this achieves practically is the ability to potentially create periodic structures smaller than would traditionally be possible with a contact mask aligner and which would require more specialized methods such as projection photolithography, holographic interference, or e-beam writing. It is not investigated further as we have access to many of these systems in our lab, but may be of use to labs without access to these resources.

2.4.3 Imprint lithography

Another method investigated for pattern transfer was an extension of imprint nanolithography. Imprint nanolithography is frequently used to rapidly and effectively reproduce nano-scale structures in thermoplastics or UV curable polymers [39]. After the creation of a master stamp, it allows for the reproduction of the desired pattern without additional photolithographic or etching steps. This is advantageous in that it allows for the creation of large surface area patterns by reducing the associated time consuming patterning to a single master device. Once the master template is created, it can be used to create numerous additional patterns.

This technique investigated in this work begins with the creation of an aluminum coated master grating which is used to cast a polydimethylsiloxane (PDMS) stamp. The stamp is then used to imprint the grating pattern into a freshly spun layer of photoresist which is then baked to remove the solvent and harden the resist. The stamp is then peeled away, leaving behind the desired pattern in the photoresist which can then be used as a standard etch mask to transfer the pattern to the substrate.

Figure 2.13 depicts the flow of the design process. The creation of the master template is shown in Fig. 2.13 a) and starts with the standard exposure and development of a photoresist grating. In order to harden the template and allow for multiple uses, the PR grating is coated with a 40 nm layer of sputtered aluminum to ensure a conformal deposition. The template device is then placed in a small tray along with a few drops of a liquid adhesion inhibiter which is then placed in a vacuum chamber and held at a rough vacuum for approximately 30 minutes. As the vacuum is drawn down, the inhibiter vaporizes and deposits a monolayer of material on top of the grating. Freshly mixed PDMS is then poured over the grating, and the tray is placed

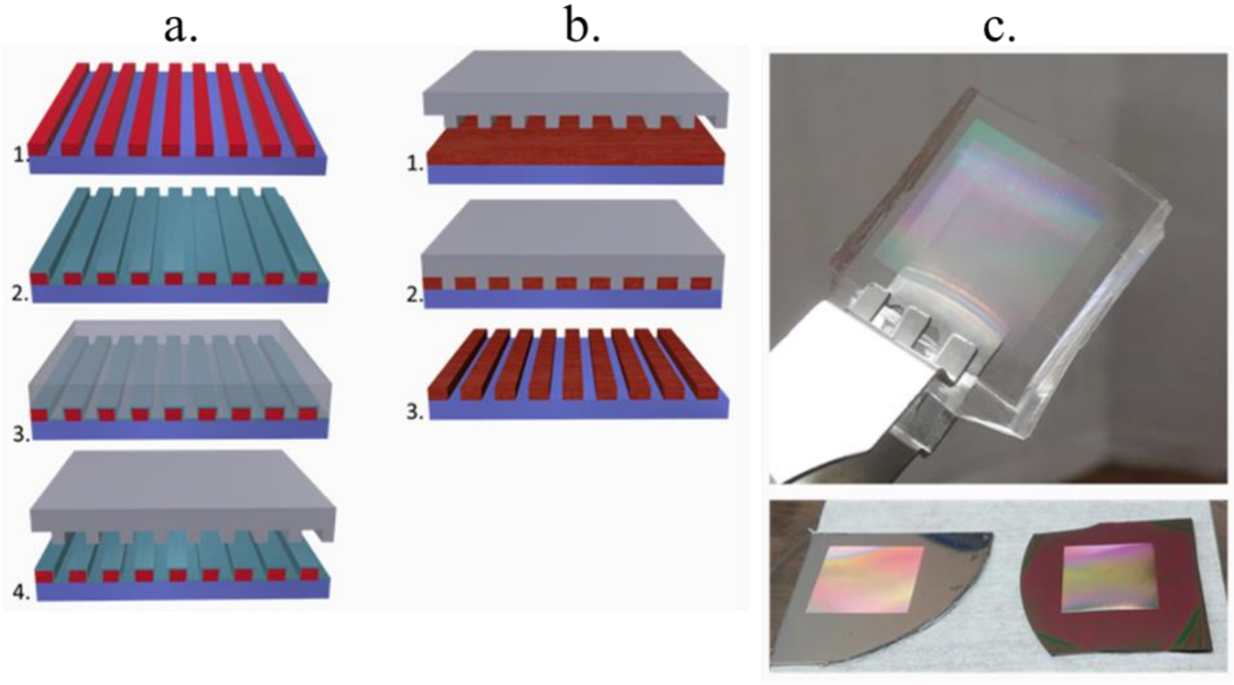

Figure 2.13 - Nanostamp fabrication and photoresist imprinting process. a) PDMS stamp creation. b) Photoresist imprinting. c) fabricated PDMS stamp, aluminum coated master template, and stamped photoresist.

back in the vacuum chamber for 2 hours to allow for the removal all dissolved gasses from the PDMS. At this point the PDMS should be transparent and free of any visible bubbles. The sample tray is then removed from the chamber and placed on a hotplate at 80^0 C for 8 hours to cure. After curing, the stamp is peeled away from the aluminum grating and is ready for use. The durability of the aluminum coating and the use of the adhesion inhibiter allows for the creation of several stamps which themselves can be used to create numerous devices before needing replacement.

Figure 2.13 b) depicts the photoresist imprinting procedure, and Fig. 2.13 c) shows images of a completed PDMS stamp along with an aluminum master grating and a stamped PR device. The stamping procedure is performed on a freshly spun layer of photoresist with the edge bead removed to ensure an even surface. The stamp is placed on top of the photoresist layer and gentle pressure is applied to remove any large air bubbles. The stamp is held in place using a metal chuck which is then place on a hot plate and allowed to bake at 125^0 C for 1 hour. This process ensures all of the solvent is driven out from the photoresist, allows it to flow into the stamp channels, and upon cooling hardens the resist to allow for smooth removal of the stamp. Upon removal of the PDMS stamp, the pattern is transferred to the photoresist layer which can then be used as a standard etch mask.

Figure 2.14 shows SEM images of a master grating before and after coating with the aluminum layer and of the final printed photoresist grating. Immediately visible is the hemispherical shape taken on by the grating as seen in Fig. 2.14 b) and c) resulting from the thermal reflow of the photoresist prior to the Al deposition. The photoresist must be cured prior to sputtering or the pattern will be degraded by the high energy impacts from the Al atoms. The curing process involves heating the PR grating to 130^0 C for 40 seconds while flooding it with

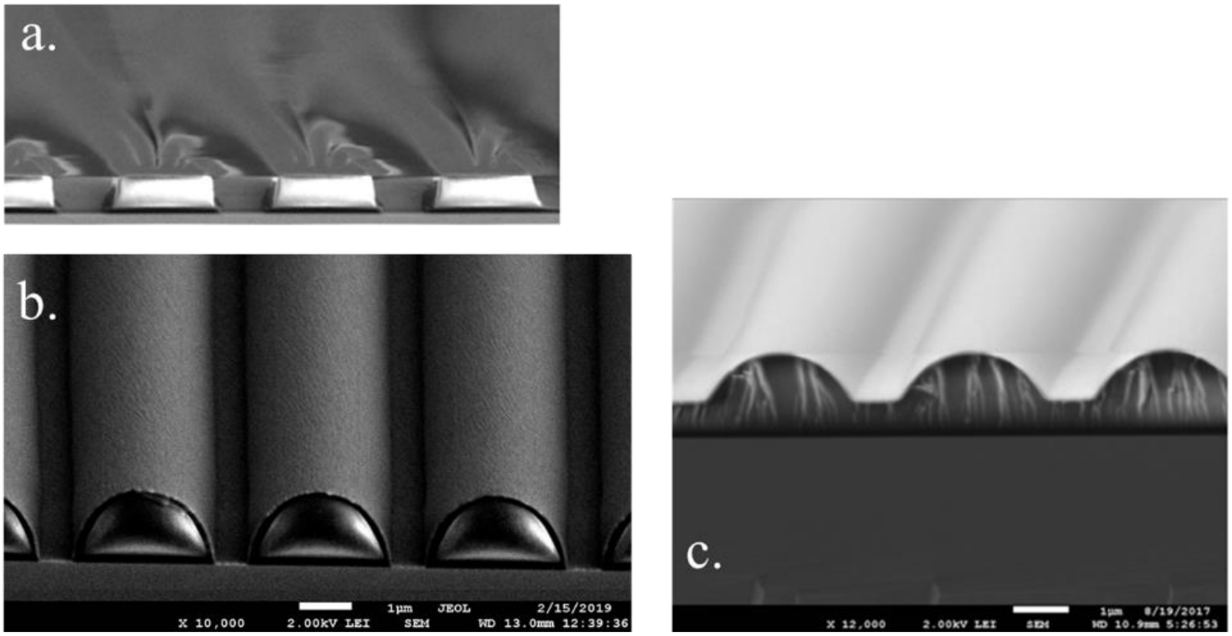

Figure 2.14 - Master grating cross-section and stamped photoresist grating with grating period $\Lambda = 3.67\ \mu m$. a) Cross-section of master PR grating. b) PR master grating after curing and Al layer coating. c) imprinted photoresist grating created from PDMS stamp showing the residual homogeneous layer and hemispherical profile.

UV light. This results in a hardened, cross-linked PR pattern, but also causes the resist to reflow into the curved profile. This profile is transferred to the stamp and ultimately to the imprinted gratings. The curved profile could be avoided by using an etched sample with a sharp wall profile as the master template, however, curved grating profiles are also not uncommon in their usage, and a straightforward method for their fabrication may be useful in future research.

A second issue of concern is the thick homogeneous layer of photoresist remaining underneath the grating visible in Fig. 2.14 c). This layer results from the spin coated photoresist being thicker than the stamp grating height and causing the stamp to “float” on the photoresist layer without contacting the substrate underneath. This can be mitigated partially with a brief exposure of the stamped grating to an O_2 plasma to open up the channels, but if the homogenous layer is too thick, the time required to clear it will result in serious degradation of the grating profile as well. Alternatively, the PR spin coat speed can be adjusted until measurements show the homogenous layer is as thin as possible. Then a brief O_2 plasma de-scum would be sufficient to prepare the sample for etching.

While the imprint method was ultimately not used in the final fabrication of devices in this work, it demonstrates the ability to become another useful tool in their fabrication. Curved grating profiles can easily be created using a simple photoresist master grating, or if more rectangular patterns are desired a pre-etched grating can be employed. One of the key benefits of the method is it allows for the elimination of the photolithographic step in device fabrication once the initial stamp is created. While photolithography is a generally reliable tool in nanofabrication, it is also greatly affected by slight misalignments and temperature and humidity changes. Substituting the photolithographic step with a stamp imprint allows for the complete elimination of yellow-room work and more rapid processing of devices.

2.5 Etching

There are three primary considerations when discussing the etching process: the degree of anisotropy achieved in the overall etch profile, the etch rate, and the selectivity of the etched material to the mask. The degree in which these variables can be controlled depends largely on the chosen etch process.

Wet chemical etching of an amorphous substrate will almost always give an isotropic etch profile, although some specialized techniques exist that utilize a metallic catalyst to create deep vertical etches. Some crystalline materials can also be anisotropicly wet etched, with a notable example being the preferential etching of the <100> plane of Si using KOH resulting in a 54.7^0 wall angle trenches.

In general, anisotropic etching requires some form of plasma etching. The mechanism employed can be purely physical, such as using an Ar plasma to physically bombard the material analogous to the target in a sputtering process. This can create near vertical etch profiles, but generally has a low etch rate and selectivity. Additional compounds can be added to the chamber to chemically react with the etched material in a reactive ion etching (RIE) process and enhance the etch rate and selectivity, but this can in turn cause a loss of anisotropy.

For this work, an etch study utilizing the Oxford Plasmalab 80 Plus in the NDG clean room is performed to develop a germanium etch recipe that optimizes the etch rate, selectivity, and anisotropy of the device profile. The etch recipe developed is a cycled process inspired by the Bosch Process used for deep RIE of silicon. The process consists of two alternating steps which are cycled through until the desire etch depth is achieved. The first step introduces a reactive chemical etchant into the chamber to begin the etch process. This is followed by sidewall passivation where a polymer building chemical is introduced that coats the exposed surfaces with a protective chemical etch resistant layer. When the chemical etchant is reintroduced, the vertical physical bombardment of the horizontal surfaces removes the passivation material and allows etch to continue while preserving the vertical sidewalls.

For deep Si etching, SF_6 is the primary etchant used and C_4F_8 is the primary polymer material. The C_4F_8 is broken down into CF_2 molecules by the ion plasma, and these are what form the protective passivation layer. For our system, CHF_3 is available and breaks down into $HF + CF_2$ in the chamber. While this produces an unwanted HF byproduct, it still performs the primary function of sidewall passivation. A schematic of the etch process along with descriptions of the etch profiles under discussion is shown in Fig. 2.15

The desired etch profile for this work is either vertical or slightly positive. A positive profile recipe allows for compensation for inexact mask tolerances by leaving extra substrate

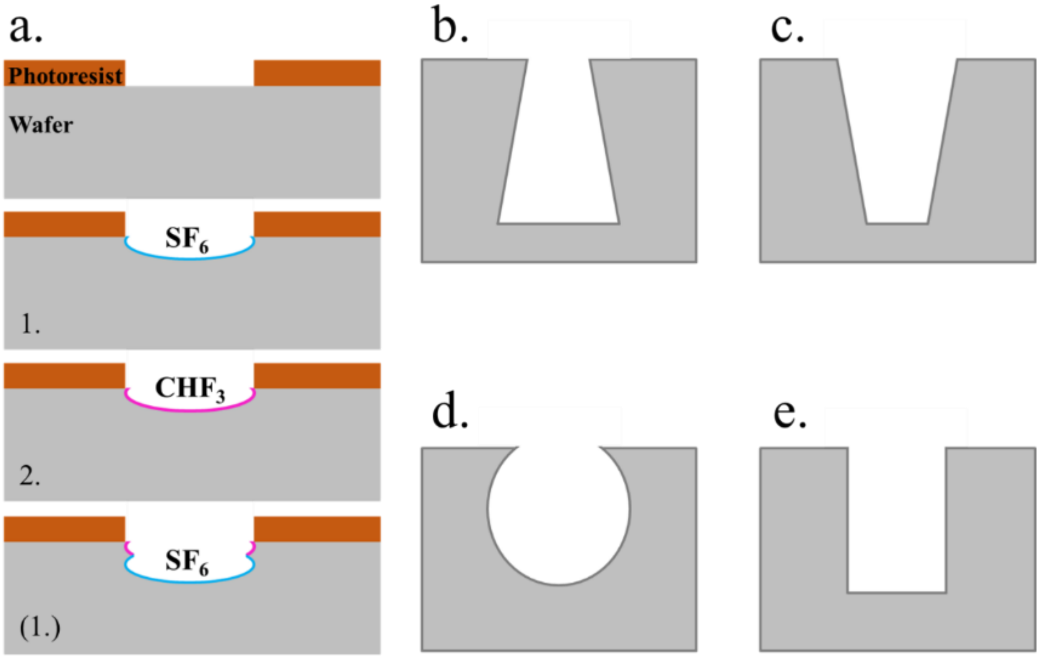

Figure 2.15 - Etch process and sidewall profiles. a) general process of the cycled etch recipe consisting of alternating etch and sidewall passivation steps. b) negative etch profile. c) positive etch profile. d) isotropic etch profile. e) vertical etch profile.

material in the etched trenches and can be reduced by increasing the amount of etchant gas. Negative or isotropic profiles generally represent over-etching of the material and in addition to being undesirable are often more difficult to counteract.

The process variables for each cycle step are power, gas flow rate, pressure, and time. Etch tests are performed using a photoresist pattern created using a photomask with period Λ = 3.67 µm and fill factor f = 0.67. Etch rate is calculated per cycle and determined by SEM images of the test samples. Etch selectivity is found by determining the amount of photoresist etched by comparing SEM cross sections of etched samples with initial photoresist grating measurements, and then comparing that amount to the amount of substrate etched. The profile is found through the cross sectional SEM measurements.

The spin coated resist thickness is 1225 nm measured with an SEM cross section as shown in Fig. 2.16. In this image we see that the PR grating also has a positive profile which will affect the etched samples profile and maximum fill factor. Anisotropy of the test samples is

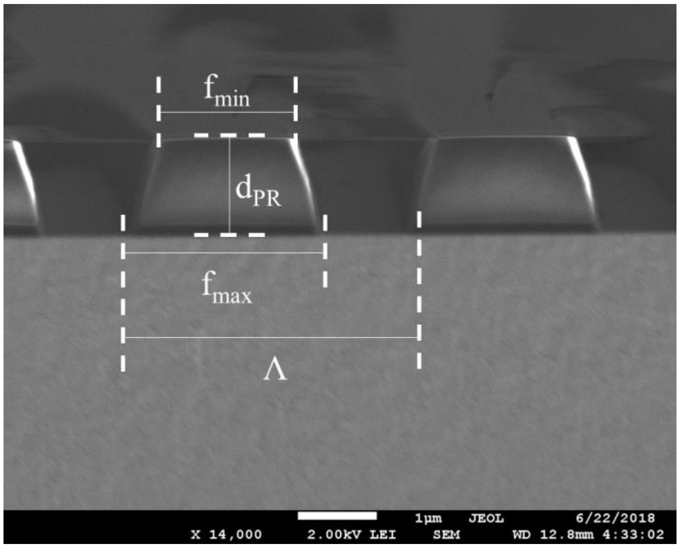

Figure 2.16 - Photoresist grating cross section. d_{PR} = 1225 nm, Λ = 3556 nm, f_{min} = 0.51, f_{max} = 0.65.

characterized using a fill factor ratio which is defined by dividing the etched grating fill factor by the maximum photoresist fill point, $f_{ratio} = f_{etch} / f_{max}$, where f_{max} is measured to be 0.65 as shown in Fig. 2.16. Higher values of f_{ratio} represent lower losses and indicate recipes with better anisotropy.

What follows are the test results for a systematic study on the impacts of power, gas flow rate, pressure, and step times on the etch profile. For each set of parameters, a 25 cycle etch is performed, after which the wafer is cleaved and examined under SEM. The study results are displayed in the following Tables 2.1, 2.2, and 2.3 along with corresponding SEM cross sectional images in Figures 2.17, 2.18, and 2.19. Best case results are highlighted in yellow. General findings are summarized in Figures 2.20, 2.21, and 2.22. For the results shown in the tables, “dPR” is the measured photoresist thickness after etching in nanometers,”dg” is the etched grating depth, “P” is the measured period of the grating, “f” is the grating width in nanometers, “ff” is the fill factor ratio equal to f/P, “f_ratio” is the fill factor ratio divided by 0.65, the starting PR fill factor, “etch rate” is nanometers etched per cycle, “selectivity” is the ratio of the amount of germanium etched divided by the amount of photoresist etched, “2.2 μm cycles” is the number of etch cycles needed to reach a target etch depth of 2.2 μm, and “max etch” is the maximum grating depth achievable with the given starting photoresist thickness and measured selectivity.

The results show that in general, increasing the SF_6 power has the effect of increasing the etch rate and anisotropy while decreasing the etch selectivity, increasing the SF_6 flow rate increases the etch rate and selectivity but reduces anisotropy, and CHF_3 has an optimal power rate to control etch rate and selectivity outside of which both will decrease.

Table 2.1 - Etch results 1.1 through 1.10.

		Pressure (mT)	Power (W)	flow (sccm)	time (s)	dPR	dg	P	f	ff	f_ratio	etch rate	selectivity	2.2 µm cycles	max etch
1.1	**SF6**	5	100	14	17	926	709	3504	2098	0.60	0.92	28.36	2.37	77.57	2906.7
	CHF3	10	100	34.2	12										
1.2	**SF6**	5	150	14	17	837	808	3599	2106	0.59	0.90	32.32	2.08	68.07	2551.03
	CHF3	10	100	34.2	12										
1.3	**SF6**	5	200	14	17	750	838	3485	2051	0.59	0.90	33.52	1.76	65.63	2161.16
	CHF3	10	100	34.2	12										
1.4	**SF6**	5	100	14	17	914	709	3580	2332	0.65	1.00	28.36	2.28	77.57	2792.68
	CHF3	15	100	34.2	12										
1.5	**SF6**	5	100	21	17	888	800	3464	2215	0.64	0.98	32	2.37	68.75	2908.01
	CHF3	10	100	34.2	12										
1.6	**SF6**	5	100	28	17	932	888	3562	2311	0.65	0.99	35.52	3.03	61.94	3712.63
	CHF3	10	100	34.2	12										
1.7	**SF6**	5	100	28	17	917	864	3617	2133	0.59	0.90	34.56	2.81	63.66	3436.36
	CHF3	15	100	34.2	15										
1.8	**SF6**	5	150	28	17	765	1100	3528	2166	0.61	0.94	44	2.39	50.00	2929.35
	CHF3	15	100	34.2	12										
1.9	**SF6**	5	200	28	17	706	1175	3519	1969	0.56	0.86	47	2.26	46.81	2773.36
	CHF3	15	100	34.2	12										
1.10	**SF6**	5	150	28	17	756	1075	3656	2194	0.60	0.92	43	2.29	51.16	2807.84
	CHF3	20	100	34.2	12										

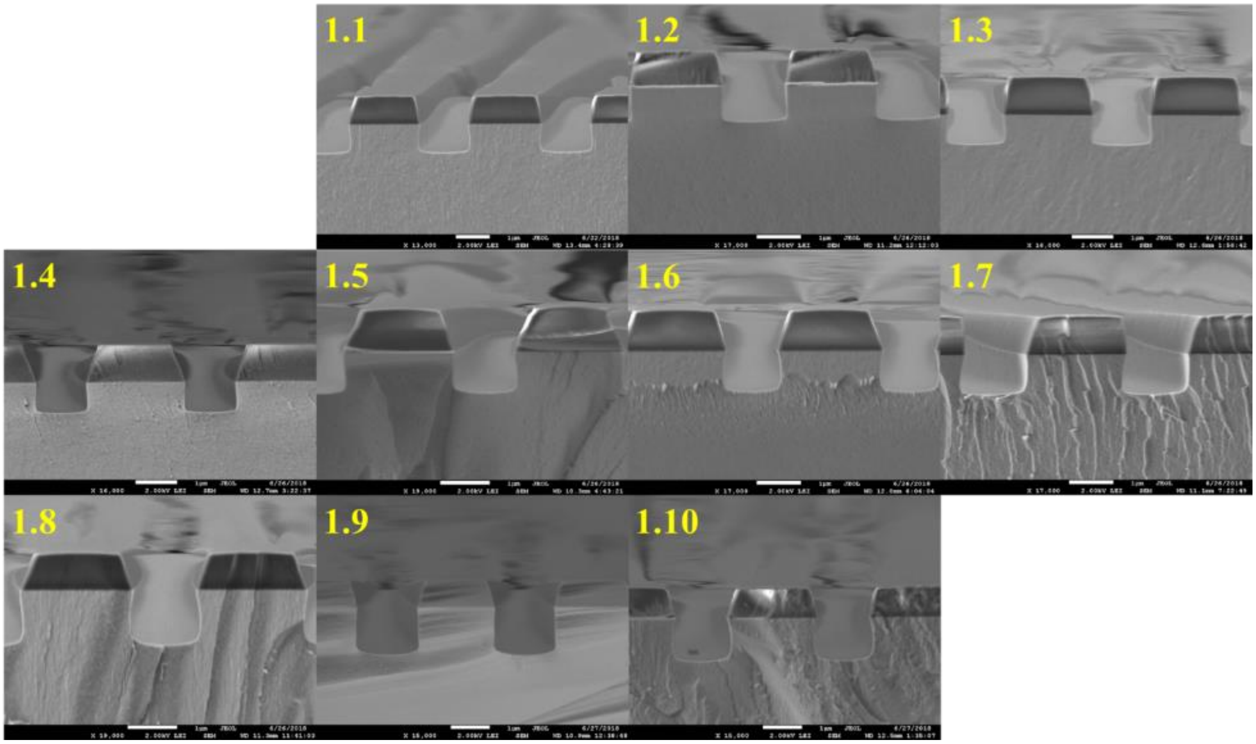

Figure 2.17 - SEM images for etch tests 1.1 through 1.10.

Table 2.2 - Etch results III.1 through III.6.

		Pressure (mT)	Power (W)	flow (sccm)	time (s)	dPR	dg	P	f	ff	f_ratio	etch rate	selectivity	2.2 µm cycles	max etch
III.1	**SF6**	5	200	28	12	785	844	3551	1992	0.56	0.81	33.76	2.16	65.17	2542.82
	CHF3	15	150	34.2	17										
III.2	**SF6**	5	200	35	12	844	969	3547	1961	0.55	0.80	38.76	2.93	56.76	3439.80
	CHF3	15	150	34.2	17										
III.3	**SF6**	5	250	35	12	701	898	3533	1945	0.55	0.80	35.92	1.89	61.25	2226.05
	CHF3	15	150	40	17										
III.4	**SF6**	5	100	28	12	943	633	3562	2086	0.59	0.85	25.32	2.73	86.89	3205.93
	CHF3	15	150	40	17										
III.5	**SF6**	5	150	28	12	850	803	3504	2004	0.57	0.83	32.12	2.47	68.49	2903.15
	CHF3	15	150	40	17										
III.6	**SF6**	5	200	28	12	770	830	3449	1955	0.57	0.82	33.2	2.05	66.27	2408.02
	CHF3	15	150	40	17										

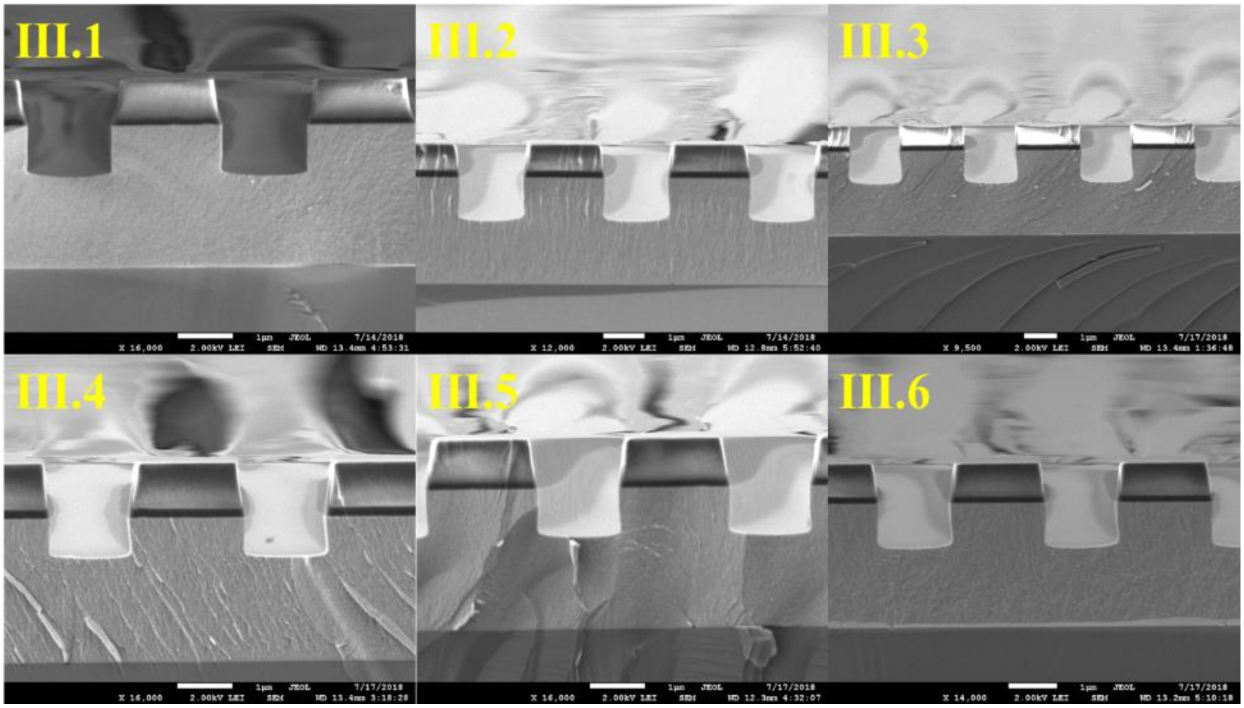

Figure 2.18 - SEM images for etch tests III.1 through III.6.

Table 2.3 - Etch results IV.6 through IV.17.

		Pressure (mT)	Power (W)	flow (sccm)	time (s)	dPR	dg	P	f	ff	f_ratio	etch rate	selectivity	2.2 µm cycles	max etch
IV.6	**SF6**	5	100	28	17	945	635	3541	2063	0.58	0.92	25.4	2.76	86.61	3244.02
	CHF3			17											
	CHF3	15	100	34.2	12										
IV.7	**SF6**	5	150	28	17	945	779	3606	2070	0.57	0.91	31.16	3.39	70.60	3979.67
	CHF3			17											
	CHF3	15	100	34.2	12										
IV.8	**SF6**	5	200	28	17	803	785	3557	2004	0.56	0.89	31.4	2.11	70.06	2479.50
	CHF3			17											
	CHF3	15	100	34.2	12										
IV.9	**SF6**	5	175	24	17	756	744	3419	1944	0.57	0.90	29.76	1.78	73.92	2086.40
	CHF3			14											
	CHF3	15	100	17	12										
IV.10	**SF6**	5	150	35	12	875	856	3519	1988	0.56	0.89	34.24	2.85	64.25	3352.67
	CHF3			0											
	CHF3	15	150	35	12										
IV.11	**SF6**	5	150	35	12	944	606	3569	2175	0.61	0.96	24.24	2.62	90.76	3082.47
	CHF3			14											
	CHF3	15	150	35	12										
IV.12	**SF6**	10	150	35	12	984	633	3504	2016	0.58	0.91	25.32	3.31	86.89	3894.11
	CHF3			14											
	CHF3	15	150	35	12										
IV.13	**SF6**	10	100	35	12	1036	641	3682	2203	0.60	0.94	25.64	4.61	85.80	5418.53
	CHF3			7											
	CHF3	15	150	35	12										
IV.14	**SF6**	10	100	35	12	475	2196	3509	1741	0.50	0.78	25.53488	3.14	86.16	3686.14
	CHF3			7											
	CHF3	15	150	35	15										
IV.15	**SF6**	10	100	35	12	888	834	3424	1964	0.57	0.90	33.36	2.91	65.95	3414.46
	CHF3			7											
	CHF3	15	150	35	12										
IV.16	**SF6**	10	200	50	12	861	820	3492	1969	0.56	0.89	32.8	2.61	67.07	3068.47
	CHF3			7											
	CHF3	15	150	50	15										
IV.17	**SF6**	8	250	50	12	743	1045	3556	1935	0.54	0.86	41.8	2.42	52.63	2842.30
	CHF3			7											
	CHF3	15	150	50	15										

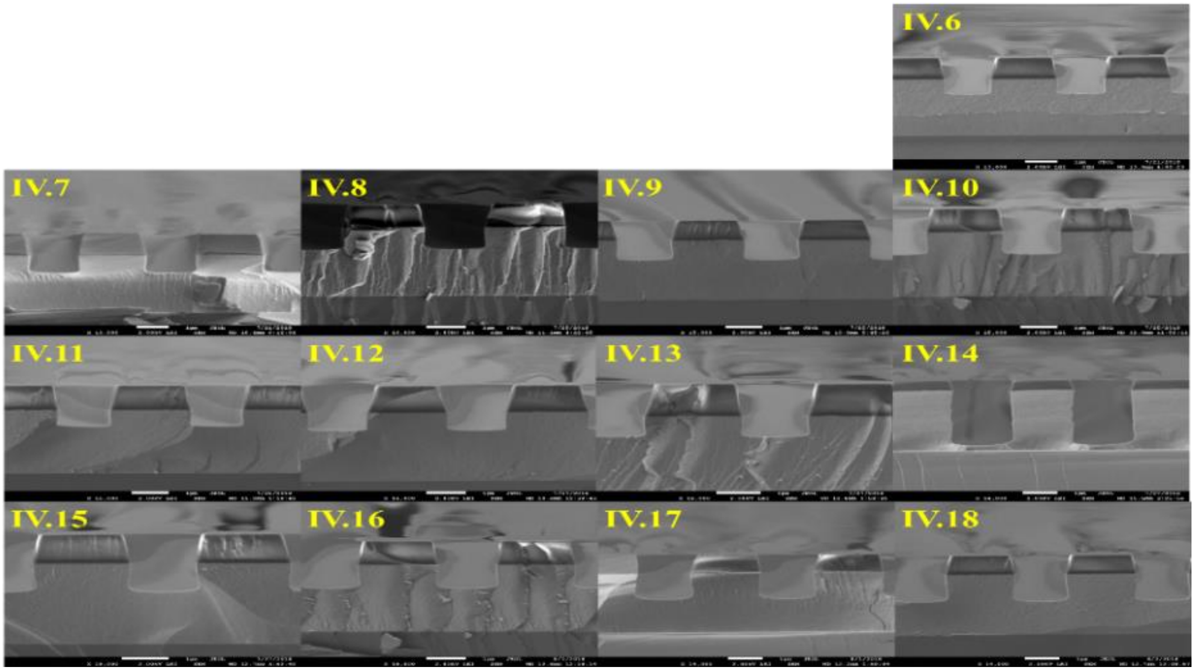

Figure 2.19 - SEM images for etch tests IV.6 through IV.18.

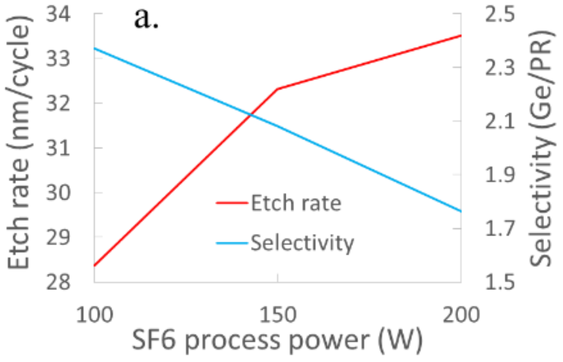

b.

base	pressure (mT)	power (W)	flow rate (sccm)	time (s)
SF6	40/5	**100**	14	17
CHF3	40/10	100	34.2	12

c.

SF6 power	selectivity	etch rate	fill factor	f_ratio
100.00	2.37	28.36	0.60	0.92
150.00	2.08	32.32	0.59	0.90
200.00	1.76	33.52	0.59	0.90

Figure 2.22 – SF6 power results. a) graphical display of results. b) baseline etch parameters. c) experimental results.

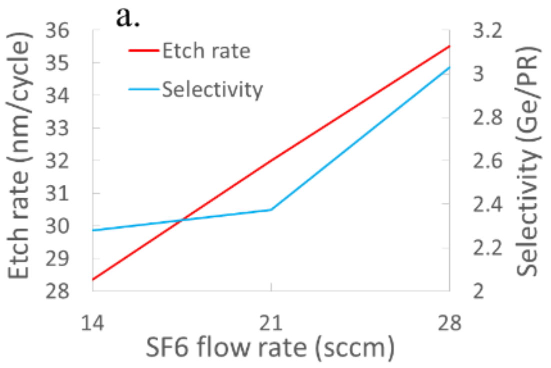

b.

base	pressure (mT)	power (W)	flow rate (sccm)	time (s)
SF6	40/5	100	**14**	17
CHF3	40/15	100	34.2	12

c.

SF6 sccm	selectivity	etch rate	fill factor	f_ratio
14.00	2.28	28.36	0.65	1.00
21.00	2.37	32.00	0.64	0.98
28.00	3.03	35.52	0.65	0.99

Figure 2.21 – SF_6 flow rate results. a) graphical display of results. b) baseline etch parameters. c) experimental results.

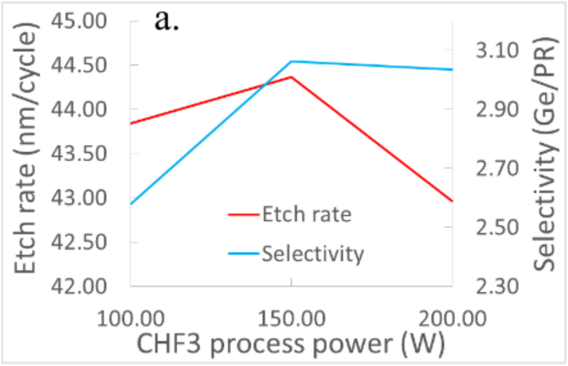

b.

base	pressure (mT)	power (W)	flow rate (sccm)	time (s)
SF6	40/5	150	28	12
CHF3	40/15	**100**	34.2	12

c.

CHF3 power	selectivity	etch rate	fill factor	f_ratio
100.00	2.58	43.84	0.56	0.89
150.00	3.06	44.36	0.54	0.86
200.00	3.03	42.96	0.60	0.95

Figure 2.20 - CHF_3 power results. a) graphical display of results. b) baseline etch parameters. c) experimental results.

Another finding in these experiments is the significant impact the size of the sample stage has on the etch process. The RIE chamber is fitted with carbon disk stage plates with 2” and 4” diameter center openings under which is placed a 4” silicon carrier wafer as shown in Figure 2.23 a). All results presented in the previous figures and tables were achieved using the 4“ stage opening.

Measurements show that samples etched using the 2” stage show significant increases in the etch rate and selectivity, as if the effective flow rate of the etchant gas had been increased. Figure 2.23 b) shows the identical etch recipes used with the 2” and 4” stages along with the etch results, and Fig. 2.23 c) shows the resulting etch profiles where the 2” stage sample demonstrates significantly increased etching.

This can be explained by the exposed surface area of the silicon carrier wafer. During the etch process, the silicon wafer surface is competing with the test samples for the utilization of the gas chemistries. With the entire 4” wafer exposed, more of the etch gasses are interacting with the silicon, leaving less for the sample. When the 2” opening is used, fewer reactants are lost and the sample sees a higher concentration of fresh gasses, resulting in the enhanced etch rate. By switching from the 4” to the 2” stage, the etch rate is increased roughly 33% and the accompanying selectivity increases by roughly 10%.

A maximum flow rate of 35 sccm was used for the process gases, and with this rate It was found that the 4” wafer was ultimately a limiting factor in the maximum etch rate, selectivity, and profile results. A second set of tests was run using the 2” diameter opening using a similar parametric sweep of the process variables as shown in Figures 2.17-2.19. The results of the study are summarized in Fig. 2.24 where in this case only the best three recipe results are shown.

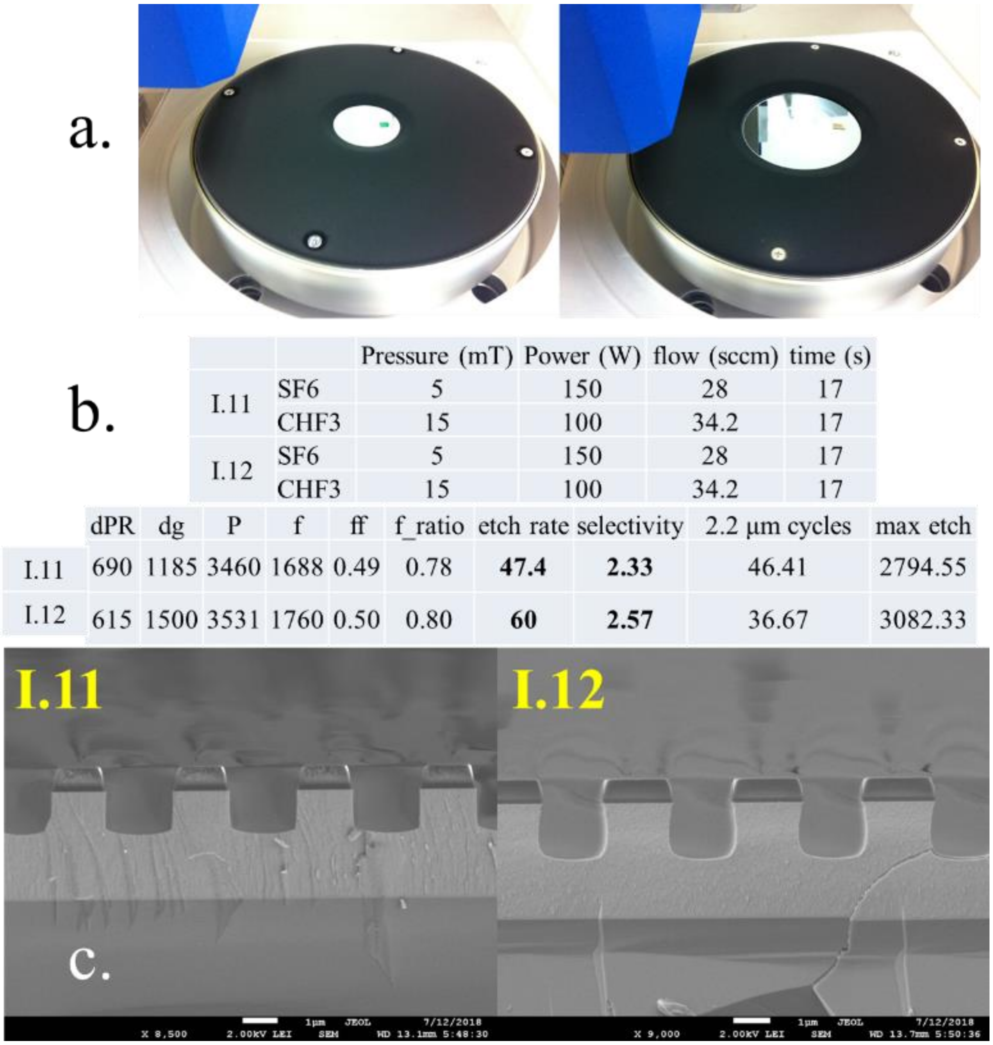

		Pressure (mT)	Power (W)	flow (sccm)	time (s)
I.11	SF6	5	150	28	17
	CHF3	15	100	34.2	17
I.12	SF6	5	150	28	17
	CHF3	15	100	34.2	17

	dPR	dg	P	f	ff	f_ratio	etch rate	selectivity	2.2 µm cycles	max etch
I.11	690	1185	3460	1688	0.49	0.78	**47.4**	**2.33**	46.41	2794.55
I.12	615	1500	3531	1760	0.50	0.80	**60**	**2.57**	36.67	3082.33

Figure 2.23 - Etch chamber stage comparisons. a) photographs of the 2” and 4” stage installed in the etch chamber. b) Etch parameters and etch results for the 4” stage corresponding to I.11 and the 2” stage corresponding to I.12. c) SEM images showing the etch profile for the 4” stage (I.11) and 2” stage (I.12).

Recipe V.4 resulted in the best overall etch profile from all of the samples, and it is interesting in that it incorporates a hybrid etch procedure. The etch step utilizes 14 sccm of CHF_3 along with the SF_6 etchant. This would be a typical combination used in a single step etch recipe, and in this case the additional polymer gas likely helps to regulate sidewall erosion. It is followed by a dedicated polymer building step, and the combination of the two results in minimized sidewall losses while maximizing the etch depth and selectivity. Using the 2” sample a.

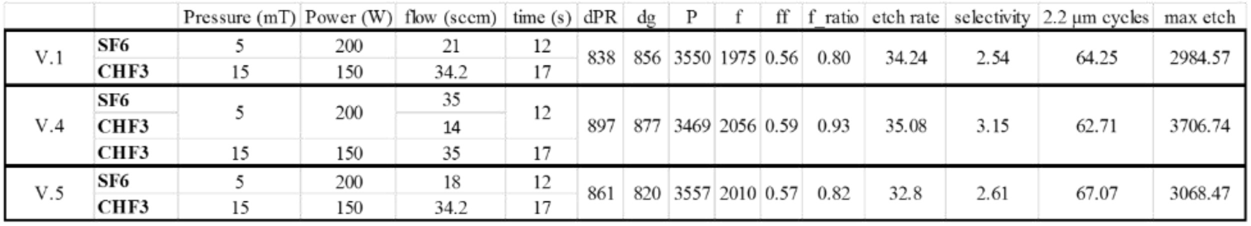

		Pressure (mT)	Power (W)	flow (sccm)	time (s)	dPR	dg	P	f	ff	f_ratio	etch rate	selectivity	2.2 μm cycles	max etch
V.1	**SF6**	5	200	21	12	838	856	3550	1975	0.56	0.80	34.24	2.54	64.25	2984.57
	CHF3	15	150	34.2	17										
V.4	**SF6**	5	200	35	12	897	877	3469	2056	0.59	0.93	35.08	3.15	62.71	3706.74
	CHF3			14											
	CHF3	15	150	35	17										
V.5	**SF6**	5	200	18	12	861	820	3557	2010	0.57	0.82	32.8	2.61	67.07	3068.47
	CHF3	15	150	34.2	17										

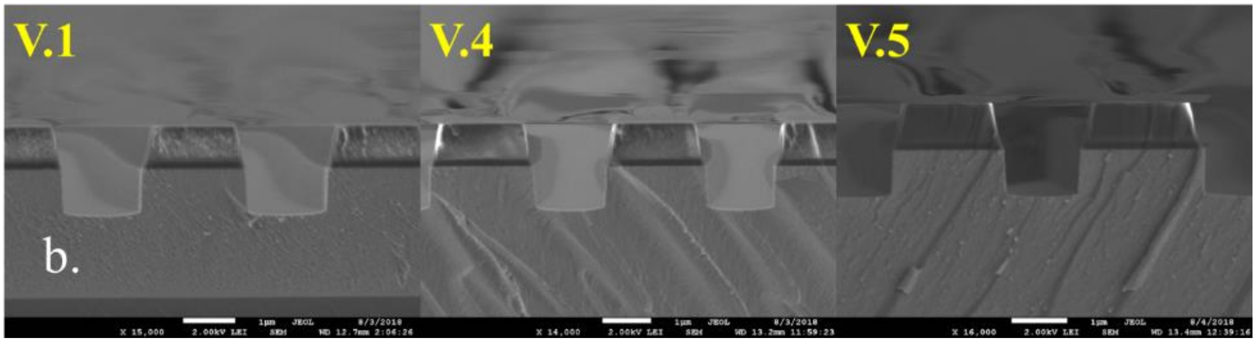

Figure 2.24 - 2” stage Ge etch results. a) table of recipes resulting in the best profile, etch rate, and selectivity. b) SEM cross sections of the test samples showing the positive etch profiles.

stage along with this hybrid cycled recipe, it became possible to achieve the desired positive etch profile along with high etch rate and selectivity.

2.5.1 Film density influence

A final note is made in consideration of the impacts of the film density on the etch rate and profile. The preceding etch studies were carried out using sputtered germanium films. It is well known that the sputtering process will generally result in a more dense film that other processes such as CVD or evaporation methods. This density will in turn impact the resulting etch profiles, with the less dense films generally having a higher etch rate. In Figure 2.25, etch test results are displayed for a 1300 nm Ge film deposited by e-beam evaporation. In Fig. 2.25 a) the film is shown along with a developed photoresist grating on top, while Fig. 2.25 b) shows a cross section of the film after a 20 cycle etch using recipe V.4 from above.

The measured initial photoresist dimensions in Fig. 2.25 a) are d_{PR} = 955 nm, Λ = 3503 nm, f_{min} = 1304 nm, and f_{max} = 1700 nm. The post etch measurements are d_{PR} = 633 nm, d_g =

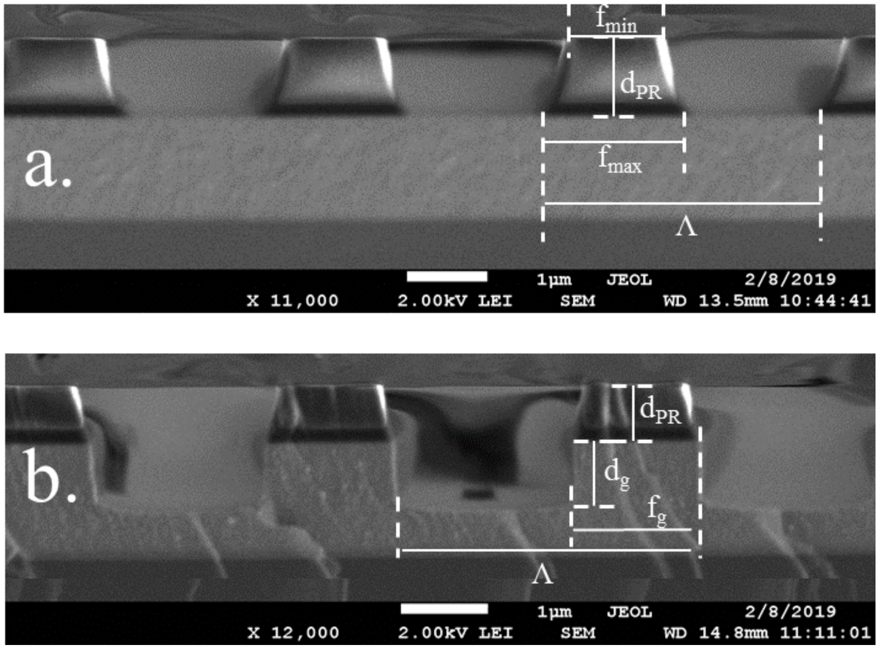

Figure 2.25 - Evaporated film etch results. a) unetched film and photoresist grating. b) PR and Ge film after 20 cycle etch using recipe V.4.

797 nm, Λ = 3531 nm, and f_g = 1508 nm. This gives an etch rate of 39.85 nm / cycle or 82.45 nm / min, etch selectivity of 2.475, and a fill ratio of 0.88. Compared to the sputtered test results displayed in Fig. 2.24, the etch rate has increased, though the selectivity and fill ratio have decreased slightly. The profile is also slightly positive though nearly vertical. This demonstrates that while the recipe gives similar results for sputtered and evaporated films, test etches should always be performed when going from one to the other to ensure accurate grating depth and fill factor results.

2.6 Fabrication process conclusions

The results of this chapter have been compiled primarily as a guide for the processing and fabrication of germanium based devices. While many different materials exist with desirable optical properties in the mid to long-wave IR, germanium stands out as an optimal device layer material due to its high refractive index, lack of toxicity, and ease of processing. Many of the standard techniques developed in silicon processing carry over to germanium devices with minimal modifications, which carries the advantage of not requiring additional investment in expensive new equipment or facilities. It was also shown in the etching process how techniques developed for deep reactive ion etching of silicon substrates can effectively be translated to standard etch chambers to achieve micrometer depth etching of germanium while maintaining desired device profiles. Other novel methods of patterning using diffractive methods and PDMS stamps were also introduced that when combined with all the rest, provide an array of useful tools in the fabricator's toolbox for use in the creation of devices in the mid and long-wave IR.

Chapter 3 Wideband longwave-infrared Ge-ZnS GMR reflectors

3.1 Introduction

Photonic devices operating in the mid-IR (3 – 5 μm) and long-IR (8 – 13 μm) are fast becoming topics of active research. As mentioned in chapter 1, the mid and long-wave IR spectral regions are zones of relative atmospheric optical transparency. This makes them important for applications including terrestrial imaging [40] [41], spectroscopic applications [42] [43], and various medical and industrial laser technologies [44] [45] [46] [47]. Periodic photonic metasurfaces are commonly engineered to operate in the visible and near-IR regions [48]. These devices can be designed to act as wideband reflectors [49], anti-reflections surfaces [50], planar lenses [48] [51], polarizers [52] [53], and band-pass or band-stop filters [54] [55] [56] [57]. Due to the linear nature of Maxwell's equations, the same basic designs can be used to create mid and long-IR devices as well [58] [59], though at this time, literature describing their fabrication is sparse. The challenge in fabricating devices in this range often lies in adapting established fabrication technologies to work with photonic materials outside of those typically used in the visible and near-IR region, and with working with device dimensions that fall between the nanoscale (10s to 100s of nanometers) and MEMs range (10s to 100s of micrometers). In this chapter, the design, fabrication, and measurement results are presented for germanium-zinc sulfide based wideband GMR reflectors operating in the longwave IR.

3.2 Design

The devices in this chapter are designed as wideband guided-mode resonance reflectors. This wideband response is enabled by creating a design with multiple guided modes within close spectral proximity with each being efficiently pumped by multiple evanescent diffraction orders [60]. These resonances create an overlapping response that results in a flat-top, wideband reflection. The widest bandwidth responses are generally found using the TM polarization, though TE designs are possible as well.

3.2.1 Particle swarm optimization

Rough physical dimensions for the wideband reflectors in this study are first determined by running a serious of particle swarm optimization (PSO) sweeps. This is an iterative technique designed to search for optimized design parameters that will fulfill a desired output spectrum [61]. In this case, a search is run for a reflector with a 30% bandwidth centered at 10 µm. The fractional bandwidth is a dimensionless figure of merit that is determined by dividing the absolute bandwidth by the center wavelength, and is used to characterize the efficiency of a design without referencing the absolute dimensions.

Figure 3.1 shows a sample output from the PSO code with a GUI interface developed to facilitate ease of use. Search parameter windows are entered into the device parameters section to limit the areas in which the code will look for a design. In general, running several sweeps

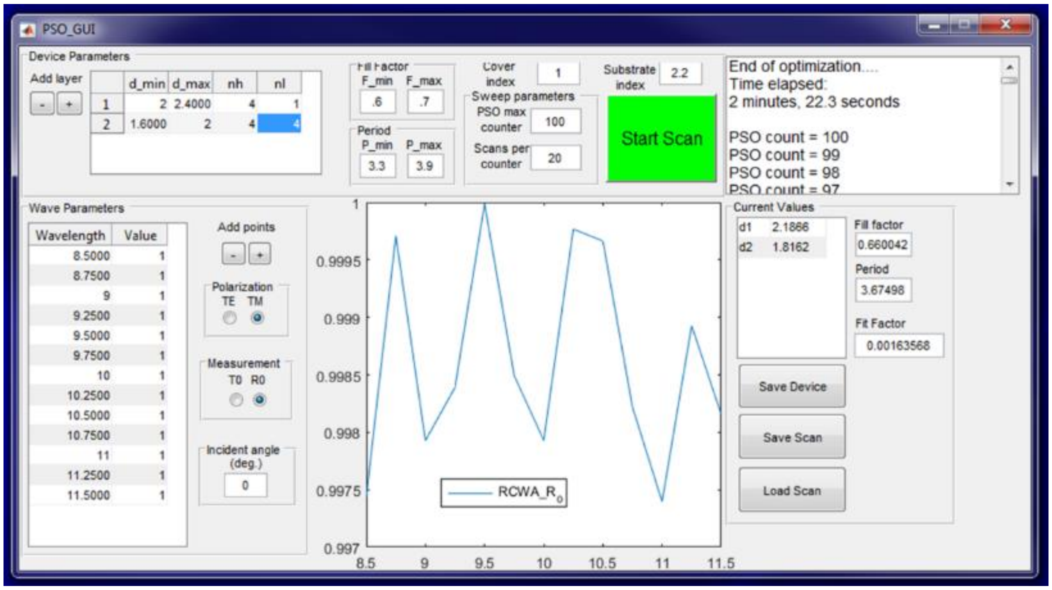

	d_min	d_max	nh	nl
1	2	2.4000	4	1
2	1.6000	2	4	4

Fill Factor
F_min .6
F_max .7

Period
P_min 3.3
P_max 3.9

Cover index 1
Substrate index 2.2

Sweep parameters
PSO max counter 100
Scans per counter 20

Wavelength	Value
8.5000	1
8.7500	1
9	1
9.2500	1
9.5000	1
9.7500	1
10	1
10.2500	1
10.5000	1
10.7500	1
11	1
11.2500	1
11.5000	1

Polarization
TE ○ TM ●

Measurement
T0 ○ R0 ●

Incident angle (deg.) 0

```
End of optimization....
Time elapsed:
2 minutes, 22.3 seconds

PSO count = 100
PSO count = 99
PSO count = 98
PSO count = 97
```

d1	2.1866
d2	1.8162

Fill factor 0.660042
Period 3.67498
Fit Factor 0.00163568

Figure 3.1 - PSO GUI interface.

consisting of small window sizes will provide more accurate results than running a single sweep with a very wide parameter window that will likely miss an optimal design due to the random nature of the algorithm. In this case, sweep windows have been set with foreknowledge of an optimal design as an example of the code's ability to converge on a result. Output dimensions are displayed in the bottom right "Current Values" section along with a fit factor parameter that is a measure of the closeness to the converged results to the desired input spectrum with lower values being better and anything less than 0.01 generally being a good fit.

Figure 3.2 shows a more detailed calculation using the PSO algorithm output parameters and incorporating dispersive index of refraction values for germanium and zinc sulfide. We see the result is a very good flat-top wideband reflector with a 31% bandwidth for $R_0 > 0.995$. This calculation demonstrates the effectiveness of the PSO even as it uses static values for the refractive index. The code will result in reliable spectra, but this does depend strongly on the dispersiveness of the materials studied.

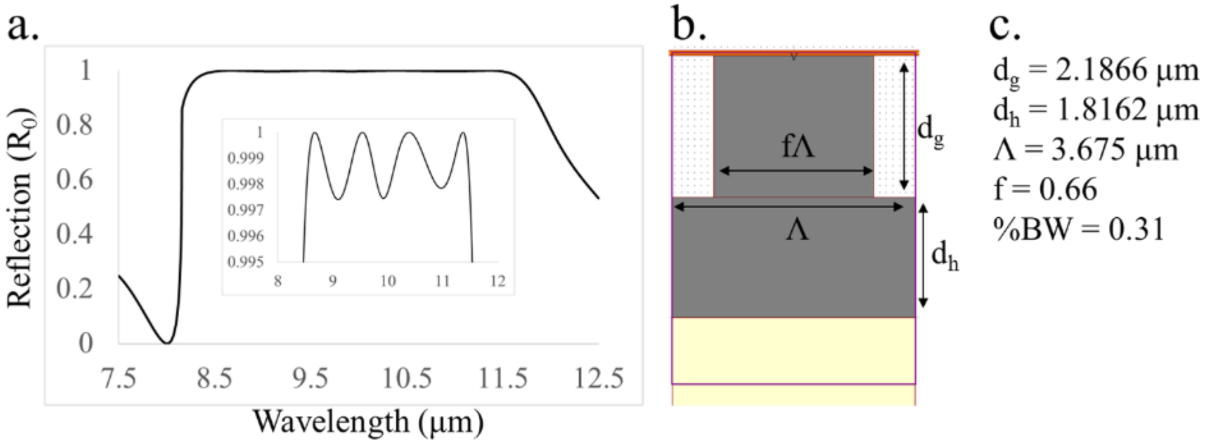

Figure 3.2 - Optimized wideband device. a) R_0 spectrum showing flat-top response, inset shows reflection for $R_0 > 0.995$. b) Device schematic. c) Physical device parameters and percent bandwidth.

3.2.2 Device tuning

Often the output of the PSO algorithm will need to be tuned to achieve an optimal result. This can be achieved by re-running the PSO code using progressively smaller windows until a desired fit factor is achieved, but a more robust method that gives more insight into the device response and fabrication tolerances is to plot a parametric sweep using the PSO parameters as a starting point. The results of these sweeps can be used to either adjust a rough output from the PSO code into an optimal resonant shape, or can be used to tailor an already optimized design for a specific application.

In Figure 3.3 we see the results of taking the optimal design shown in Figure 3.2 and performing a sweep of d_g, d_h, and f while holding the other two values constant at their optimal

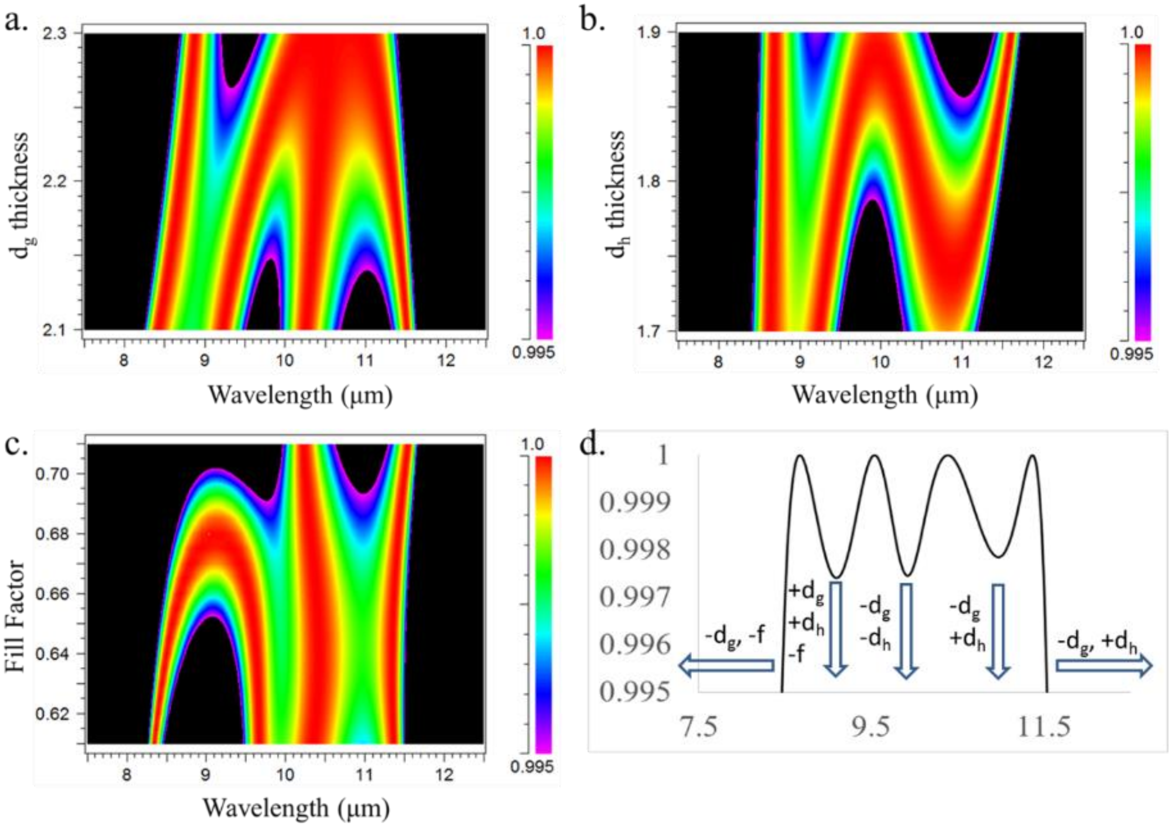

Figure 3.3 - parametric sweep of 1D device. a) d_g sweep results. b) d_h sweep results. c) fill factor sweep results. d) summary of parametric influence on resonant response.

values. The 2D plots are generated in respect to the device reflectance R_0 and provide a visual guide to how the response of the device will be affected by changing the physical dimensions. Figure 3.3 d) summarizes the effects the dimensions have on the resonant lobes where we see that for instance the bandwidth of the device can be increased by decreasing the value of d_g or the minimum value of the second and third lobes can be increased by increasing the value of d_g while sacrificing bandwidth.

This parametric data can be used to easily tune the response to a desired shape, as shown in Figure 3.4. In Fig. 3.4 a), the percent bandwidth has been reduce to 23%, but R_0 across the band is now greater than 0.9995. In Fig. 3.4 b), the bandwidth has been increased to 36%, but

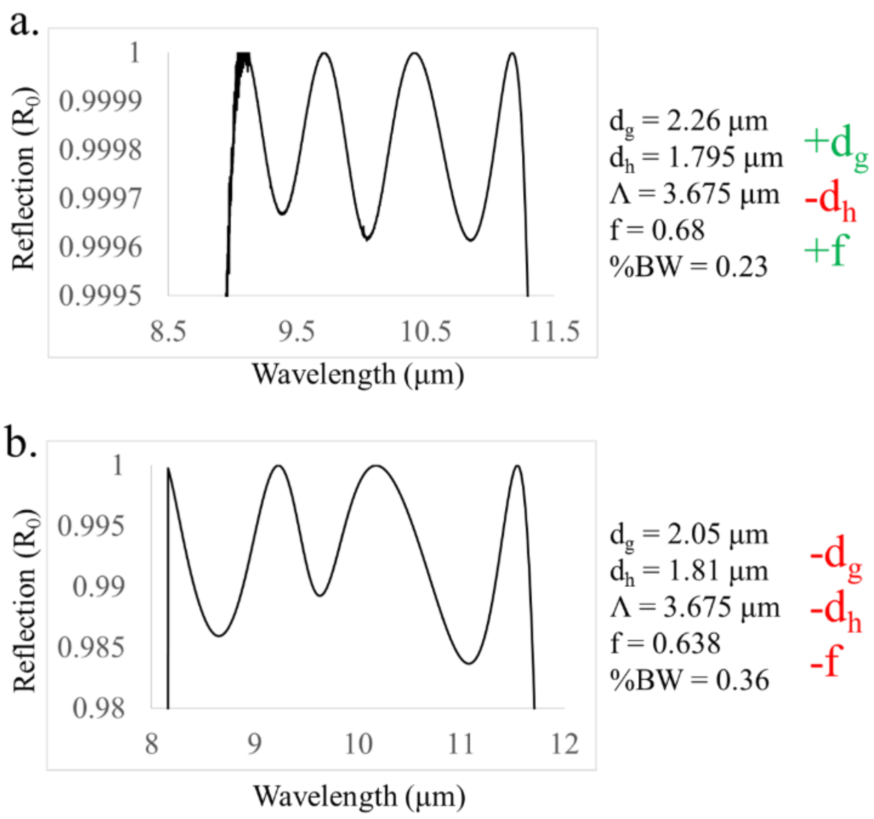

Figure 3.4 - Tuned 1D reflector designs. a) high-reflectance, lower bandwidth design. b) high-bandwidth design sacrificing some reflectance.

now R_0 is only greater than 0.98 across the band. Newly derived device values are shown next to each resonant curve. And while these results could also have been derived by re-running the PSO code, it is important to note that using the parametric sweeps also gives insight into fabrication tolerances. We see from Fig. 3.3 c), for instance, that while the second and third minima are largely unaffected by fill factor variances, the first minimum will drop sharply if the fill factor decreases significantly from the optimal value of 0.66.

3.2.3 HCG & ZCG designs

There are two general design archetypes for a GMR device. They are what have been coined as “high-contrast gratings” (HCG) [62] and “zero-contrast gratings (ZCG) [63]. The contrast in this context is between the index of refraction of the grating material and that of the homogeneous layer directly beneath it. A HCG device will consist of a stand-alone high-index grating placed directly on top of a low-index substrate. A ZCG device in contrast places an additional layer of the same high-index material beneath the grating and on top of the substrate. The benefits of this additional layer for a wideband device is that it increases the effective index of refraction of the waveguide and allows additional modes to be brought into the resonance. This additional mode can significantly increase the overall bandwidth of the device as shown in Fig. 3.5. Figure 3.5 a) is a HCG Ge on ZnS device with a percent bandwidth of 0.24 for $R_0 > .995$. The inset shows there are three $R_0 = 1$ nodes which combine to create the wideband response. In Fig.3.5 b) the ZCG design from fig 3.2 is shown again where now we note the extra $R_0 = 1$ node present in the resonance at 11.5 μm that increases the bandwidth to 0.31.

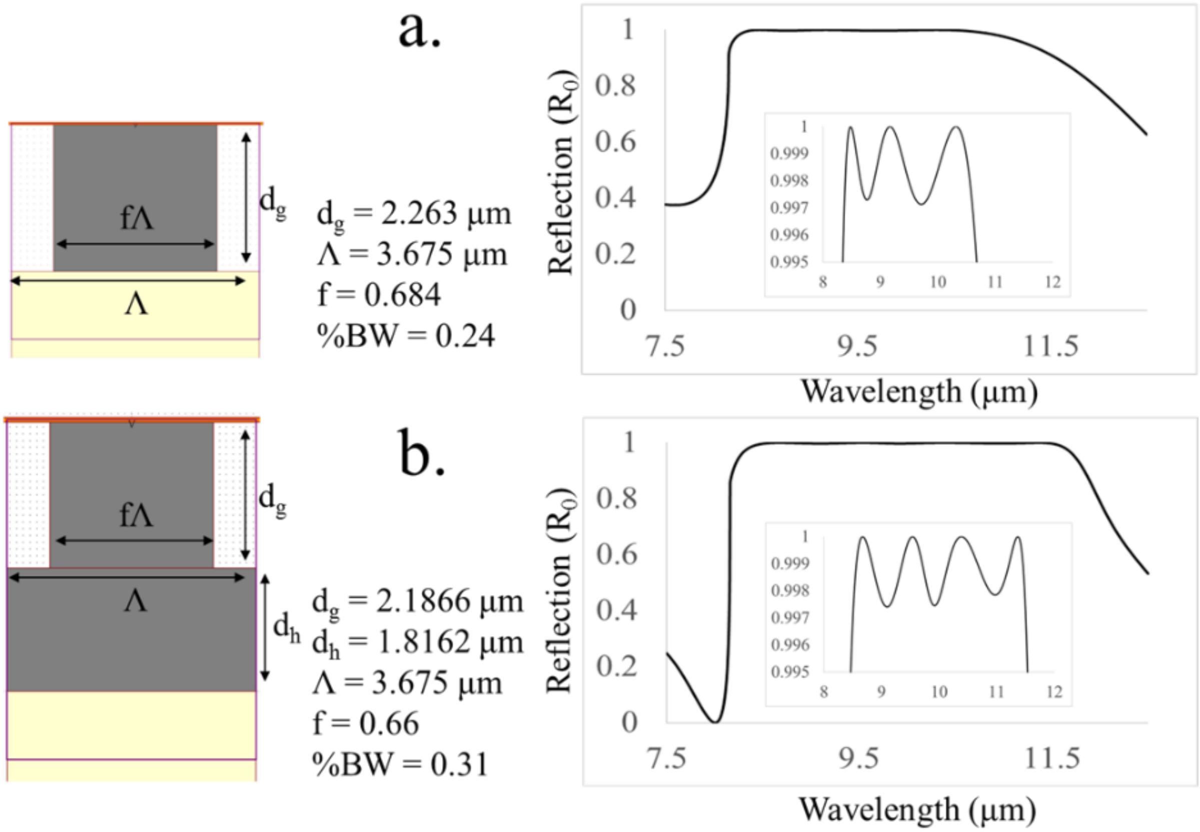

Figure 3.5 - HCG and ZCG design comparisons. a) HCG grating dimensions and spectrum. b) ZCG grating design.

3.2.4 1D and 2D designs

The one dimensional (1D) grating designs discussed up to this point will exhibit polarization dependent responses and have been designed to operate in the transverse magnetic (TM) polarization state. The transverse electric (TE) response of these devices will in general not consist of any wideband reflection, and should be accounted for when designing for a specific application. If an unpolarized response is desired, a two dimensional design can be considered.

A straight-forward implementation is shown in Figure 3.6 where the one dimensional HGC design has been split into an array of square posts with the same grating height, fill factor and periodicity. The accompanying spectrum shows a flat-top wideband reflection that is now polarization independent, however the bandwidth is less than half that of the one dimensional design due to the simultaneous TE/TM resonant characteristics and the TE resonant modes limiting the bandwidth. The inset figure shows that there are now only two resonant modes contributing to the response. This is a consequence of the additional material losses in the 2D design that reduces the effective index of refraction of the layer which allows fewer waveguide modes to be present.

As before, the bandwidth can be increased with the inclusion of an additional layer to form a ZCG design. A ZCG 2D design is shown in Fig. 3.7 along with its accompanying spectrum. Here we see again a greatly enhanced bandwidth with the additional waveguide modes doubling the bandwidth of the device. This case in particular highlights the influence of

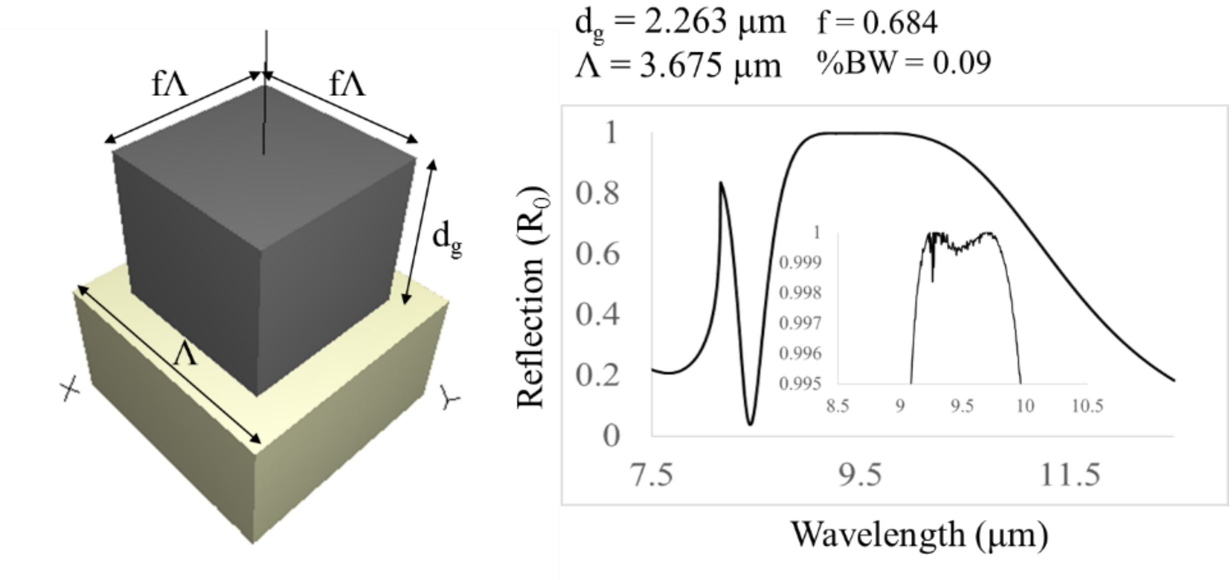

Figure 3.6 - 2D HCG post design.

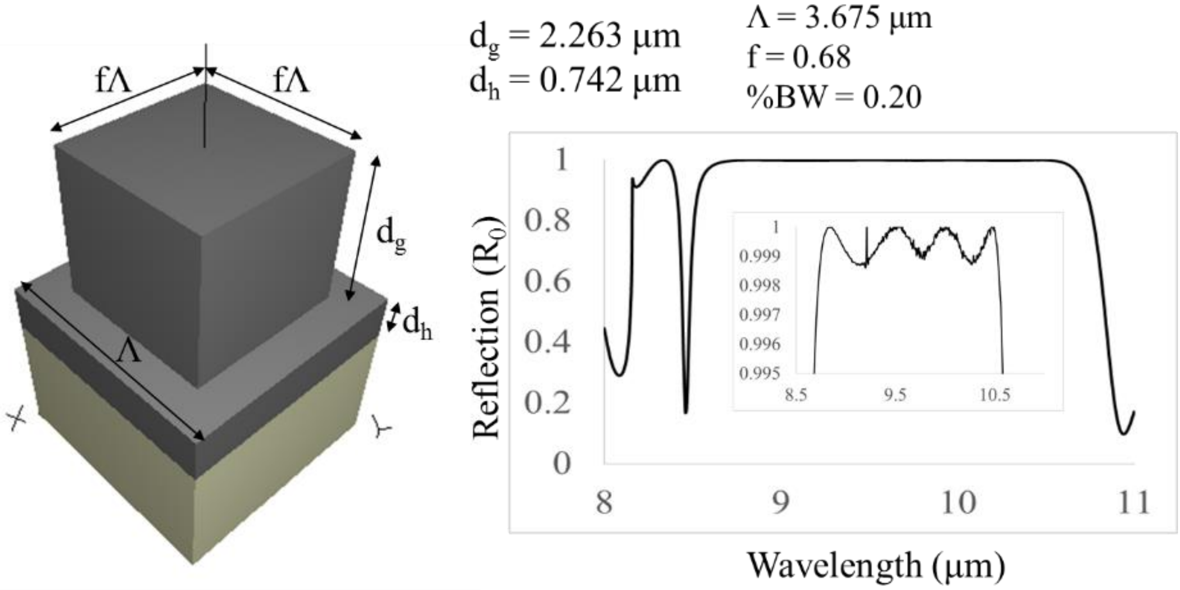

Figure 3.7 - ZCG 2D post design and spectrum.

the homogenous high-index layer. With the 2D design, the effective index of refraction in the grating layer is significantly reduced from the 1D grating which causes the loss of a waveguide mode. The addition of even a relatively thin homogeneous layer beneath the post array raises the effective index and thickness of the device enough to create two additional $R_0 = 1$ modes and allows for a bandwidth comparable to the 1D HCG design.

3.2.5 Substrate material selection

Zinc sulfide is chosen as the device substrate due to its low-index of refraction and physical robustness. However, there are two different grades of material available from commercial suppliers that present slightly different optical characteristics.

Standard grade ZnS is translucent with a pale yellow coloration. It is manufactured using a chemical vapor deposition (CVD) process that results in a robust material suitable for transparent IR windows in the LWIR range of 8 – 12 μm. Multi-spectral zinc sulfide (ZnS-MS) is a form of CVD grown ZnS that has been heat and pressure treated to remove deformities and results in a nearly mono-crystalline material. It is water transparent in color and exhibits uniform transmission from the visible range through the LWIR.

Figure 3.8 shows a comparison between ZnS and ZnS-MS samples ordered from II-VI Infrared measured with Fourier transform infrared (FTIR) spectroscopy in our lab. In it we see that while standard grade ZnS presents acceptable transmission in the IR bands, ZnS-MS demonstrates a flatter response and slightly higher transmission across the entire MWIR and LWIR range. Figure 3.9 shows the results of an x-ray diffraction (XRD) measurement of a standard grade ZnS and a ZnS-MS sample. We see in Fig. 3.9 a) that the ZnS sample displays several diffraction peaks with significant intensity which result from its polycrystaline structure.

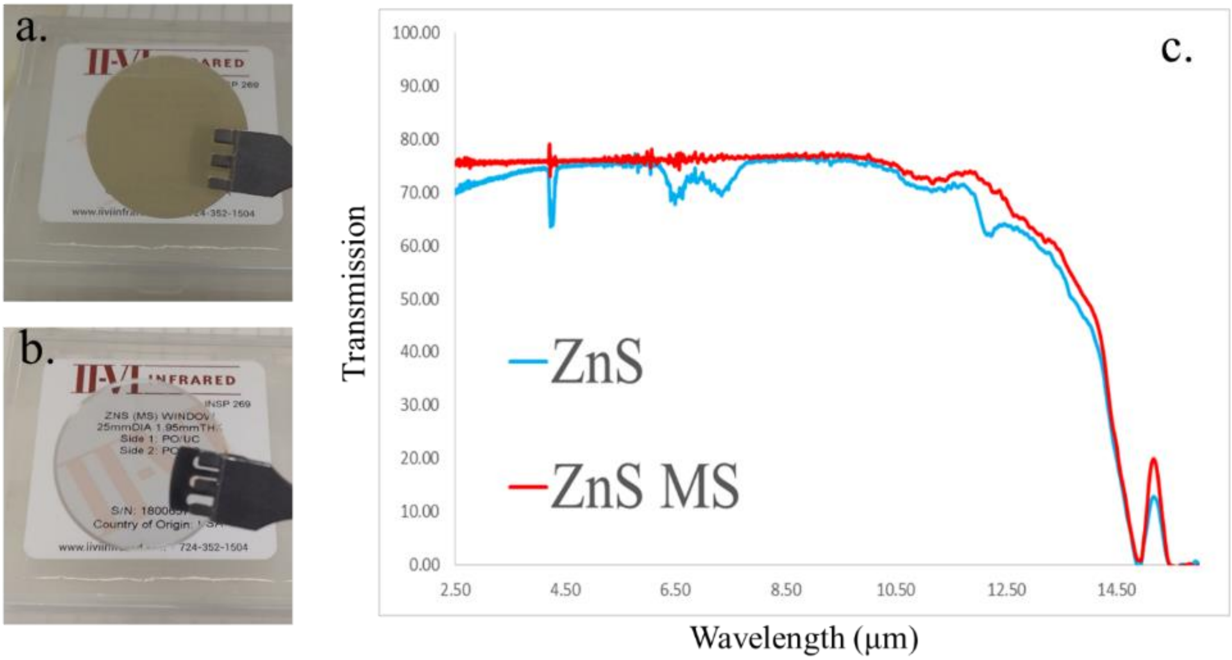

Figure 3.8 - ZnS and ZnS-MS comparison. a) Standard ZnS wafer showing translucent yellow coloration. b) Transparent ZnS-MS wafer. c) FTIR transmission measurements of the ZnS and ZnS-MS wafers. Transmission losses in both cases are primarily due to reflection.

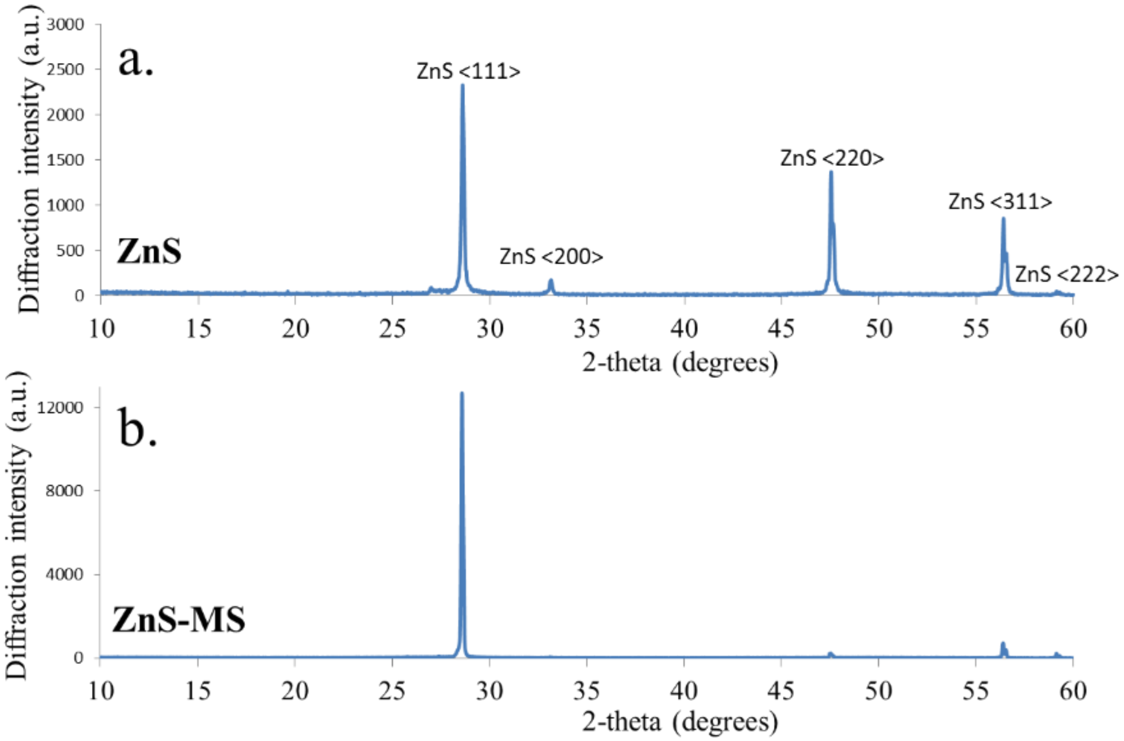

Figure 3.9 - ZnS and ZnS-MS XRD analysis. a) ZnS results showing multiple diffraction planes. b) ZnS-MS results demonstrating high degree of mono-crystallinity.

The ZnS-MS result in Fig. 3.9 b) is dominated by the <111> plane diffraction intensity which demonstrates its nearly uniform crystallinity.

3.3 Device fabrication and measurement

A proof of concept 1D HCG device is fabricated based on the design shown in Fig. 3.5 a). This is the simplest design from a fabrication tolerance standpoint as it requires only a well controlled deposition of the germanium layer thickness. The HCG design allows the ZnS to function as an etch stop layer and prevents over-etching of the device due to any variances in the etch step. The fabrication of the device follows from the general procedure reported in Chapter 2. Specific results pertaining to the device under fabrication are reported here.

Fabrication begins with the selection of a 1.95 mm thick, 25 mm diameter ZnS-MS wafer as the device substrate. The wafer is cleaned in a 20 minute ultrasonic acetone bath followed by a 20 minute ultrasonic IPA bath followed by a DI water rinse. The wafer is dried using dry N_2 and placed on a 115^0 C hotplate for 1 minute for a dehydration bake. The wafer is then transferred to the OxfordLab 80 Plus RIE chamber where it is cleaned with an O_2 plasma for 4 minutes at 200 W and 50 sccm O_2 flow rate. This is followed by an Ar plasma for 4 minutes at 200 W and 35 sccm gas flow rate. At this point the wafer is ready for film deposition.

The Ge surface adhesion layer is deposited using the homebuilt sputter chamber in the UTA nanofab. The layer is deposited with an initial pumpdown to $2x10^{-6}$ mT, 100 W plasma power, 40 mT strike pressure, 3.5 mT process pressure, 15 rpm stage rotation, 120 second presputter and 240 second sputter time. The Ge device layer is then deposited using the nanofab e-beam evaporator solution. 99.999% pure Ge pieces are loaded into the chamber crucible. The Ge deposition parameters are set under “film 11” in the e-beam evaporator control software. Deposition rate is set to 4 Å/s; total deposition thickness is set to 22.000 kÅ. Total deposition time is approximately 1.5 hours. The Ge coated wafers are then transferred to the Lab18 sputter system within the nanofab cleanroom for Si passivation layer deposition. The recipe used is “Daniel Si deposition full auto” with presputter time set to 120 seconds and sputter duration set to 480 seconds. Completed wafers are removed from the Lab18 sample holder and will display a dull gold tinge resulting from the Si thin film effects as shown in Figure 3.10.

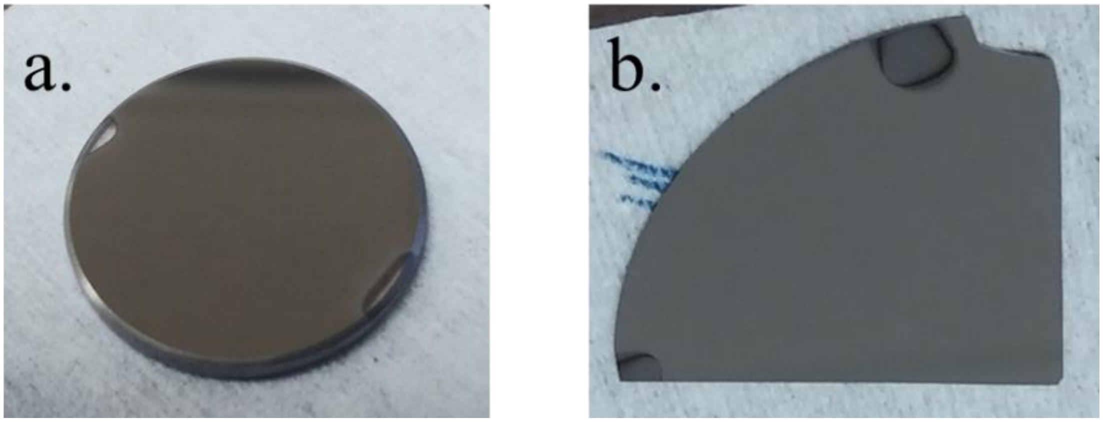

Figure 3.10 - Completed Ge-ZnS device blank comparison. a) Ge coated ZnS wafer with Si passivation layer present resulting in gold coloration. b) Si wafer shard coated with Ge but no passivation layer showing dull silver coloration.

The next step is photoresist spin coating and photolithographic pattern transfer. The Brewer model 200 spin coating machine in the NDG cleanroom is used for the spin coating process. The spin coating chamber is first prepared with an injection nozzle made from thin capillary tubing connected to a standard syringe which will be used to dispense the edge bead removing solvent during the spin coating process. This setup is shown in Figure 3.11. The spin coating recipe used is DC4150-ER which has been programmed with a two part process consisting of a 40 second spin coating at 4150 rpm which is followed by a 3000 rpm, 20 second process to allow dispensation of the edge bead solvent. The syringe is loaded with 1 to 1.5 mL of Microposit EC-11 edge bead remover solvent for each wafer that will be processed.

Just prior to loading, the sample is blown with dry N_2 to remove any surface particles that may have deposited during transit. If the sample has been sitting for an extended period of time, it can be gently rinsed with DI water, blown dry and placed on a 115^0 C hotplate for 60 seconds to dehydrate. After this the sample is blown off a final time as before and loaded into the spin coating chamber. Microposit s1813 positive photoresist is dispensed onto the wafer using a

Figure 3.11 - Spin coating chamber with attached solvent injection nozzle.

plastic lab pipette until the liquid forms a uniform bead across the wafer. The chamber is then closed and the spin coating program is run.

After the initial 40 second spin coating, the EC-11 solvent is dispensed onto the wafer using firm and steady pressure on the syringe plunger to ensure a smooth and steady stream of liquid. Care must be taken in this step to avoid any errant drops or splashing of the solvent which will render the spin coating non-uniform and unfit for use. The solvent stream is directed as it is being dispensed by using light pressure on the rigid piece of tubing that enters into the chamber. The stream is gently moved back and forth to wash the edge of the wafer and leave a uniform, circular patch of photoresist remaining in the middle. If a non-circular substrate is being used in this step, all photoresist must be removed from the edges of the wafer resulting in a circular patch of photoresist that resides entirely within the wafer boundaries. Anywhere that the photoresist touches the edge of the wafer will result in the presence of an edge bead and subsequent exposure misalignment.

After spin-coating, the wafer is transferred to a 115^0 C hotplate for 60 seconds as a softbake to drive off remaining solvent. When baking the thick ZnS samples, it is important to allow them adequate time to cool on a cold plate prior to placing them in a transport carrier. The added thickness and mass results in more heat retention, and a heated sample will quickly melt and fuse to a plastic sample tray. After being allowed to cool and being placed in a tray, the carrier is wrapped with a layer of aluminum foil to protect the now sensitive photoresist coating from accidental exposure. The coated samples have been tested to be stable for at least one hour between coating and exposure, but the exposures should take place as soon after spin coating as possible to ensure the best results.

The devices are transported to the nanofab using the petri dishes containing them with double layered aluminum foil liners. The exposures are carried out using an EVG-620 contact mask aligner. This system accepts either 5” or 7” square masks and has sample chucks designed for 4” to 6” wafers. As the devices being fabricated in this case are much smaller than the minimum chuck size, a 4” carrier wafer is employed to hold the sample during exposure. The mask used is a 5” chrome on glass template fabricated at the UT Dallas cleanroom with a Heidelberg system. The grating pattern is first laid out using CAD software and saved as a .dxf format for use in the Heidelberg equipment. The pattern is designed for a positive photoresist exposure with $\Lambda = 3.67$ μm and dark space fill factor of 0.66. These dimensions are very close to the resolution limits of the EVG-620 system, and to minimize the chances of misalignment during exposure, the pattern to be exposed should be placed in the exact center of the mask in order to ensure even pressure is placed on the sample during contact.

The mask, carrier wafer, and sample thickness are measured with a digital caliper and entered into the exposure software with the carrier wafer and sample thickness measurements being combined together. Mask thickness in this case is 2.13 mm, carrier wafer is 0.56 mm, and the ZnS wafer is 1.95 mm. The settings entered serve as a general guide for the equipment, but do not need to be exact. For instance, if several similarly sized wafers are to be exposed in a batch process, the average thickness can be entered into the program without causing issue. The carrier wafer should also be exposed and developed with the mask pattern prior to this step. This allows the wafer to serve as a placement template for the smaller device samples. Exposure energy is set to 74 mJ/cm^2 and hard contact pressure is set to 1150 mT.

The mask is cleaned before each use by rinsing with acetone followed by IPA and blown dry with compressed N_2. The mask surface should never be cleaned with any sort of physical wipe as this can easily damage the etched pattern. If any visible residue remains on the surface, the rinsing cycle can be repeated as necessary. The mask chuck is cleaned with IPA and a cleanroom lab wipe to ensure good vacuum contact. The mask and carrier wafer are then loaded into the aligner according to the onscreen prompts. The samples are placed onto the carrier wafer using the pre-exposed pattern as a guide. Prior to loading they are blown off with compressed N_2 a final time to remove any particles that may have been deposited in transit as the surface must be absolutely flat to produce a reliable exposure. During each exposure, the tray containing any additional samples is generally covered to prevent any incidental UV light from striking them.

The exposed samples can be developed in the nanofab cleanroom, or, if preferred, can be transferred back to the NDG lab. If the samples are to be transferred, their carrier must be securely re-wrapped in aluminum foil as they are still photosensitive at this point. Prior to development, the exposed wafers are placed on a 115^0 C hotplate for 60 seconds as a post exposure bake to smooth out any minor pattern irregularities. They are then developed by immersing in Microposit MF-321 developer for 60 seconds followed by rinsing in DI water and blown dry with compressed N_2. The developed samples can then be placed back on a 115^0 C hotplate for 10 to 20 minutes as a final hard bake to prepare for etching.

Device etching is performed using the NDG OxfordLab 80 Plus reactive ion etcher using the “DANIEL GE ETCH CYCLED V.4” recipe. This recipe etches evaporated germanium at a rate of 39.85 nm/cycle, and is set to a 55 cycle etch to achieve the 2.2 μm depth. Each cycle is 29 seconds long which results in 26.6 min total etch time. After etching, the remaining photoresist is removed using O_2 ashing for 4 minutes followed by a 20 minute immersion in AZ-400T photoresist stripper to remove any remaining hardened resist. The wafer is then rinsed with acetone, IPA, and DI water, and then blown dry with compressed N_2

The physical dimensions of the device are characterized with AFM and SEM measurements, however, the grating height of 2.2 μm can prove difficult for AFM tip to accurately measure, and the ZnS substrates will shatter if an attempt to cleave them is made in order to produce a cross section for viewing under SEM. The work around for this is to create a dummy device on a silicon wafer in parallel with the ZnS device. The deposition and lithography steps are all performed at the same time, and the final device and dummy wafer are both etched simultaneously to ensure identical etch conditions. The dummy device is then cleaved and viewed under SEM to verify the Ge layer thickness, etch depth, and etch profile. A topographic view of the ZnS device is taken with the SEM to verify the device fill factor. This results in accurate dimensions that can then be used to simulate the theoretical resonant response of the final device.

The spectral response is measured using a Nicolet iN10 FTIR with iZ10 transmission measurement attachment located in the NDG cleanroom. This device uses a blackbody radiator as its IR source and takes inherently unpolarized measurements. In order to record the TM response of the device, a 10,000:1 metallic wire grid polarizer effective from 7 to 15 μm is placed within the beam path in front of the sample holder. A 2 mm diameter aperture is placed behind the sample to allow for localized measurements, and remainder of the beam path behind the aperture is shielded with aluminum foil to reduce stray signals and noise. The FTIR projects a HeNe alignment laser beam along the beam path which is conveniently used to locate measurement points on the sample. The FTIR instrument and a close-up view of the sample stage is shown in Figure 3.12.

In order to provide accurate measurement results, a proper background measurement and calibration calculation must be performed. The devices as designed function as wideband reflectors, but the FTIR is only configured to take transmission measurements. A proper background measurement must therefore take into account not only the free-space propagation losses associated with the system, but also the losses incurred while transmitting through the bulk ZnS substrate. To accommodate this, the background measurement is taken with a blank ZnS wafer placed in the sample holder.

Included in the background measurement is the loss incurred by reflection from the front interface of the blank ZnS wafer. However, when making a device measurement, this front

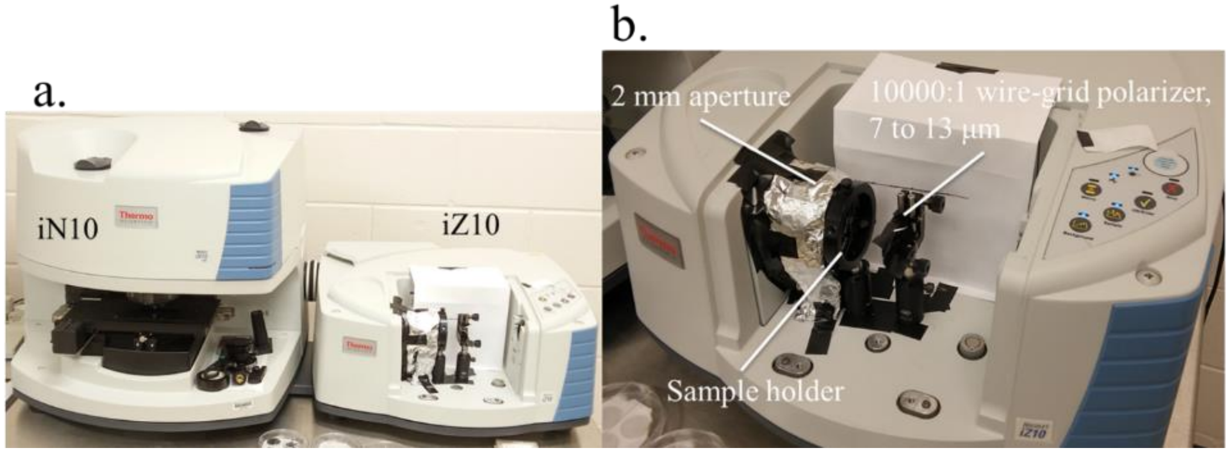

Figure 3.12 - FTIR instrument and sample stage. a) iN10 and iZ10 module configuration. b) detailed view of sample stage.

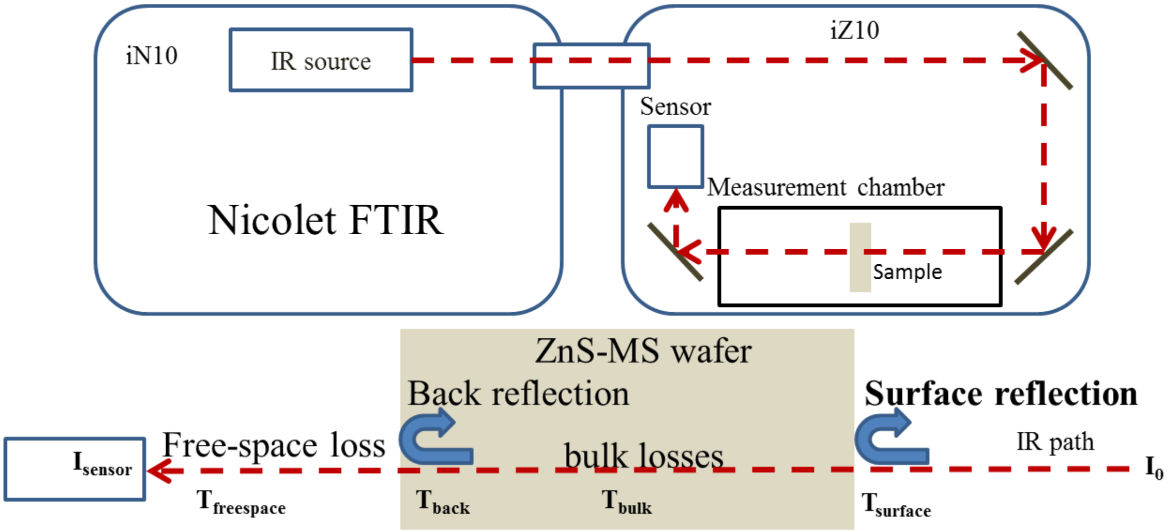

Figure 3.13 - FTIR measurement beam path and sources of transmission losses in background calculation.

reflection will no longer exist and will instead be replaced by the device response. This will result in the measurements being shifted by an amount equal to the inverse of the surface transmission. A schematic of the background measurement path and associated losses is shown in Figure 3.13.

Mathematically, the background signal recorded by the FTIR is the product of the nominal intensity of the IR source and the complete optical path transmission coefficient, or

$$\mathbf{I}_{\mathbf{background}} = \mathbf{I}_{\mathbf{0}} \cdot T_{background}, \text{ where } T_{background} = (T_{surface}T_{bulk}T_{back}T_{freespace})$$

After a background measurement is stored, the FTIR software reports results normalized by the relation $\mathbf{I}_{normalized} = \mathbf{I}_{sensor} / \mathbf{I}_{background}$. The background contains information about the surface transmission of a blank ZnS wafer, $T_{surface}$, but when measuring a patterned device, that surface transmission coefficient is replaced by the device response. The surface transmission coefficient needs to be removed from the normalized results, and this is done by multiplying the measured device transmission results by the coefficient’s value across the measured band.

Calculating the transmission coefficient is a trivial matter for a single interface and it can be found with the expression $T_{surface}(\lambda) = \frac{2\sqrt{\varepsilon(\lambda)}}{\sqrt{\varepsilon(\lambda)}+\sqrt{\varepsilon_0}}$ where ε_0 is the vacuum permittivity and $\varepsilon(\lambda)$ is the substrate permittivity as a function of the wavelength. Figure 3.14 shows the result of the calculation including full dispersion for an air-ZnS interface across the mid and long-wave IR along with the results of applying this re-normalization to a measured result.

As can be seen from the graph on the right in Fig. 3.14, the raw measurement data in blue using only the internal background measurement in the FTIR is shifted higher than the results predicted by calculations. In some cases, this can result in measurement results reported by the FTIR that exceed unity, which is a nonsensical result for a normalized measurement. But as the red curve shows, after multiplying the raw data by the calculated transmission coefficient for an air-ZnS interface, a very strong match is found between measurement and simulation.

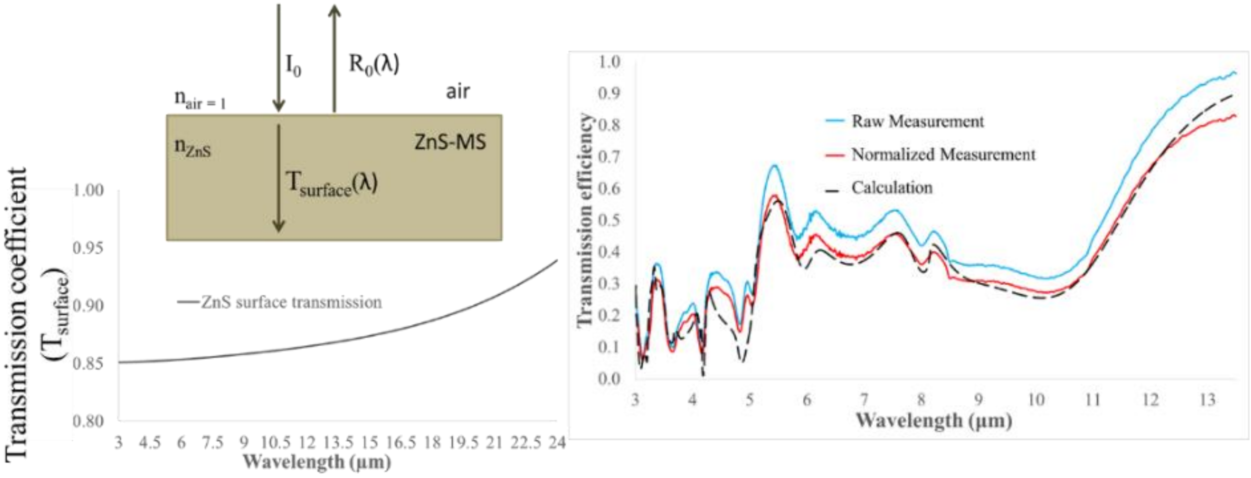

Figure 3.14 - surface transmission coefficient calculating and normalized measurement result.

3.4 Device results

SEM images of the fabricated wideband HCG device are shown in Figure 3.15. Figure 3.15 a) is a cross-section of the dummy Ge on Si device showing the rectangular grating profile

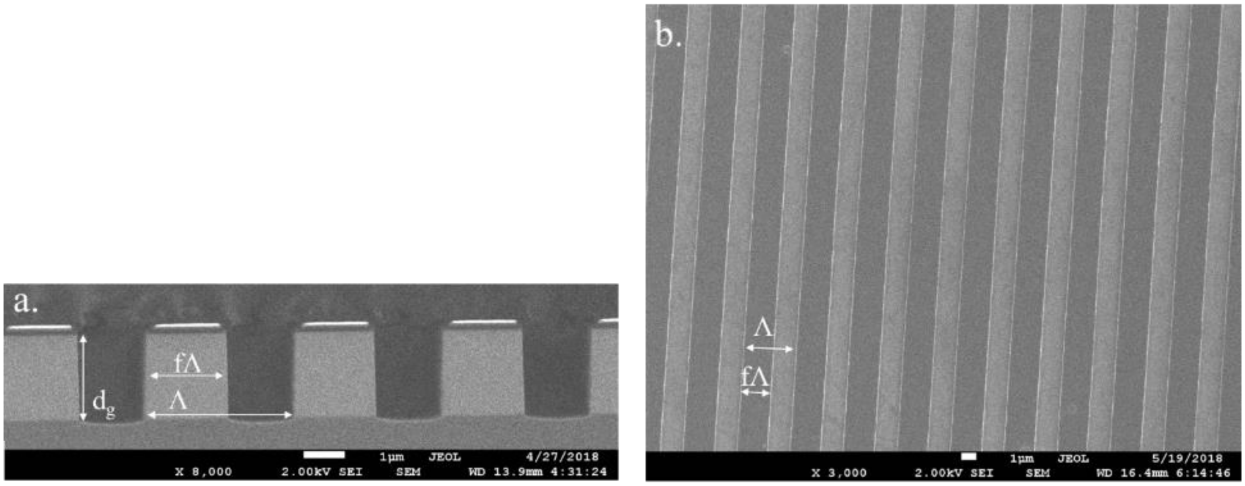

Figure 3.15 - HCG device SEM images. a) cross-section of Ge on Si dummy device. b) Top-down view of Ge on ZnS device. Final dimensions are $\Lambda = 3.67$ µm, dg = 2.2 µm, and f = 0.55.

and allowing measurement of the grating height, period, and fill factor. On top of the grating is residual photoresist that was not removed from the dummy device. Figure 3.15 b) shows a top-down view of the Ge on ZnS device. The dark bands are the germanium grating, the light bands are the ZnS substrate underneath. This view was used to verify the uniformity of the device as well as the final fill factor.

The fabricated device dimensions are $\Lambda = 3.67$ µm, $d_g = 2.2$ µm, and f = 0.55. Fill factor losses were significant and resulted from the profile of the photoresist mask. The exposure mask was fabricated using the exact design specifications of f = 0.66, but the thickness required of the photoresist results in a tapered photoresist profile as was shown in Fig. 2.16. This trapezoidal shape creates sidewall losses as the etch progresses and the photoresist profile is eroded. The final result is the loss of fill factor as seen in the fabricated device.

Figure 3.16 shows transmission measurement results and calculated spectra for the device that includes background normalization and surface reflection calibration as described in Section 3.3. Results are shown for the unpolarized spectrum from 3 to 13.5 µm and for TE & TM polarized measurements taken within the 7 to 13.5 μm range of the 10,000:1 wire grid polarizer. Figure 3.16 a) shows the unpolarized results, b) shows the results for TE polarization, and c) show the TM spectrum demonstrating the wideband response. Included also in the TM graph is the predicted reflection response calculated by assuming minimal scattering and absorption losses and then using the relation $R_0 = 1 - T_0$.

As can be seen, there is excellent agreement between theory and measurement, even in the short wavelengths below the Rayleigh point where higher order scattering is present and where fabrication defects would have a larger impact. The TM spectral map is especially striking, as the extremely close overlap between theory and measurement is testament to the

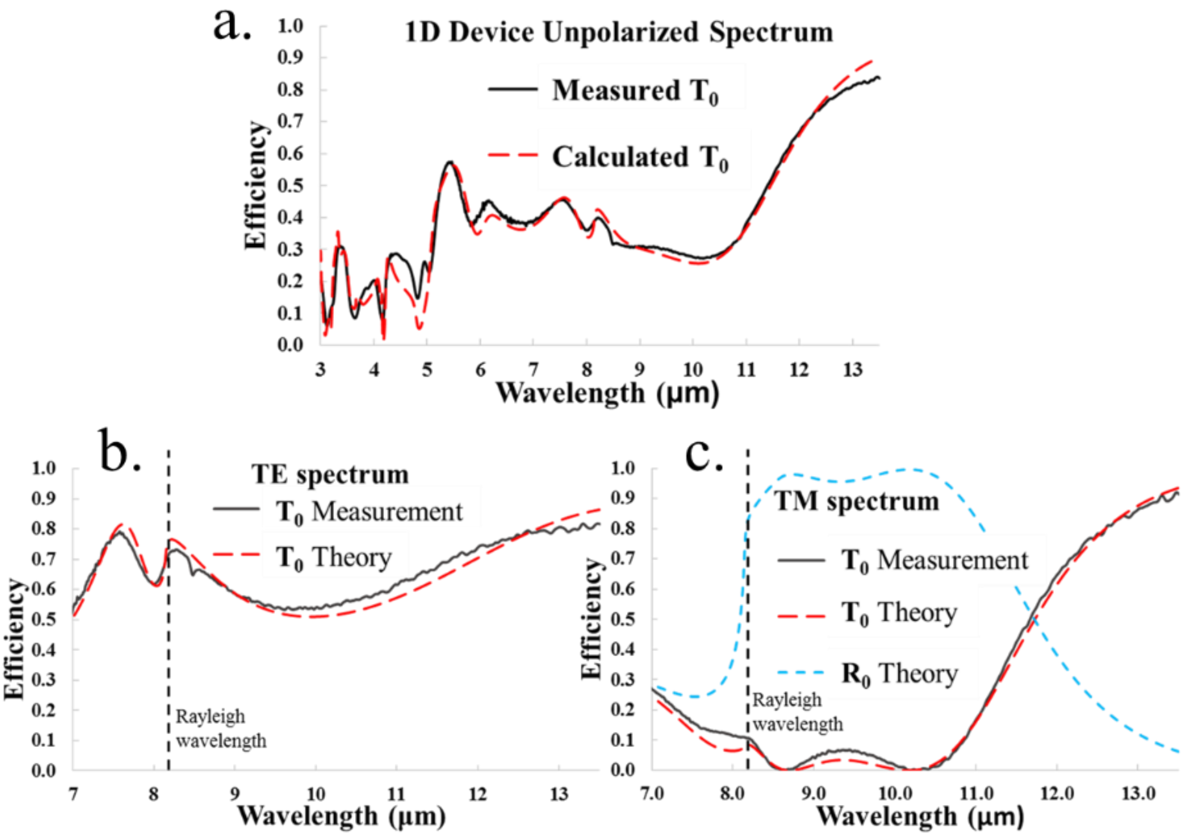

Figure 3.16 - Fabricated HCG device measurements. a) unpolarized spectrum. b) TE polarization results. c) TM polarization results including predicted R_0 response.

accuracy of the design and fabrication. These results provide validation for the wideband reflector designs in the LWIR, and, importantly, strong validation of the ability of the developed fabrication process to produce a high-quality final product.

3.4.1 Further device refinement

The device results of Section 3.4 are an excellent demonstration of the ability to produce a wideband resonant device, but they are marred by the 0.55 device fill factor that results in a large reduction in the device bandwidth. Figure 3.17 shows the fill factor dependence of the device. Going from 0.66 to 0.55 results in the loss of a waveguide mode and corresponds to the reduction in resonant bandwidth. An investigation was made to see whether a technique could be developed to post-process the fabricated device in order to restore the lost fill factor and increase the corresponding resonant bandwidth.

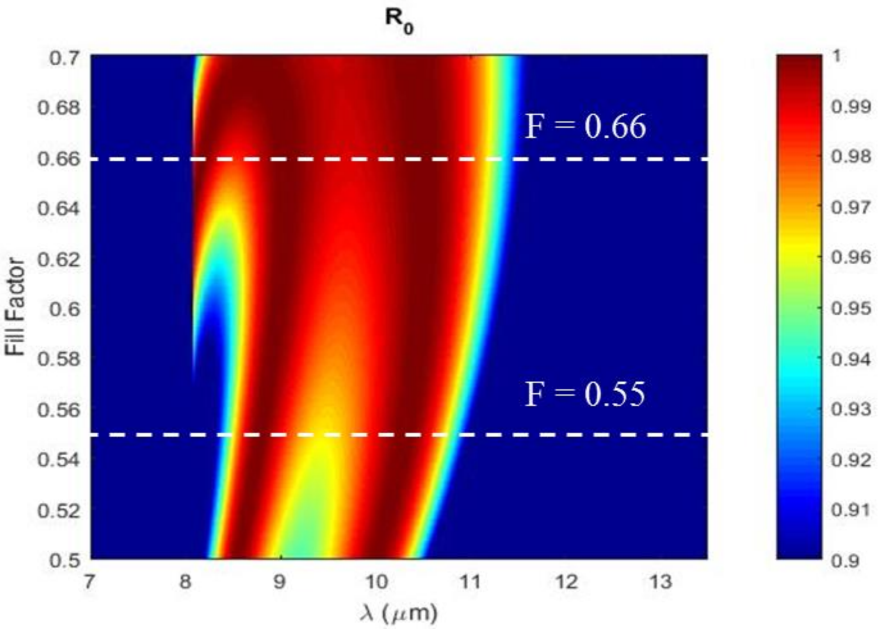

Figure 3.17 - Parametric sweep of fill factor impact on reflectance spectrum for HCG device.

Figure 3.18 shows the results of two different germanium depositions performed to see whether additional material could be grown on top of the gratings. Figure 3.18 a) shows the result of using the e-beam evaporator solution in the UTA nanofab to deposit an additional 500 nm of material. The e-beam deposition chamber is conFigured in an anisotropic deposition mode, and the resulting profile is exactly that which would be used in a classical deposition-liftoff operation. The vertically deposited material gathers at the corners of the device gratings and builds outward, gradually forming a shadow region for material deposited in the trench and resulting in trapezoidal deposition profiles. A key observation in this case is that there is no noticeable sidewall deposition, which would preclude it from use in the goal of increasing the fill factor.

Figure 3.18 b) shows the results of a sputter deposition using the homebuilt sputter system in the UTA nanofab. In this case, there is a clear conformal layer that has been grown on top and sides of the grating. However, inspection of the profile shows that roughly three times as much material has been deposited on top of the grating as along the sidewalls and within the trenches, and has resulted in a distorted jewel or coffin like shape in the grating. This extra

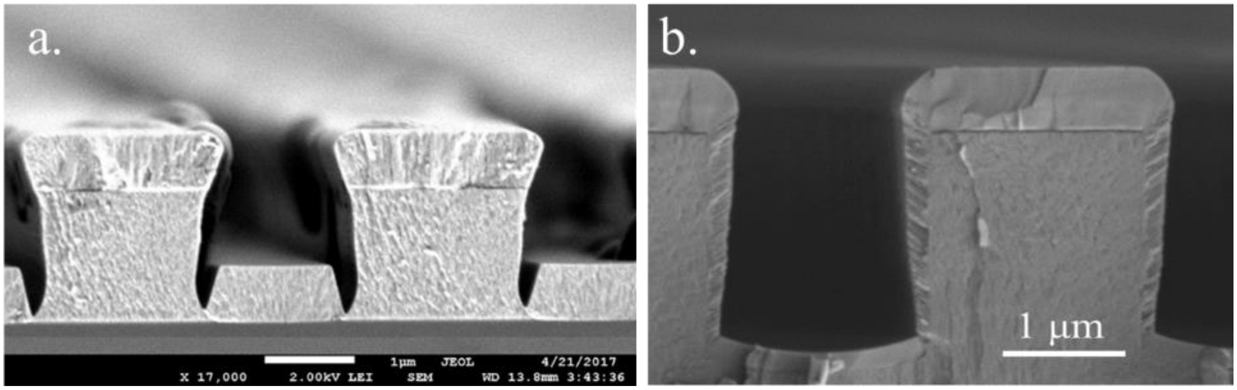

Figure 3.18 - Film deposition comparison. a) 500 nm e-beam evaporated Ge film on a Ge grating. b) Conformal sputtered Ge film on a Ge grating.

material will adversely affect the resonance and counteract any benefits gained from an increase in fill factor as shown in a simplified simulation in Figure 3.19. Part a) shows a simplified schematic that ignores the non-uniform shape of the device with $\Lambda = 3.67$ µm and an assumed ideal fill factor of $f = 0.66$. In Fig. 3.19 b), the reflectance is calculated in response to the trench depth deposited, d_h where the grating height d_g will increase by an amount equal to $2d_h$. This calculation shows that even with an ideal fill factor of 0.66, the wideband resonance will quickly be lost if the grating height deviates from the designed value of 2.2 µm.

The solution to this dilemma is provided by the HCG design. As the ZnS is negligibly etched by the Ge etch recipe, the tops of the grating can be etched down prior to deposition without meaningfully impacting the trench depth. After this, the additional material deposited on the tops of the grating will recover the lost grating height while simultaneously filling out the sidewalls.

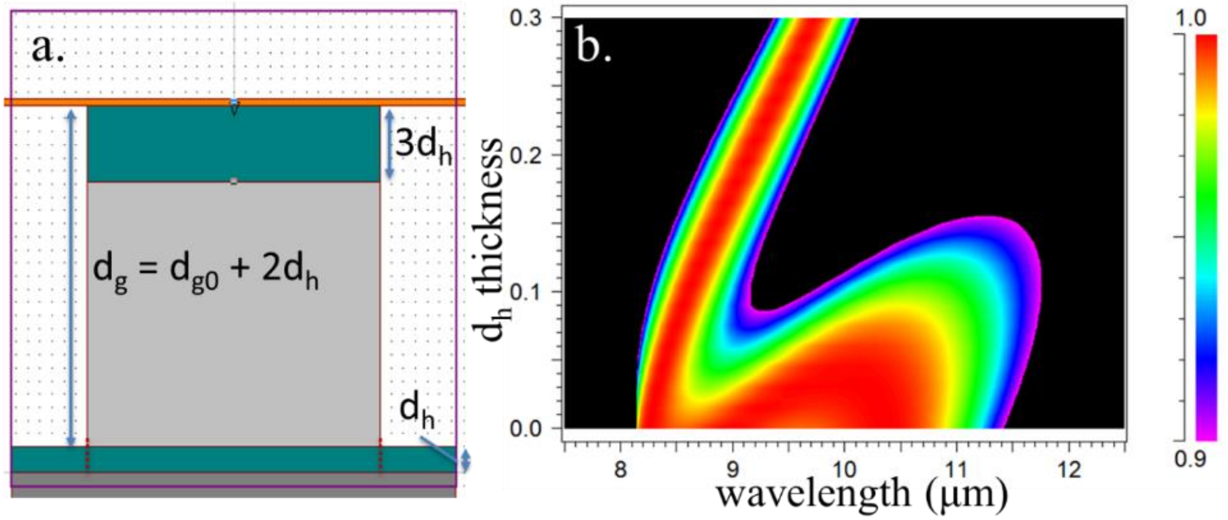

Figure 3.19 - Conformal coated device parametric analysis. a) simplified device schematic. b) resonant spectrum in response to increasing d_h thickness.

The fabricated Ge – ZnS device is thus placed in the Oxfordlab RIE chamber and etched for 10 cycles using the V.4 cycled etch recipe. The device is then placed in the homebuilt sputter with an initial pumpdown to 2×10^{-6} mT, 75 W plasma power, 40 mT strike pressure, 3.5 mT process pressure, 15 rpm stage rotation, 120 second presputter and 2851 second sputter time for an estimated deposition of 200 nm along the sidewalls and in the grating trenches and 600 nm on the ridges.

The results of the device post-processing are shown in Figure 3.20. The device spectrum is simulated using an approximate shape outlined in Fig. 3.20 d). Parameters used are $d_g = 2.14$,

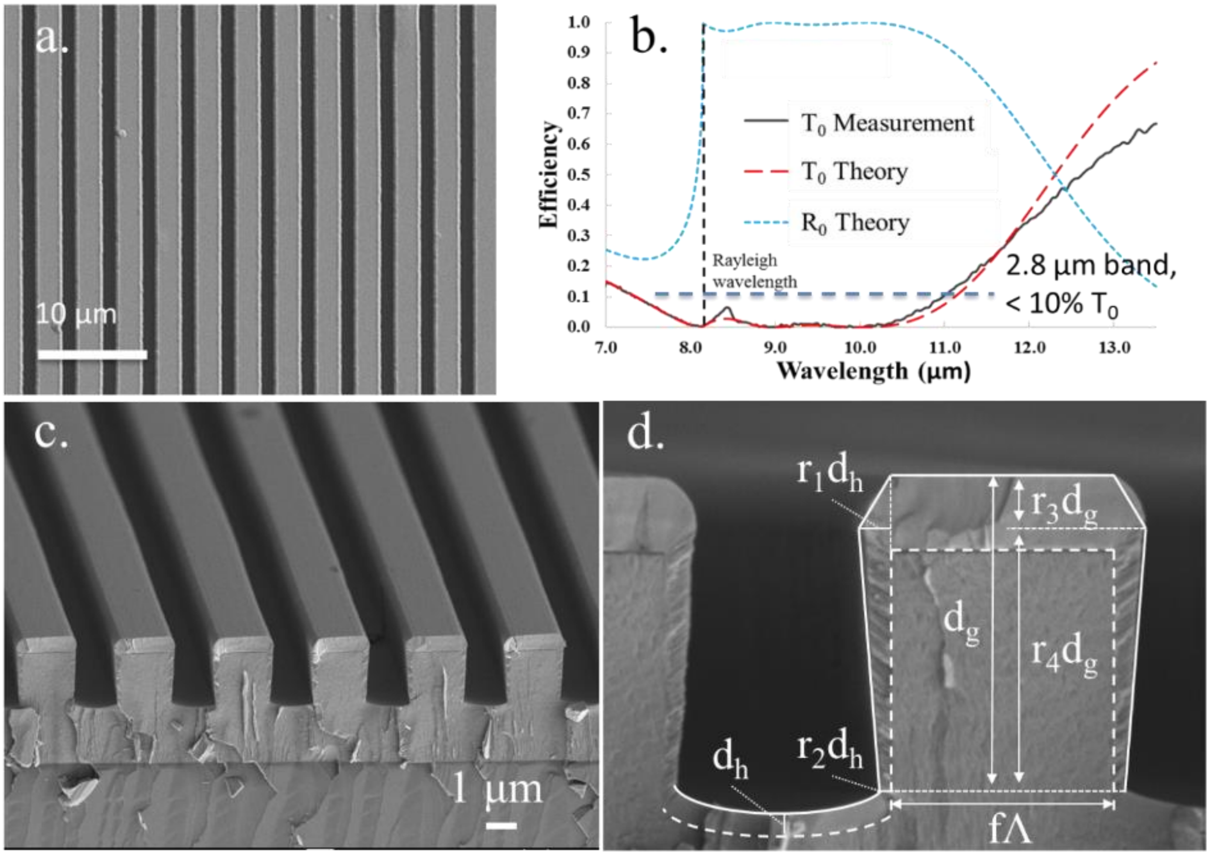

Figure 3.20 - Conformally coated wideband device results. a) Top-down view of the final device. b) Measured and calculated spectrum showing an increase in bandwidth and flattening of resonant response. c) Cross-sectional view of dummy device showing uniformly coated grating. d) Cross section of a single device period outlining simulation parameters used.

$d_h = 0.15$, $r_1 = 1.182$, $r_2 = 0.612$, $r_3 = 0.102$, $r_4 = 0.898$, $f = 0.54$, $\Lambda = 3.67$, and are based off measurements made from the SEM cross-section. Figure 3.20 a) shows the top-down view of the device where again the dimensions can be cross-referenced with those of the dummy device cross-section to verify the proper ratios are used. Figure 3.20 b) shows the new spectrum measurement and calculations. As predicted, the resonant response has flattened significantly, and another $R_0 = 1$, $T_0 = 0$ node has been brought into the resonance at the Rayleigh point, widening the overall response.

3.5 Conclusions

In this chapter it was shown how the fabrication techniques developed in chapter 2 can be implemented to create a resonant wideband LWIR device. Design methodology is discussed that allows for rapid prototyping of a device exhibiting a desired response, and designs are presented for four wideband germanium – zinc sulfide devices. A proof of concept sample is fabricated based on the 1D HCG design and is used to demonstrate the accuracy of the fabrication and measurement techniques, but also the pitfalls that can occur when device tolerances are not taken into account during the initial design phase.

A novel fabrication step is then presented that attempts to improve the spectral response of the fabricated device by sputtering a conformal layer of additional material in order to restore fill factor lost in the etching process. The process is largely successful and demonstrates the robustness of the resonant response even in non-standard device geometries as well as the power of simplified computer models to correctly predict the behavior of complex grating designs.

The design and fabrication methodology presented here can serve as a template for the fabrication of additional wideband devices including ZCG and 2D unpolarized implementations.

It can also be used as a general guideline for any germanium based device operating in the LWIR and will be a useful tool as research continues to expand into this region.

Chapter 4 Infrared refractive index of sputtered germanium films

4.1 Introduction

When working with thin films, the structural morphology of the film, be it crystalline, polycrystalline or amorphous, and the resulting material density, void percentages, and grain boundary size will have a strong impact on the electro-optical properties [64] [65] [66] [67]. The structure of the deposited film can be controlled based upon the deposition method employed. Amorphous films are readily deposited via sputtering or thermal and electron-beam evaporation. Polycrystalline silicon films useful in solar cell production and other semiconductor technologies can be deposited using chemical vapor deposition (CVD) or through thermal annealing of amorphous films [67] [68] [69]. CVD processes as well as wet chemical and thermal annealing can also be used to deposit crystalline or near-crystalline (nc) films [70] [71].

Previous studies on the deposition of amorphous germanium (a-Ge) films have shown that the method of deposition used will influence the material composition of the film, the material density, and optical constants [72] [73]. Ellipsometry measurements from the ultraviolet to the near IR (275 nm to 826 nm) demonstrated that in general, sputtered deposition grown films will have higher valued dielectric constants than those grown via e-beam evaporation [73]. Studies of RF sputter deposited a-Ge films have also demonstrated films with higher density that intrinsic crystalline germanium (c-Ge) [74].

In this chapter, the optical properties in the mid to long-wave IR are studied for germanium films ranging from 850 nm to 3950 nm in thickness prepared via RF sputter deposition. Energy-dispersive spectroscopy (EDS) is used to verify the material composition of the films, and x-ray diffraction is used to study the material morphology. The index of refraction of the deposited films is characterized through FTIR Fabry-Perot thin film transmission measurements and through the fabrication of GMR devices designed with characteristic resonant markers. The measured resonant position of these markers acts as an index of refraction sensor for the material itself, similar in function to a GMR biosensor acting on a deposited bio layer [75].

4.2 Initial device observations

Anomalous index of refraction measurement results in a sputtered Ge film were first observed in the attempted fabrication of a ZCG GMR device based on the design shown in Fig. 3.2. The design requires 4 μm of Ge to be deposited on a ZnS substrate. The ZnS substrate was cleaned and prepared accorded to the procedure described in Chapter 2. The Ge layer was deposited using the Lab18 system in the nanofab due to the capability to deposit the entire 4 μm in a single growth cycle versus a multi-part growth that would be required using an e-beam evaporation system as discussed in Chapter 2. The recipe used for the Ge deposition is "Lee HfO2 Gun1", with relevant process parameters of 150 W deposition power, 25 sccm Ar flow rate, and 3.3 mT process pressure. Estimations based on previous depositions put the required deposition time at 40,313 seconds. After film growth, the Ge was coated with a Si passivation layer using Lab18 with a 480 s deposition time, 3.3 mT process pressure and 200 W power.

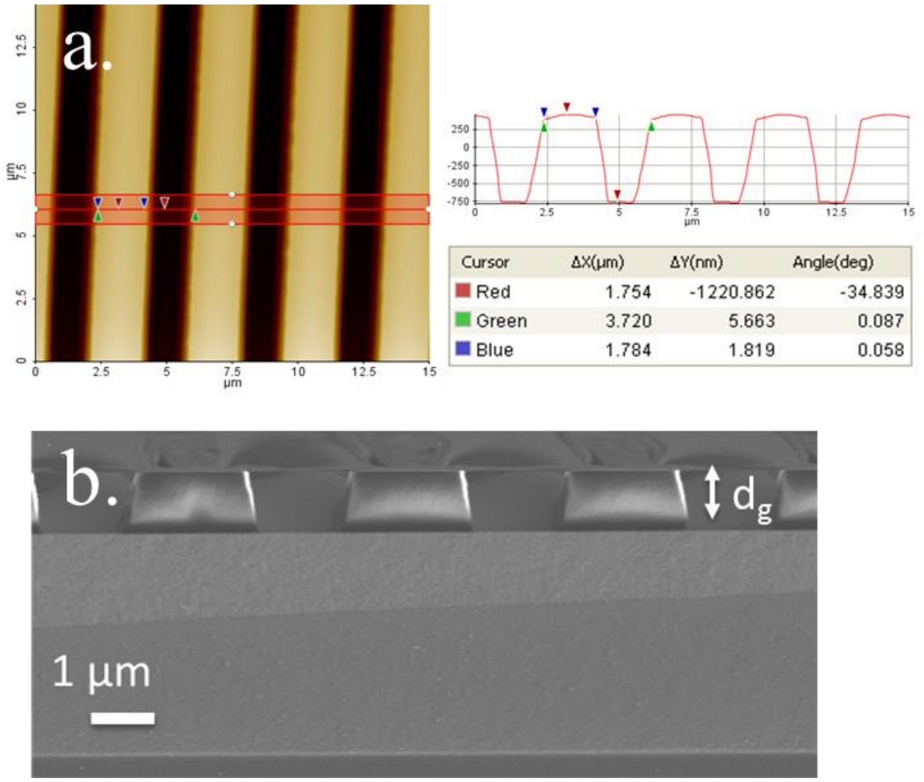

Cursor	ΔX(µm)	ΔY(nm)	Angle(deg)
🟥 Red	1.754	-1220.862	-34.839
🟩 Green	3.720	5.663	0.087
🟦 Blue	1.784	1.819	0.058

Figure 4.1 - AFM and SEM measurements of 4 µm dummy device. a) AFM measurements of PR grating showing a PR height dg = 1220 nm. b) SEM cross-section of dummy device. Ge layer thickness measured to be 3950 nm.

The thickness of the Ge sputtered layer is measured via comparisons to a dummy wafer prepared in parallel consisting of germanium sputtered on a 50 mm silicon wafer. A photoresist grating is patterned on the dummy wafer and then measured with AFM. The wafer is then cleaved, and the cross section is examined under SEM. The AFM grating height measurements are cross referenced to the height measured through the SEM cross section, and the germanium film thickness is then determined from the SEM cross section measurements. The film thickness on the ZnS substrate is assumed to be identical to that of the dummy device as they were both prepared during the same deposition. Using the results of the AFM and SEM measurements shown in Figure 4.1, it was determined that the thickness of the sputtered Ge layer was 3950 nm.

The device was then patterned using s1813 positive PR and the EVG620 mask aligner in a similar fashion to the device fabricated in Chapter 3. An initial device was etched with a cycled RIE recipe developed using evaporated films. The result of this etching was an under-etched profile that did not meet the target depth of roughly 2200 nm. This result provided the first indication of a difference between the sputtered and evaporated film densities, as a more dense film would be expected to etch more slowly.

The number of cycles was adjusted and a second device was etched into a film that had been prepared in parallel with the first deposition. The results shown in AFM and SEM images in Figure 4.2. The physical size of the gratings makes AFM measurements difficult due to the inherent taper of the AFM stylus tip. To achieve an accurate reading of the trench depth, a scan was taken over a single 4 μm period with a scan rate of 3 Hz which is shown in Fig. 4.2 a). A SEM image showing the topology of the grating was taken with a 2kV beam at x8000 magnification and is shown in Fig. 4.2 b).

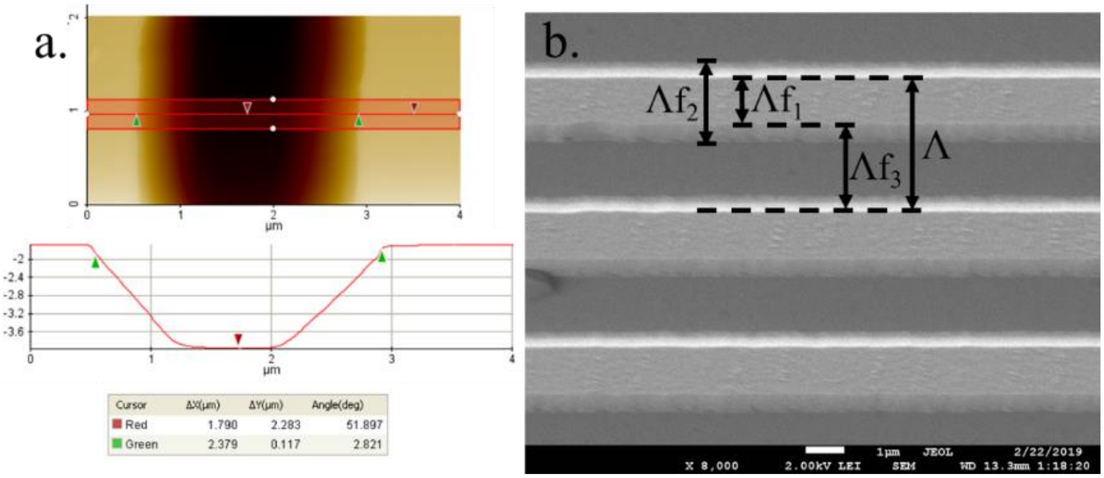

Cursor	ΔX(μm)	ΔY(μm)	Angle(deg)
🟥 Red	1.790	2.283	51.897
🟩 Green	2.379	0.117	2.821

Figure 4.2 -3950 nm device AFM and SEM measurements. a) AFM measurement of a single device period. b) top-down SEM scan allowing the characterization of physical dimension ratios.

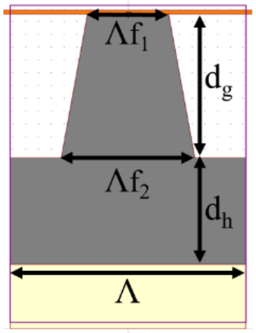

Figure 4.3 -3950 nm device model. $\Lambda = 3.67$ μm, $f_1 = 0.345$, $f_2 = 0.57$, $d_g = 2.283$ μm, and $d_h = 1.667$ μm.

The physical measurements indicate a profile that is tapered or trapezoidal in nature and is modeled as shown in Figure 4.3. Model parameters are $\Lambda = 3.67$ μm, $f_1 = 0.345$, $f_2 = 0.57$, $d_g = 2.283$ μm, and $d_h = 1.667$ μm. The f_3 parameter shown in Fig. 4.2 b) was used to cross reference with the trench width measured with the AFM in Fig. 4.2 a). The anomalous etching results ultimately led to a new etch characterization study for the sputtered films. The results of this study are those reported in Chapter 2 and resulted in a final, more robust etch recipe.

Although the device dimensions did not meet the design specifications, as an exercise the TE and TM transmission spectra of the device was measured for the 7.5 to 12.5 μm range and compared to model simulations as shown in Fig. 4.4. It is immediately apparent that significant differences exist between the measured and calculated results. What was not immediately clear was the cause of these discrepancies, as the measurement techniques and the dispersive models for Ge and ZnS used in simulation are the exact same as those used to model the devices shown in Chapter 3 where very good agreement was achieved.

The only difference between the device presented in Chapter 3 and the one with results shown in Figs. 4.2 – 4.4 is that the current device was fabricated using a sputtered germanium layer. Sputtered materials have been shown to have denser morphologies than those deposited

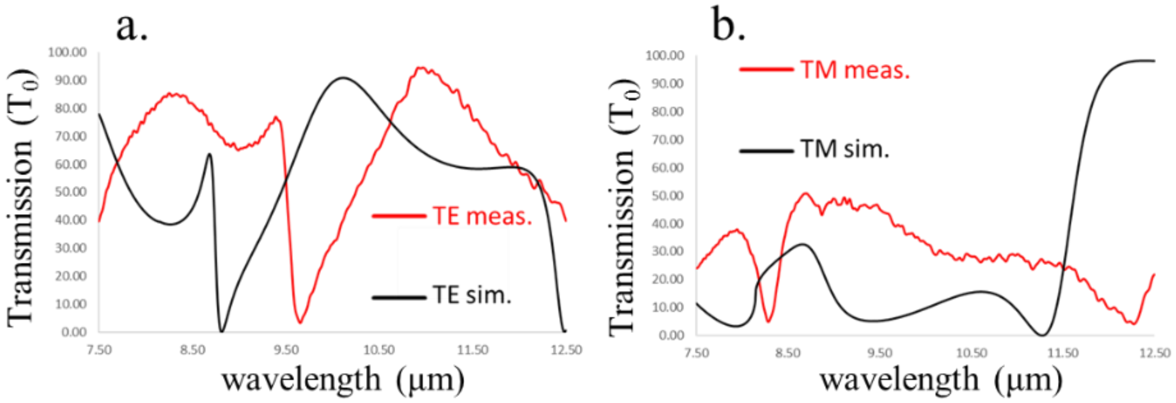

Figure 4.4 - Initial 3950 nm device measurement and calculation results. a) TE measured and simulation results. b) TM measurement and simulation results.

via evaporation methods, and their corresponding optical characteristics have been shown to differ as well [73] [74]. The index of refraction of intrinsic c-Ge at 10 μm is 4.005. If a static value of 4.41 is used in the simulations instead, the results are those as shown in Fig. 4.5. Here we see the simulations for both polarizations demonstrating a much closer match to the measured results. This represents a 10% increase in the intrinsic value for the index of refraction, and additional measurements are needed to confirm the results.

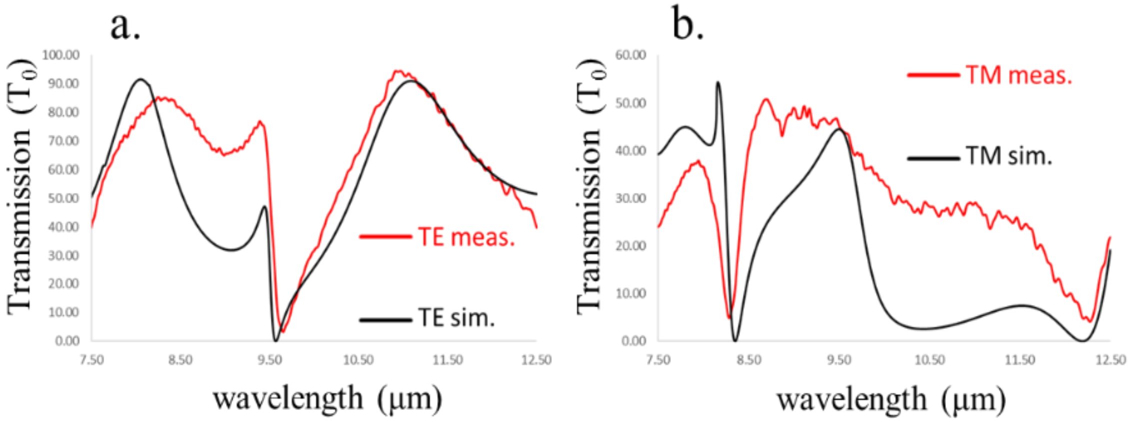

Figure 4.5 - Measured and simulated response for 3950 nm device using fit index of refraction. a) TE response. b) TM response. A static index of refraction n = 4.41 is used for both simulations.

Reflectometry and ellipsometry are common techniques used to measure the thickness and optical constants of a thin film. Surface reflections will add with waves that have traveled through the film and been back reflected from the second interface. The phase of the back reflected waves is dependent on the film thickness and its index of refraction, and the phase difference between the surface and back reflected waves will cause either constructive or destructive interference resulting in enhancement or diminishing of the observed response. If the film thickness is held constant and a range of wavelengths is swept over the surface, the measured reflected response will follow a chirped pattern as the back reflected waves cycle through a 2π range of phase shift. For a material with a dispersive index of refraction, response will generally be stretched towards the longer wavelengths as the index of refraction increases.

This result is of course known as classical Fabry-Perot interference [76]. Reflectometry is able to use this property to measure a film's thickness if the index of refraction is known, or to map the index of refraction if the thickness is known. Measuring the transmission response of a device can also be used to the same effect as the transmission curve will follow the reflection curve through the relation $T = 1 - R$ assuming negligible absorption.

The FTIR in the NDG cleanroom is thus employed to measure the transmission response of a homogenous region of the 3950 nm film. A region is selected adjacent to the patterned device area where a solid layer of photoresist prevented etching of the surface as is evident by the remaining golden-brown coloration due to the Si thin film layer. The device and measured response is shown in Figure 4.6. The measurement is compared to simulations, and as the thickness of the film is well characterized, the index of refraction of the film used in the simulation is adjusted to match the sinusoidal peak locations over the measurement range. This matching is easily accomplished manually by producing a two-dimensional plot of the peak

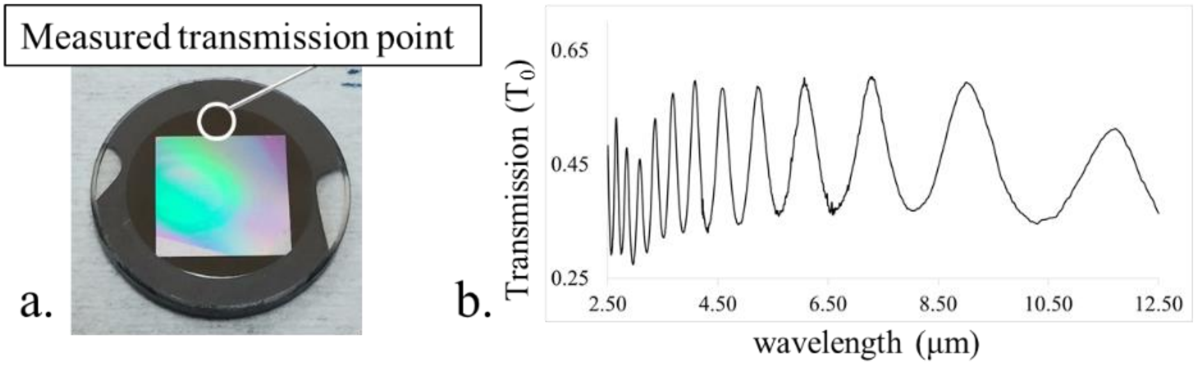

Figure 4.6 - 3950 nm device Fabry-Perot transmission measurements. a) Photograph of the device showing the thin film area to be measured. b) Thin film transmission result.

locations as a function of the index of refraction and then aligning the measured peak locations to the graph as shown in Figure 4.7. The matched points are plotted in Fig. 4.7 c), and are fit to a logarithmic trend line.

The data fitting again indicates a significant increase in the index of refraction. At 11.66 μm, the fit indicates n = 4.44, which is close in agreement to the value used in fitting the resonant spectrum simulation. For lower wavelengths, the values increase to an estimated value of n = 4.711 at 2.66 μm. This represents a very large increase in the index of refraction and is to the author's knowledge the first time such an increase is reported for sputtered germanium films in the mid and long-wave infrared. The results also demonstrate a generally dispersive curve fit, which lends credence to their representation of a real physical effect. As transparent, high-index materials are generally desirable in the fields of optics and photonics, additional experiments are designed to test and verify the reproducibility of the results.

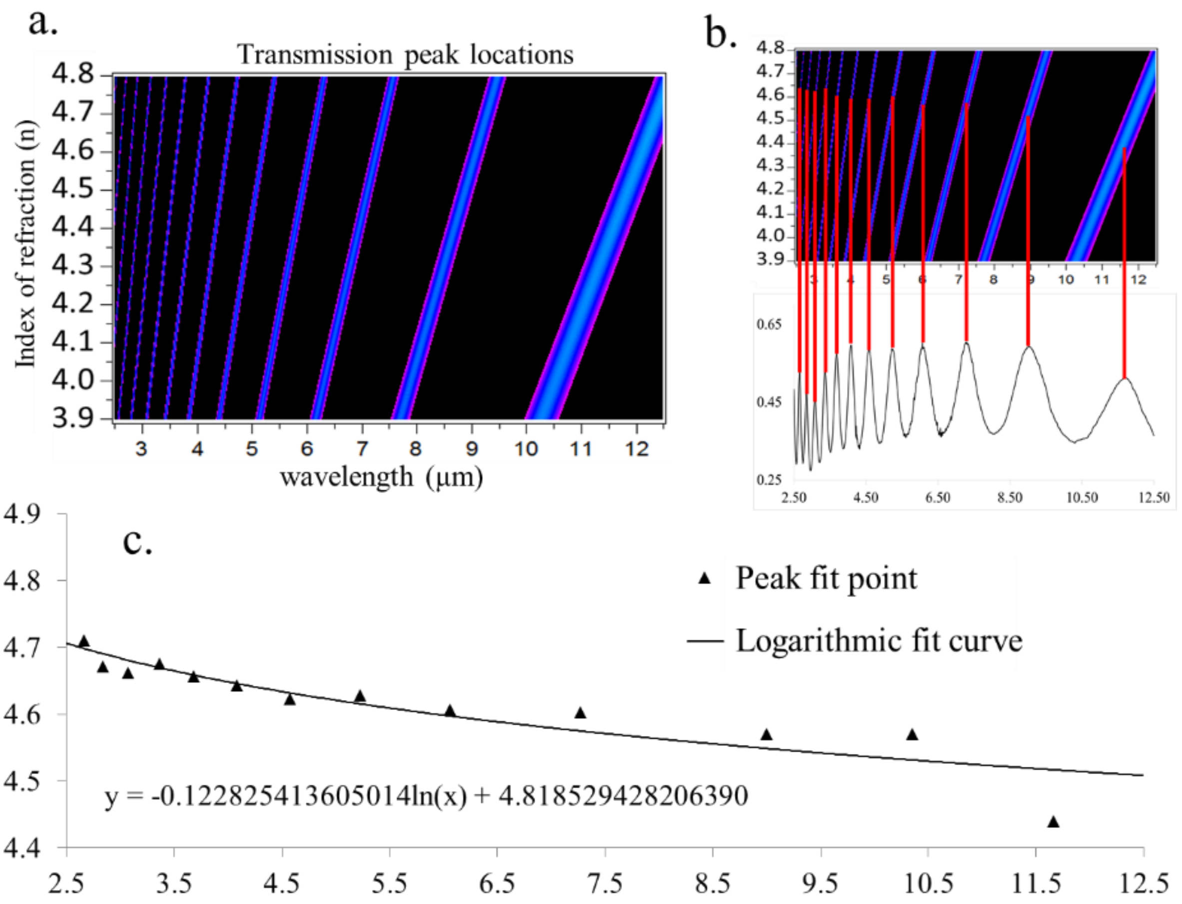

Figure 4.7 - Index matching measured to calculated data for 3950 nm film. a) Transmission peak mapping as a function of index of refraction. b) Example of matching transmission peaks to corresponding indices of refraction. c) Plot of peak locations and logarithmic curve fit.

4.3 850 nm & 2200 nm sputtered device experiment and results

Two additional devices are fabricated to investigate the anomalous refractive index results. The first is a thin film sputtered using the Lab18 recipe “Lee HfO2 Gun 1” which has been conFigured for germanium sputtering. A 2-mm-thick, 25-mm diameter ZnS wafer along with a 260 μm thick 50 mm diameter silicon wafer are cleaned with acetone, IPA, DI water, and then plasma cleaned with O_2 and Ar as described in Chapter 2. The pieces are placed in the Lab18 chamber and the sputter process is run for 8675 seconds. The samples are then coated with the Si passivation layer using the recipe “Daniel Si deposition full auto” with a 300 s pre-

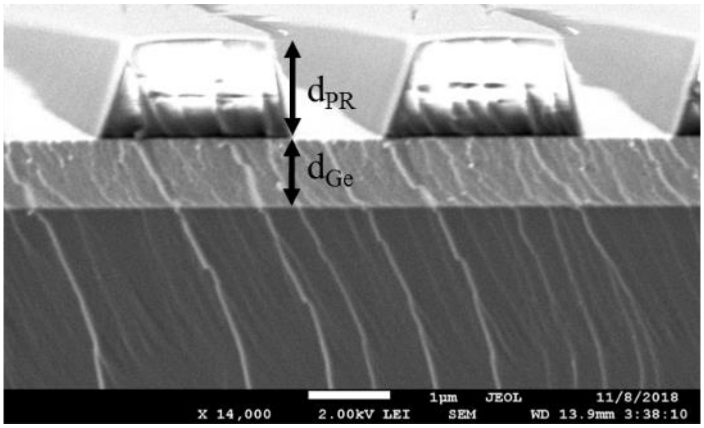

Figure 4.8 – 850 nm film thickness measurement. d_{PR} = 1220 nm, d_{Ge} = 850 nm.

sputter and 480 s sputter time. The final thickness of the sputtered layer is again measured by cleaving a Si dummy wafer after patterning a PR grating and then viewing the cross-section under SEM as shown in Figure 4.8. Results of these measurements show the layer thickness deposited to be approximately 850 nm.

Before patterning the ZnS device, a transmission measurement is taken of the clean germanium layer. Due to the thinness of the sputtered layer only two transmission peaks are present. These peaks are again matched to an index of refraction mapping, the results of which are shown in Figure 4.9. In this case, the matching indicates an index of refraction for the

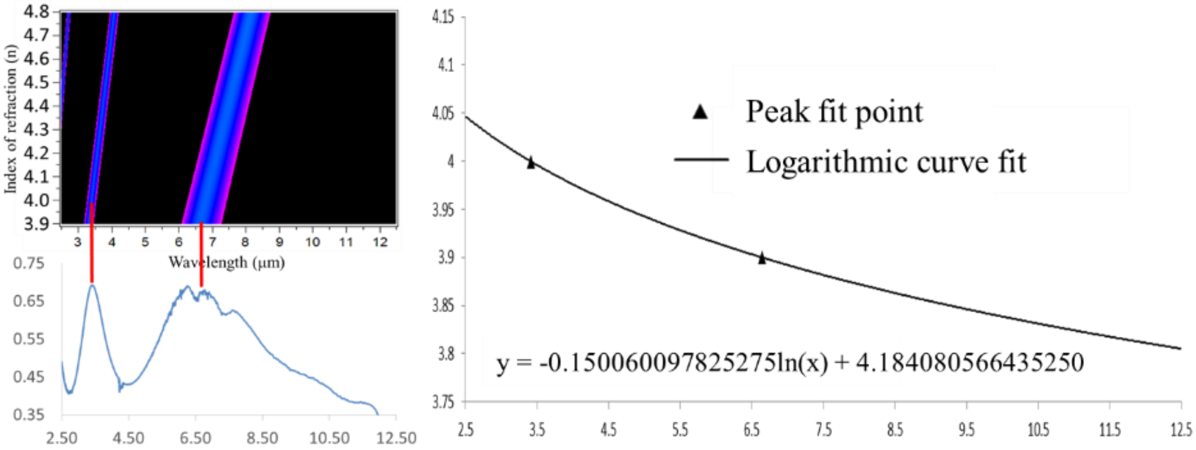

Figure 4.9 – Refractive index curve fitting for 850 nm film. Two transmission peaks are present and used to fit a logarithmic index curve.

germanium layer that is significantly lower than would be expected for crystalline material.

Verification of the index measurement is achieved by patterning the device with a resonant grating structure. Figure 4.10 shows the measurement results for the 850 nm device. The spectrum is calculated for unpolarized input across the entire MWIR and LWIR range from 2.5 to 12.5 μm using the index of refraction calculated from the thin film transmission measurements. It is overlaid on unpolarized transmission measurements taken with the FTIR. The inset shows a cross section of the Si dummy device prepared in parallel. Device dimensions are d_g = 500 nm, d_h = 350 nm, Λ = 3.67 μm, f = 0.61. The spectral matching is undeniable, and indicates that in the case of an 850 nm sputtered film, the effective index of refraction of the

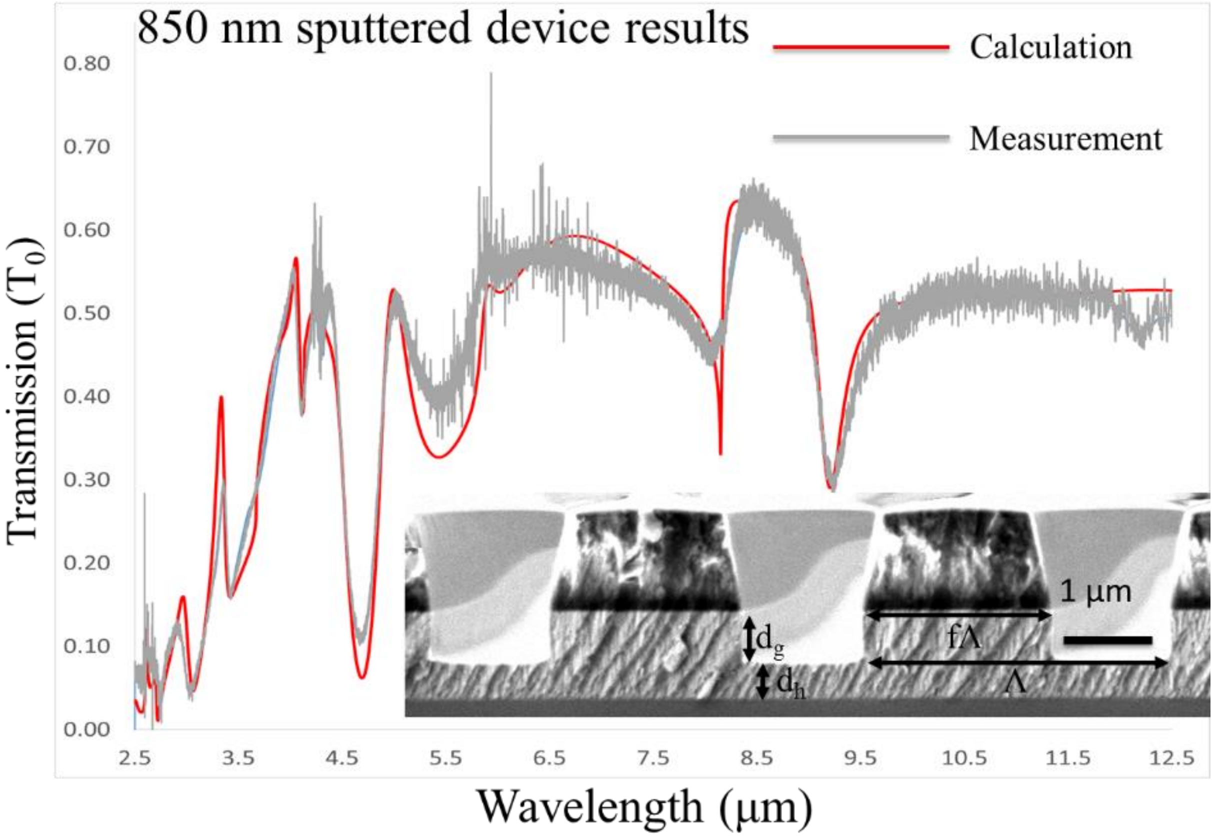

Figure 4.10 - 850 nm device unpolarized calculation and measurement results. Inset shows SEM cross section of fabricated dummy device on Si. d_g = 500 nm, d_h = 350 nm, Λ = 3.67 μm, f = 0.61. Spectrum is calculated using logarithmically fit index of refraction from film transmission measurement.

material layer is significantly lower than the nominal value.

As the index of refraction results for the 850 nm and 3950 nm films appeared to vary greatly in magnitude, a third device was fabricated with an intermediate thickness to investigate whether some sort of gradient effect was occurring. The device is designed around a 2250 nm thick film that is designed to have four specific resonant points in the LWIR region. These points will act as sensitivity markers and will shift with a varying index of refraction. Figure 4.11 shows the design for the 2250 nm device, the TE and TM spectra calculated using intrinsic crystalline values for the germanium index of refraction, and index maps for the TE and TM spectra showing the predicted shift of the resonant points as a function of the index of refraction.

As before, a 1.95-mm-thick, 25-mm-diameter ZnS-MS wafer is cleaned and prepared for a 2250 nm thick layer of sputtered Ge. After deposition, the sample is coated with the 10 nm Si

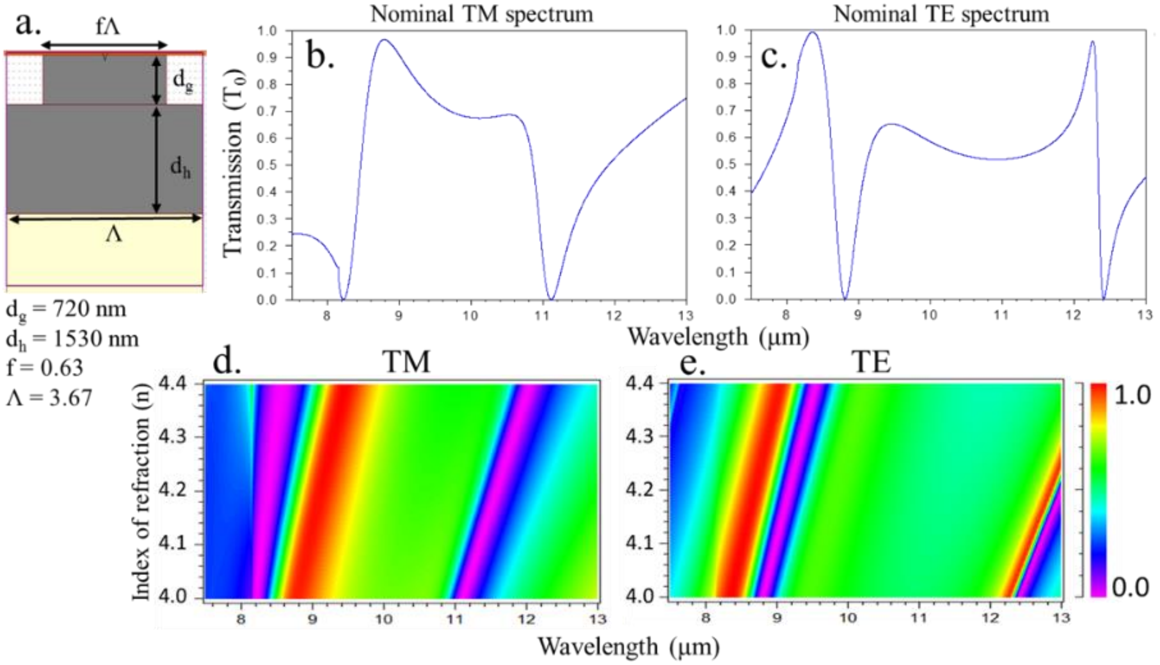

Figure 4.11 - 2250 nm device design and spectral maps. a) ZCG device dimensions. b) TM spectrum calculated with intrinsic values for n. c) TE spectrum. d) TM T_0 resonance sensitivity as a function of n. e) TE resonance map.

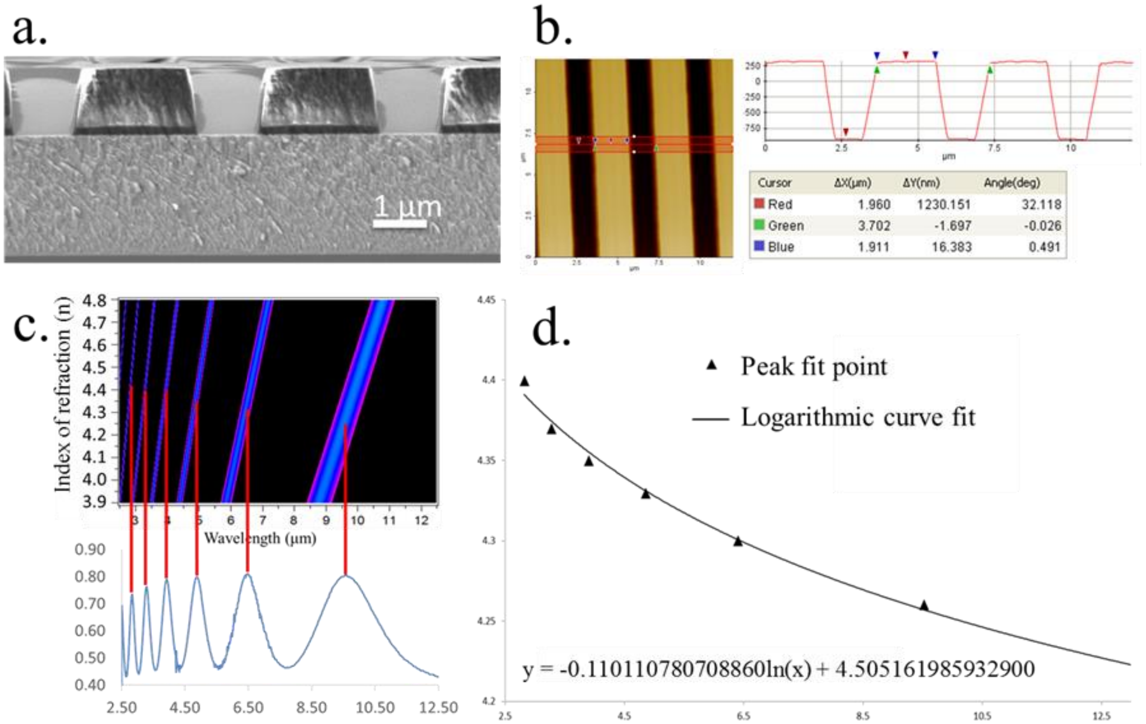

Cursor	ΔX(µm)	ΔY(nm)	Angle(deg)
🟥 Red	1.960	1230.151	32.118
🟩 Green	3.702	-1.697	-0.026
🟦 Blue	1.911	16.383	0.491

Figure 4.12 - 2250 nm Ge film measurements. a) SEM cross-section of Ge film on Si with patterned PR grating. b) AFM measurements of PR grating. c) Transmission peak measurement for Ge on ZnS-MS film and index mapping. d) Graph of fit points and logarithmic curve fit showing increased index and dispersive nature of curve.

passivation layer. Figure 4.12 shows a prepared sample with patterned photoresist grating. AFM measurements are used to verify the grating height and film thickness, and thin film transmission measurements are taken for the unpatterned Ge on ZnS film. In this case we see that the data once again indicates an increase in the index of refraction, although not as much as was seen with the 3950 nm thick film. The data at this point seems to indicate that there is indeed a gradient of indices of refraction observed dependent upon the thickness of the germanium sputtered layer.

To confirm the 2250 nm film Fabry-Perot measurements, the film is patterned according to the design in Fig. 4.11. A cross-section of the fabricated dummy device along with measured TE and TM spectrum results for the 7.5 to 12.5 µm range are shown in Figure 4.13. The

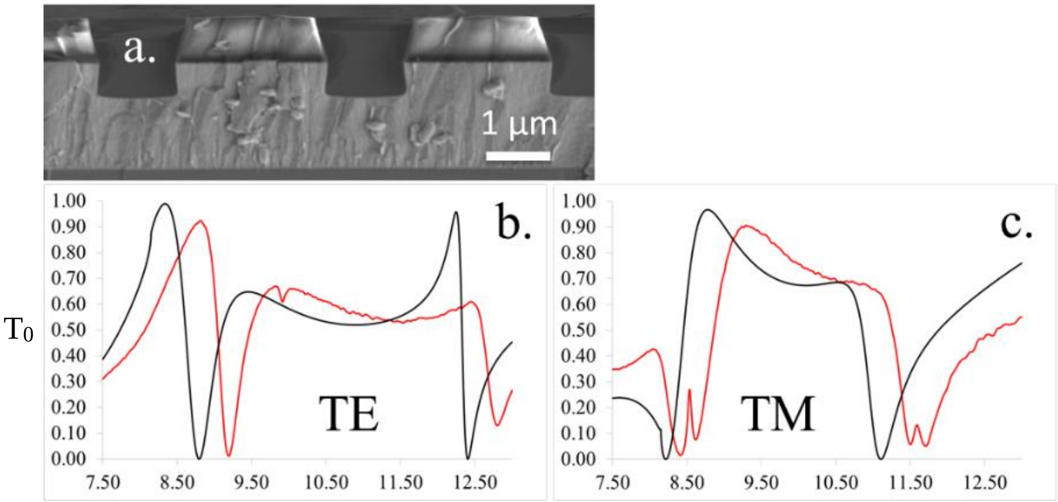

Figure 4.13 - Fabricated 2250 nm device with spectra comparisons. a) SEM cross section of dummy device. b) TE measured spectrum and calculated spectrum using intrinsic crystalline Ge index of refraction value. c) TM measured and calculated spectrum.

measured results are placed alongside calculations using the intrinsic index values for Ge, and we see again the shifted measured T_0 resonant points as appeared with the 3950 nm sample. The TM resonance also displays split resonant peaks likely due to a slight misalignment of the sample stage, but it is clear that the overall envelope of the resonance is red-shifted.

Figure 4.14 shows the results of fitting the resonant points to the calculated index map and displays the logarithmic fit curve. We see the calculated index values again follow a dispersive curve from n = 4.3 at 7.5 μm to n = 4.15 at 13 μm. As with the two previous films studied, these values support the results given by the thin film Fabry-Perot transmission map. The 2250 nm sputtered film has demonstrated an increase in the refractive index, though not as high as the 3950 nm film. Fig. 4.14 c) & d) show the revised spectrum simulations using the logarithmic curve for the index shown in Fig. 4.14 b). The simulated spectra using the higher index of refraction values are now closely aligned with the measured results in a repeat of the results seen for the 3950 nm film.

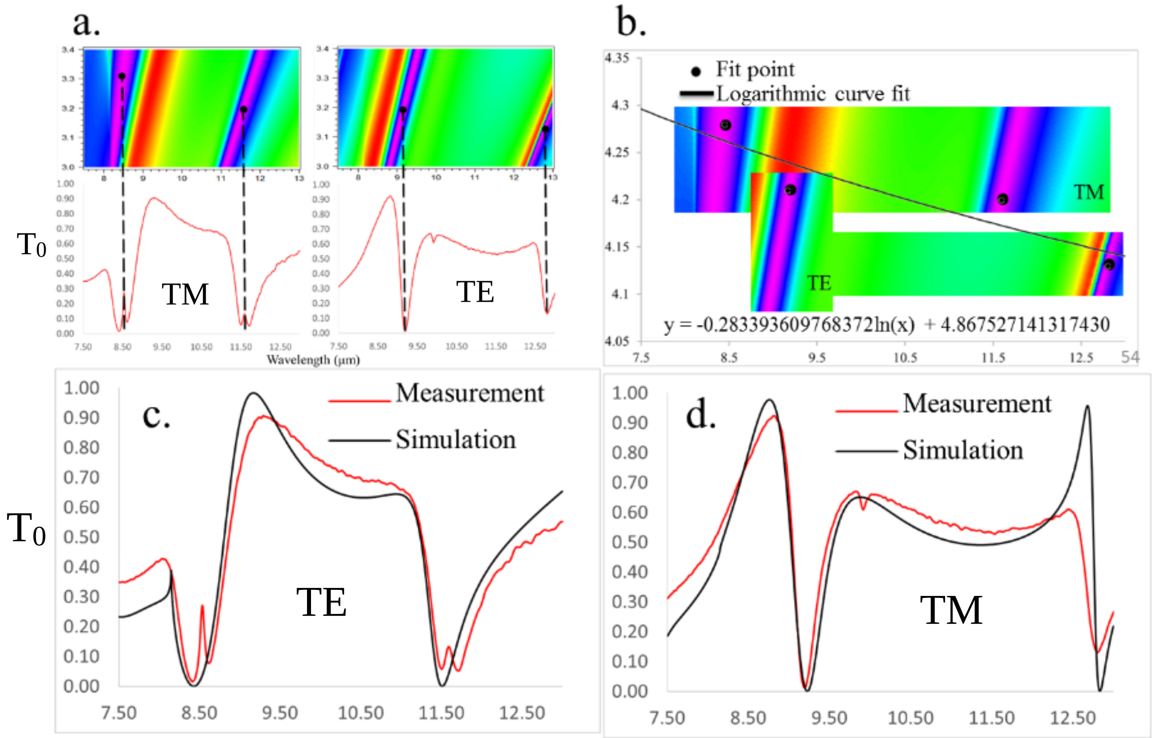

Figure 4.14 - Spectral response fit for 2250 nm device. a) Mapping of the resonant points to the refractive index shift calculations. b) Logarithmic curve fit of the mapped points. c) TM measured and calculated spectrum using fit refractive index values. d) TE measured and calculated spectrum.

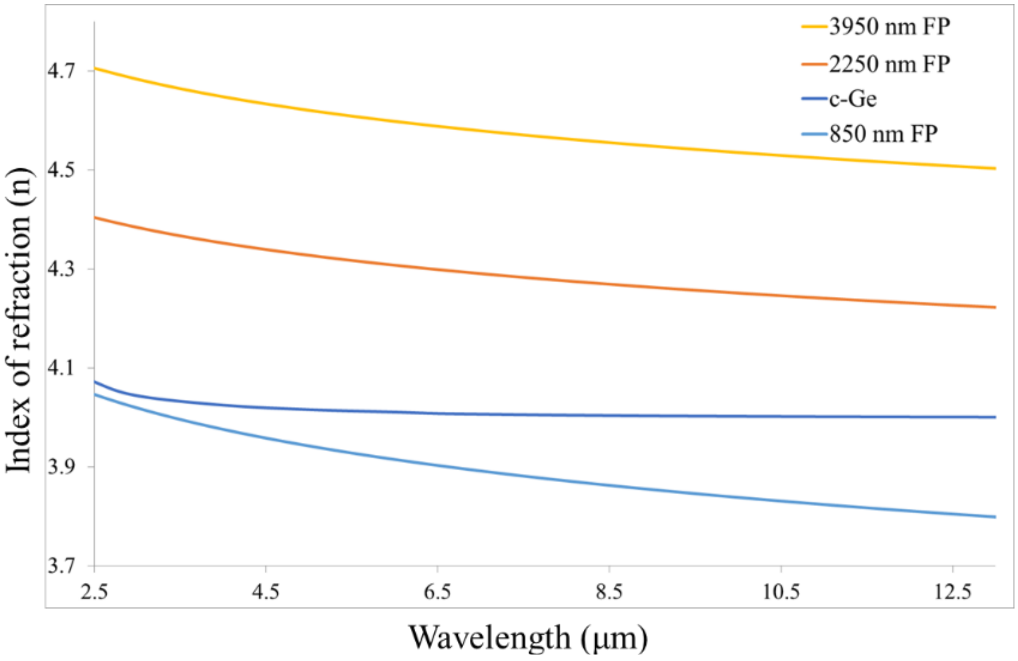

Figure 4.15 - Sputtered films index of refraction summary.

The index of refraction observations are summarized in Figure 4.15. Thin film Fabry-Perot transmission fit results are shown for the MWIR and LWIR for all three samples along with the index of refraction of crystalline germanium for comparison. These results indicate that sputtered films of germanium can demonstrate a range of optical characteristics apparently dependent upon the sputtered film thickness.

4.4 Sputtered germanium film chemical and structural analysis

Further analysis is conducted on the sputtered films in order to gain a deeper understanding of the underlying cause of the observed refractive index anomalies. Energy-dispersive spectroscopy (EDS) is conducted in order to verify the chemical composition of the devices in order to rule out the existence of any chamber contamination that may have contributed to impure film growth. Following this, XRD spectroscopy is used to gain an understanding of the physical morphology of the films.

The EDS measurements are carried out using a 20 kV beam in a Bruker Quantax SEM chamber. Spectral results for the 850 nm, 2250 nm, and 3950 nm films are shown in Figures 4.16, 4.17, and 4.18 respectively. Measurements are performed on areas adjacent to the patterned surface where photoresist completely covered the film during etching and left intact the entire sputtered germanium film along with the silicon passivation layer.

All three samples produce results that are consistent with expectations. For the 2250 nm and 3950 nm films, we see results that are predominantly germanium along with zinc, silicon, oxygen, and trace amounts of argon that were trapped during the sputtering process. The 850 nm film also produces a sulfur signature that is a result of the thinner film allowing more penetration of the beam and a deeper probing of the underlying substrate. All three films also produce a carbon signature, likely the result of residual photoresist, organic cleaning solvents, or other surface contamination. The key result is that no unexpected contamination exists that may have been contributing to the resonant shift of the devices.

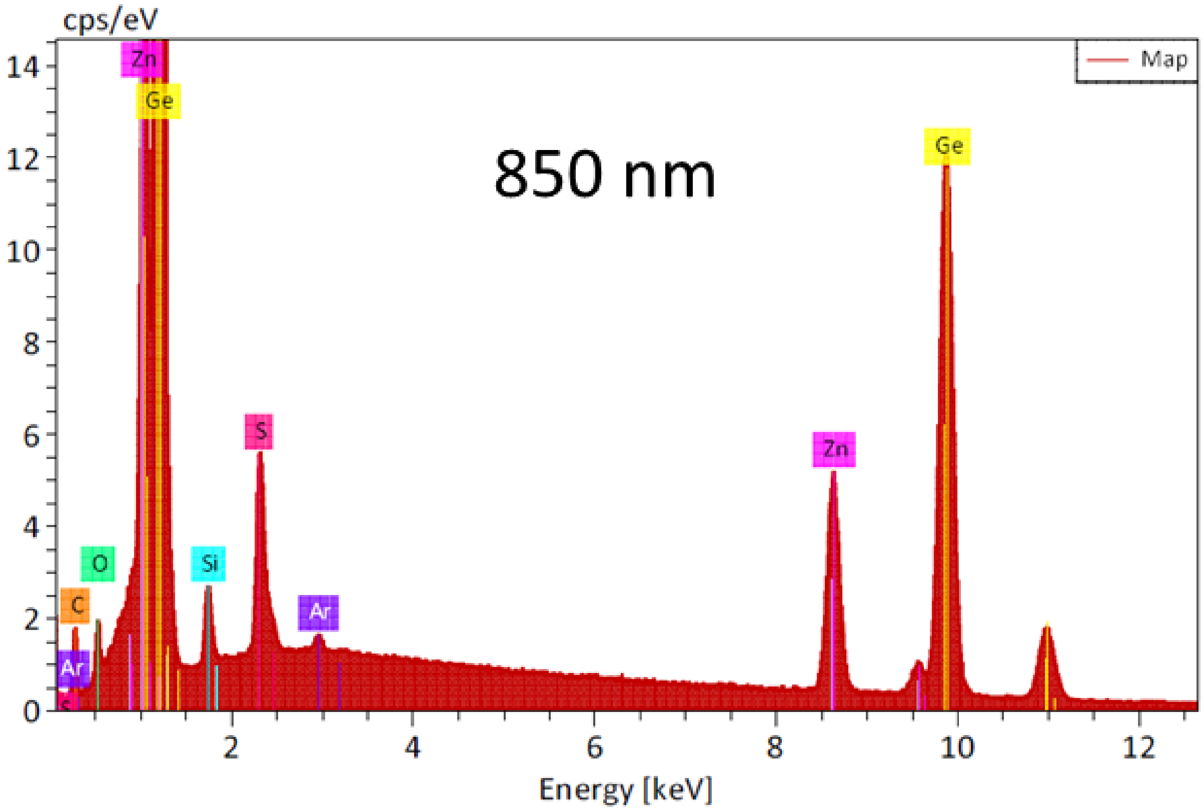

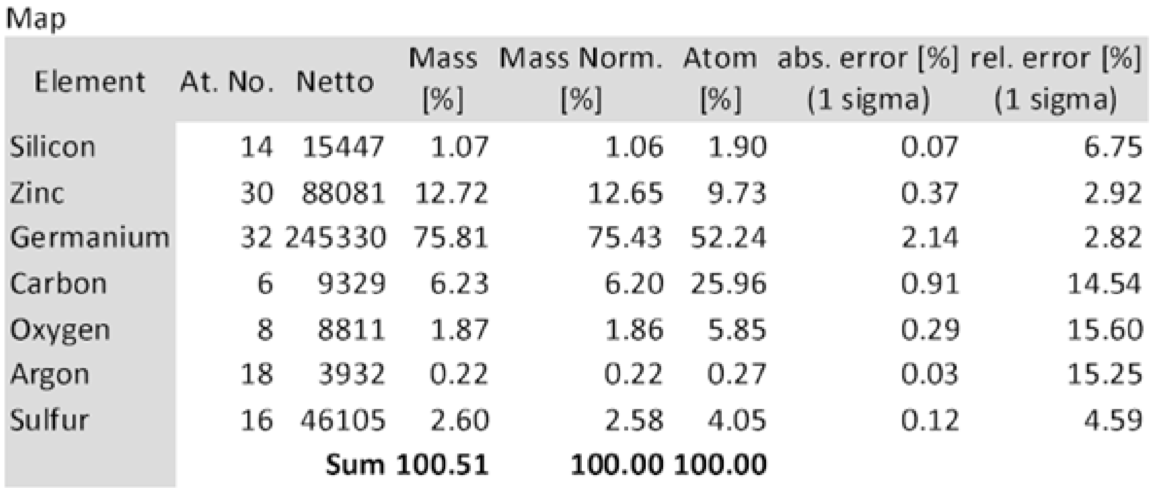

Map

Element	At. No.	Netto	Mass [%]	Mass Norm. [%]	Atom [%]	abs. error [%] (1 sigma)	rel. error [%] (1 sigma)
Silicon	14	15447	1.07	1.06	1.90	0.07	6.75
Zinc	30	88081	12.72	12.65	9.73	0.37	2.92
Germanium	32	245330	75.81	75.43	52.24	2.14	2.82
Carbon	6	9329	6.23	6.20	25.96	0.91	14.54
Oxygen	8	8811	1.87	1.86	5.85	0.29	15.60
Argon	18	3932	0.22	0.22	0.27	0.03	15.25
Sulfur	16	46105	2.60	2.58	4.05	0.12	4.59
		Sum	**100.51**	**100.00**	**100.00**		

Figure 4.16 - 850 nm film EDS results.

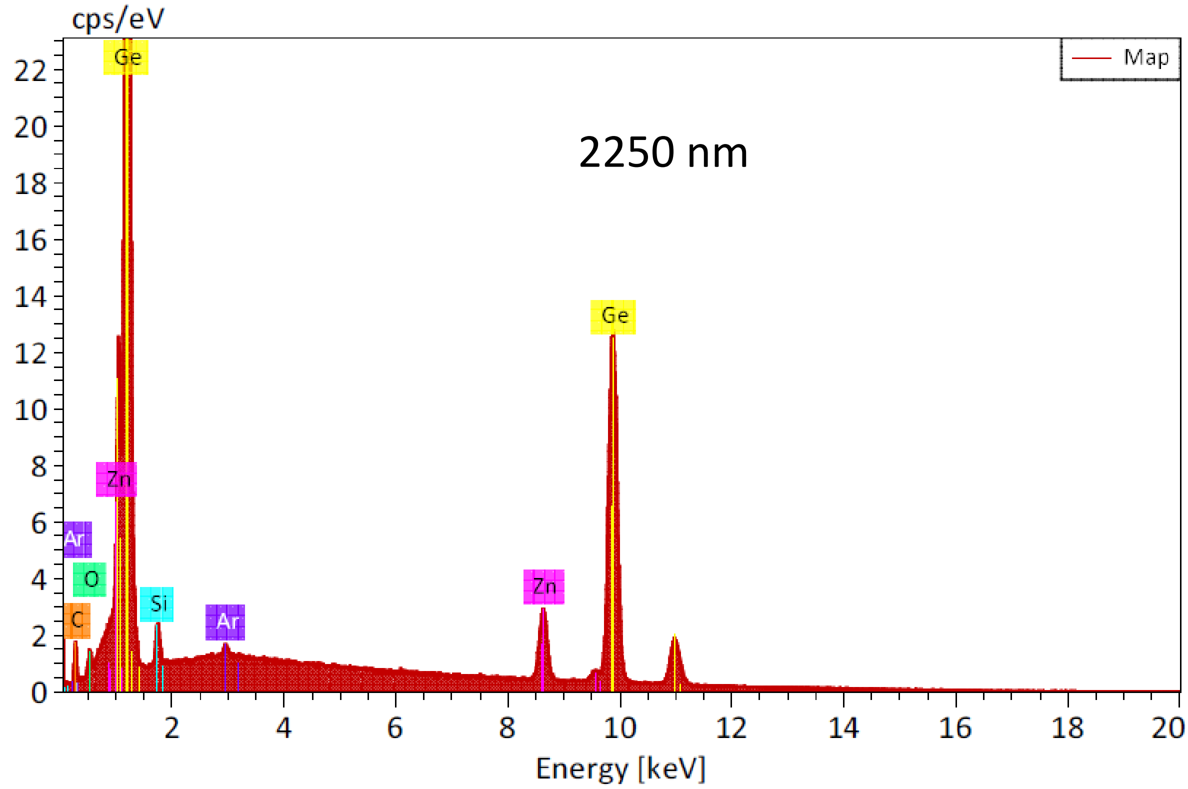

Map

Element	At. No.	Netto	Mass [%]	Mass Norm. [%]	Atom [%]	abs. error [%] (1 sigma)	rel. error [%] (1 sigma)
Silicon	14	9832	1.12	1.13	2.09	0.08	6.74
Zinc	30	31810	6.24	6.33	5.03	0.20	3.17
Germanium	32	183109	83.32	84.53	60.48	2.35	2.82
Carbon	6	6510	6.31	6.40	27.67	0.97	15.35
Oxygen	8	4271	1.33	1.35	4.39	0.24	18.00
Argon	18	3040	0.25	0.25	0.33	0.03	13.99
		Sum	**98.57**	**100.00**	**100.00**		

Figure 4.17 - 2250 nm film EDS results.

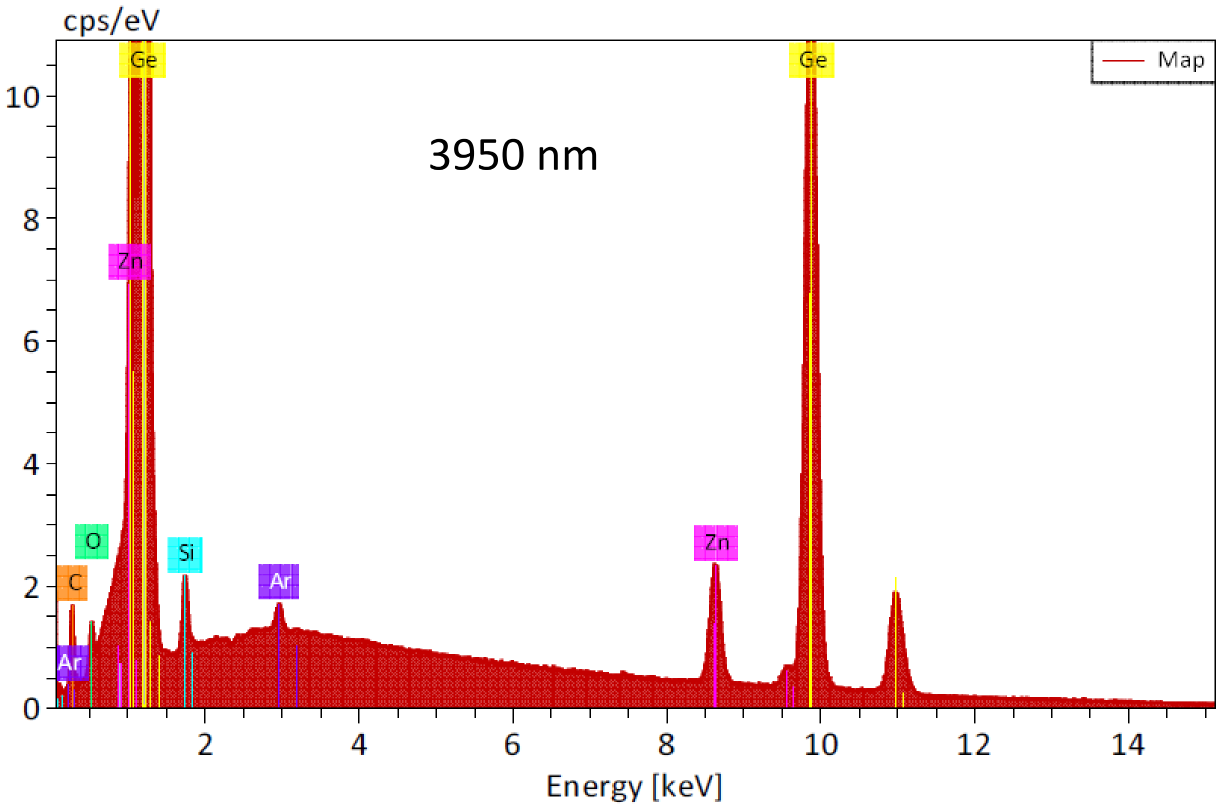

Map

Element	At. No.	Netto	Mass [%]	Mass Norm. [%]	Atom [%]	abs. error [%] (1 sigma)	rel. error [%] (1 sigma)
Zinc	30	75828	4.83	4.91	4.00	0.16	3.24
Silicon	14	20641	0.68	0.69	1.31	0.05	8.07
Oxygen	8	10615	1.10	1.12	3.74	0.18	16.15
Germanium	32	564318	85.55	86.97	63.84	2.41	2.81
Carbon	6	18316	5.93	6.03	26.74	0.79	13.38
Argon	18	10267	0.27	0.28	0.37	0.03	12.60
		Sum	**98.36**	**100.00**	**100.00**		

Figure 4.18 - 3950 nm film EDS results.

Next, XRD analysis is performed on the samples to determine their morphological composition. As the measurement is taken on patterned devices, the grating lines are oriented in parallel with the incoming x-ray beam in order to ensure than any pattern induced diffracted energy is sent away from the detector. The scan is made from 10 to 60 degrees at a scan rate of 0.02^0/s. Initial results are shown in Figure 4.19. Detector intensity is in arbitrary units reported by the measuring equipment, and results are displayed using the standard 2θ convention. In this image, we see that the most striking markers are the ones consistent with cubic zinc sulfide [77]. This is expected as the substrate used is highly crystalline in nature and the film is presumed to be predominantly amorphous.

Figure 4.20 shows a detailed view in the region from 20 – 30 degrees. In this area, there are several smaller peaks apparent corresponding to cubic silicon, cubic germanium, and germanium dioxide. Most important is the marker corresponding to the cubic-Ge <111> plane which indicates that this would be a region containing information about the film structure.

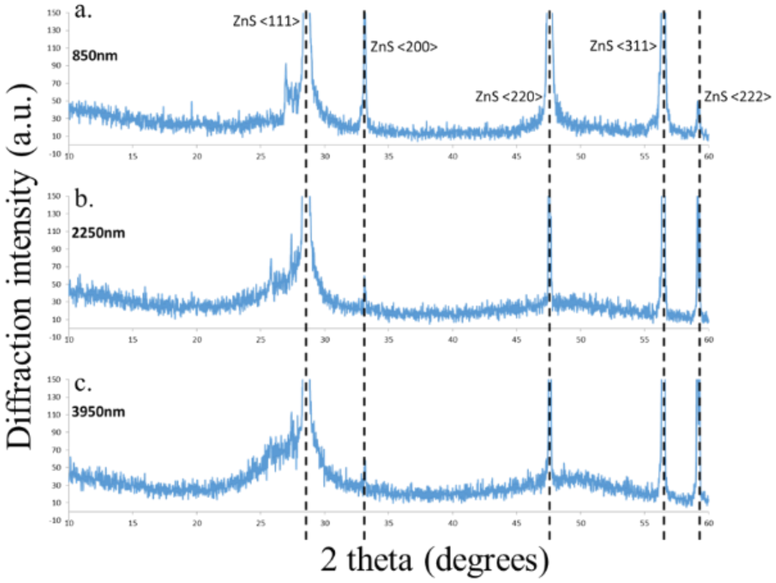

Figure 4.19 - Initial XRD results for 850 nm, 2250 nm, and 3950 nm device showing cubic ZnS diffraction responses.

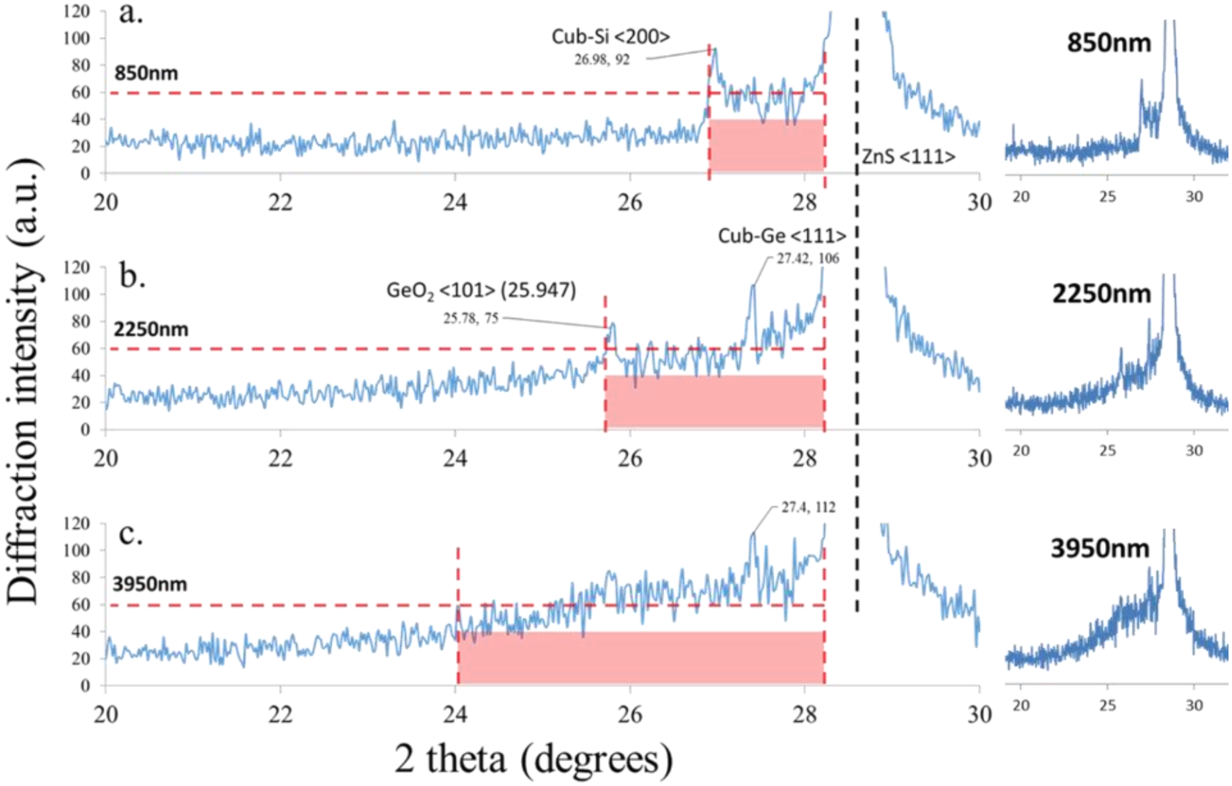

Figure 4.20 - Detailed XRD view showing spectral broadening. a) 850 nm device spectrum, b) 2250 nm device spectrum, c) 3950 nm device spectrum.

When comparing the spectral patterns for the 850 nm, 2250 nm, and 3950 nm films, there is an apparent broadening of the response when progressing from thin to thicker films. Lines have been drawn on the Figure showing the area where the peak intensity measured by the instrument reaches an arbitrary value of 60. For the 850 nm device, this is roughly one degree in area. For the 2250 nm device, the region increases to over two degrees, and for the 3950 nm device is it over four degrees. Slightly more zoomed out views to the right of each graph give another visual representation of the broadening.

A broadened XRD response is generally indicative of an amorphous substance [78] [79], and the data in this case would seem to indicate that the more thickly grown film gains a more amorphous characteristic. This corroborates well with the previous literature describing the nature of sputtered germanium films and the films' optical characteristics [73] [74]. In this case, it would begin to offer an explanation in that the thicker films take on a denser, more amorphous structure that results in an increase in their index of refraction.

4.5 Confirmation of results

Two additional devices are fabricated in order to confirm the repeatability of the optical characteristics observed in the sputtered films. A second 850 nm device is designed with a TE resonant point in the LWIR that will serve as a measurement dial for the film's index of refraction. A second 2200 nm device is designed similar to the first with multiple TM and TE resonant markers that will be used to determine the refractive index of the film. Figure 4.21 displays the device designs along with their resonant spectra calculated using the intrinsic

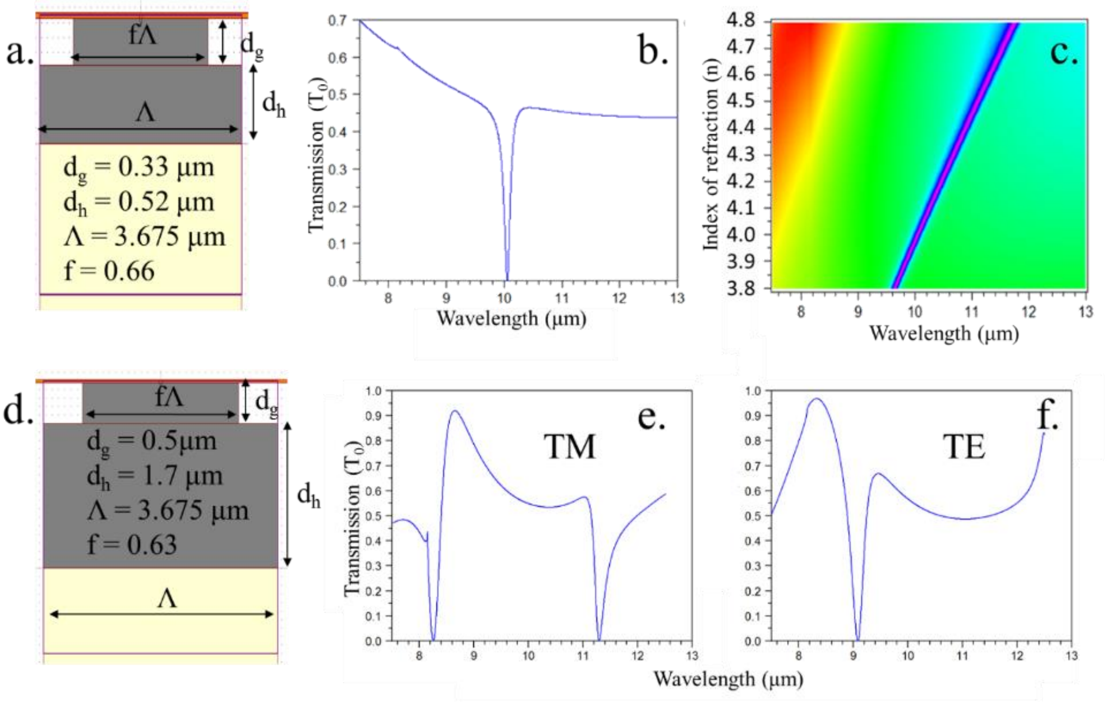

Figure 4.21 - Device designs for index of refraction shift confirmation. a) design for device fabricated on an 850 nm film. b) TE response of 850 nm device using intrinsic refractive index value. c) spectral shift of resonance as a function of n. d) 2200 nm device design. e) TM spectrum of 2200 nm device. f) TE spectrum of 2200 nm device.

crystalline value of index of refraction for germanium. Fig. 4.21 c) shows the resonant shift that will be expected with a shifting index of refraction; the shift is not shown for the 2200 nm device, but the TM and TE peaks will follow a similar trend as shown in Fig. 4.11.

The devices are fabricated using the same parameters as all previous samples. Additionally in this case, the temperature of the substrate carrier is monitored during the 2200 nm deposition to look for any possible temperature related effects. It was found that the temperature remained near room temperature (23^0 C) throughout the deposition. SEM cross sections of the fabricated devices along with their resulting measurements are displayed in Figure 4.22.

Figures 4.22 a) & b) show the results for the 850 nm film. In Fig. 4.22 b), the measured results shown in red are overlaid with a calculated TE spectrum in black using a static index of refraction n_{eff} = 3.84 resulting in a strong spectral location match. This value for the index is lower than the intrinsic value for crystalline germanium and represents a repeat of the results seen with the previous 850 nm device.

Figure 4.22 c) through f) show the results for the 2200 nm device. Figure 4.22 d) shows the logarithmic curve fitting of point matching to Fabry-Perot thin film transmission measurements of the bare film as was done with the previous devices. This fit refractive index data is used to calculate the TE and TM spectral response for the LWIR which is shown in Fig. 4.22 e) & f). Here again we see a repeat of the previous results where the thicker film demonstrates a correct spectral match only when using index of refraction values that are higher than those of intrinsic crystalline germanium. The results shown in Figure 4.22 confirm the previous measurements demonstrating that these sputtered germanium films have a varying and to an extent controllable refractive index that varies significantly from intrinsic values.

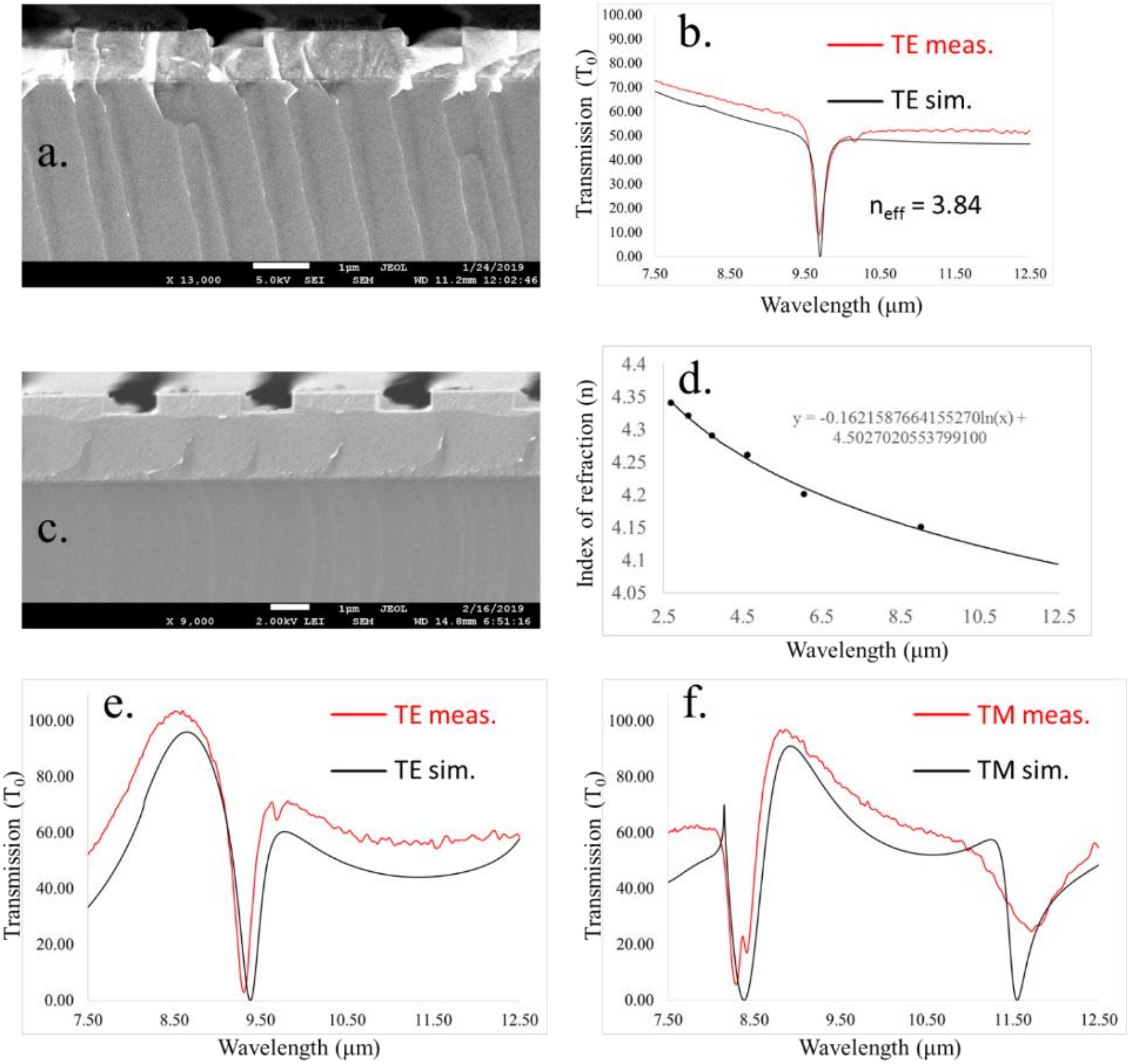

Figure 4.22 - Confirmation device results. a) SEM cross section of 850 nm device. b) Measured and calculated spectrum using static index of refraction $n_{eff} = 3.84$. c) SEM cross section of 2200 nm device. d) Logarithmic curve fit of refractive index from measured FP transmission data. e) TE spectrum calculated using curve fit data. f) TM spectrum calculated using curve fit data.

4.6 Conclusion

In this chapter, results have been presented that demonstrate the variability of optical characteristics of sputtered germanium films for the MWIR and LWIR spectral ranges. It has been shown that the refractive index of these films varies superficially as a function of the film thickness, but that the deeper explanation likely lies in the amorphousness and corresponding density of the sputtered films. A possible reason for the transition from low to high-index films is that lattice mismatches between Ge and ZnS cause nanoscale voids and island growth during the initial deposition. This would lead to a less dense material and a correspondingly reduced refractive index. As the deposition progresses, the film would homogenize into a more dense form as reported in literature. The overall effective medium index of the film would then produce the observed increase in value. Additional studies into the behavior of these films would likely need to include high resolution scans of thin initial film depositions to search for void formation as well as investigations into differing sputtering techniques such as ion assisted deposition which could be used to create high density films independent of the film thickness.

EDS measurements have shown that the films are compositionally pure and free from contaminating elements that could possibly contribute to the fluctuating refractive index measurements, and XRD results indicate a trend of increasing amorphousness as the film thickness increases which corresponds to the increase in index of refraction. Confidence in the refractive index measurements is had through using two-part measurements consisting of Fabry-Perot transmission peak matching and matching of GMR resonant markers in devices fabricated in the films. Finally, the results are verified through the fabrication of a second, repeat set of devices using the same process parameters that then in turn demonstrate the same spectral responses.

These results are significant in that generally speaking, materials with high refractive indices represent desirable characteristics for the fabrication of high quality factor or wideband response devices. The ability to achieve amplified refractive index values using standard and easily fabricated materials would represent a significant boon for the field and lead a range of potential high-precision designs.

Chapter 5 Gold nanocup plasmonic cavity resonances

5.1 Introduction

Since the 1980s, surface plasmon resonance (SPR) has been used to detect refractive index changes caused by the adsorption of molecules on a metallic surface [80] [81], and the idea itself of exciting a surface wave on a metallic surface has been around since the 1950s [82]. Solving Maxwell's equations governing the propagation of a surface plasmon reveals that the surface modes will have a higher momentum than the free space wave. Coupling to a surface plasmon therefore requires some sort of momentum boosting of the incoming wave which was first achieved through prism coupling [83] [84]. Other means have since been found to effectively couple to surface plasmons, including point source scattering [85] and diffractive coupling [86].

When coupling to a surface plasmon, the polarization of the incoming wave must also be considered. Only p-polarized waves with the electric field directed into the metallic surface are able to drive the oscillations in the electron cloud that comprise a surface plasmon wave [87]. A conceptual way of understanding this is that an s-polarized electric field is shorted out as it moves parallel to a metallic surface. Mathematically, this is derived from the tangential boundary conditions for a conducting medium. A practical application of this is that when investigating potential surface plasmon resonances in device simulations, one can often distinguish plasmonic resonances by the polarization state in which they occur.

In this chapter, the resonant characteristics of a two-dimensional array of gold nanocups is analyzed to determine the origin of its resonant response. The cavity-like nature of the nanocups is explored and the resonant response is compared to literature describing the transmission of light through thick metallic films perforated with periodic subwavelength hole arrays. Lastly, simulated results are compared to device measurements to verify the accuracy of the theoretical models. The results in this chapter have recently been published in [88].

5.2 Nanocup fabrication and modeling

A detailed description of the fabrication of the nanocups is given in published literature [89] [90] and will only briefly be described here. Fabrication begins with the creation of a two-dimensional array of photoresist posts by exposing a photoresist-coated silicon wafer using interference UV lithography, rotating the wafer by 90^0, and then exposing it a second time to create a cross-hatched region of exposure that upon development leaves behind an array of photoresist islands. The wafer is then heated sufficiently to reflow the photoresist which forms into hemispherical domes due to surface tension. After reflowing, a 150 nm thick layer of gold is sputtered on top of the wafer. A 1x3" glass microscope slide is then glued to the gold film using epoxy adhesive. After curing, the film is peeled away from the silicon wafer and residual photoresist is removed using O_2 plasma ashing.

AFM and SEM images of a fabricated device are shown in Figure 5.1 that demonstrate the uniformity achieved in the nanocup array. Figure 5.1 a) also shows AFM measurements taken of the cup dimensions. The cups are characterized by three dimensions, the cup diameter, d, the cup depth, s, and the period of the array, Λ. The dimensions as shown in Fig. 5.1 a) are d = 320 nm, s = 197 nm, and Λ = 526 nm.

Two models are examined for computing the spectrum of the device which are shown in Figure 5.2. An exact model is shown in Fig. 5.2 a) where the substrate is topped by a layer of epoxy roughly 300 nm thick which is then topped by the array of gold nanocups. The sputtered layer of gold is 150 nm thick and as such should be optically opaque. With this in mind, a second model is considered in Fig. 5.2 c) where the thickness of the gold layer is considered

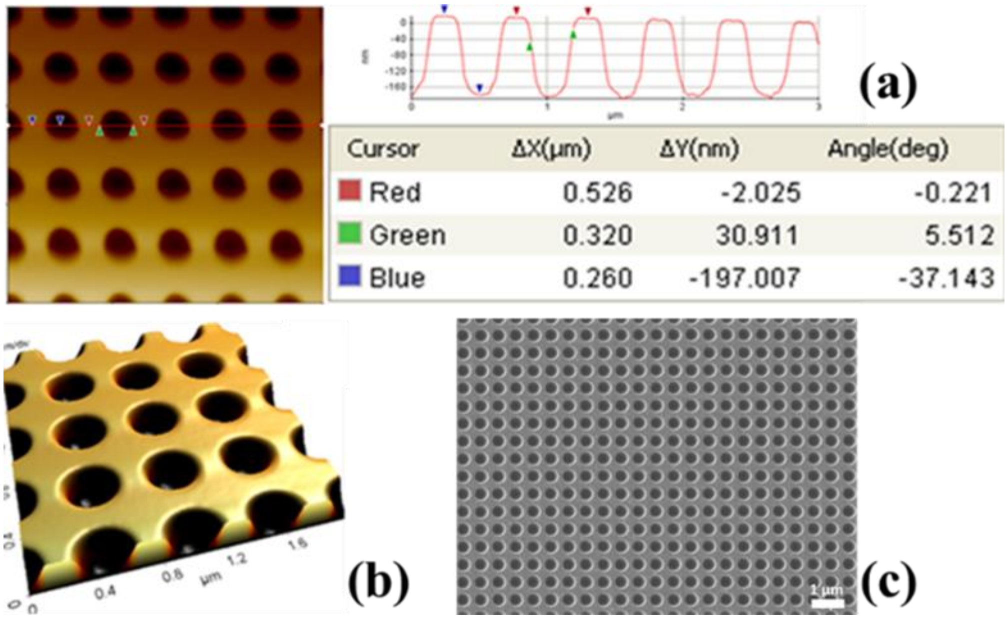

Cursor	ΔX(µm)	ΔY(nm)	Angle(deg)
🟥 Red	0.526	-2.025	-0.221
🟩 Green	0.320	30.911	5.512
🟦 Blue	0.260	-197.007	-37.143

Figure 5.1 – Nanocup AFM and SEM measurements. a) AFM line scan of the array. b) a 3D image generated from the AFM scan. c) SEM image demonstrating the uniformity of the array.

infinite in extent. If reasonable, this second model is desirable as it considerably reduces the complexity and associated computation time required for device simulations.

The spectra are computed using RCWA where fundamentally the accuracy of the results reported is a function of the number of harmonics retained in the calculation. For dielectric devices, this value will generally rapidly converge using less than 10 harmonics, but for metallics with high absorption that number will generally be higher. To test the validity of the two models, a convergence study is performed examining the spectrum as a function of the number of harmonics retained in the RCWA calculation and comparing the results. The results of this are shown in Fig. 5.2 b) & c) where it can be seen that after 15 harmonics, both the exact and solid gold model of the device demonstrate similar spectral responses. This validates the supposition that the gold layer is thick enough to be considered optically opaque, and the solid gold model is retained for the remainder of the device analysis.

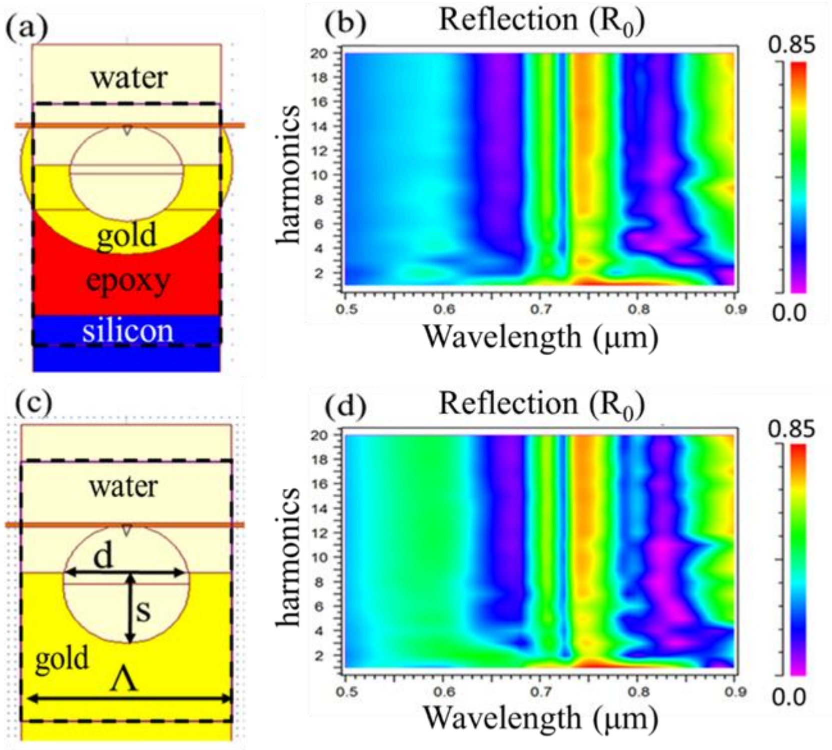

Figure 5.2 - Convergence study comparing the exact nanocup model to a simplified structure. a) The complete model along with b) its reflection spectrum plotted as a function of the number of Fourier harmonics maintained in the RCWA calculation using $n_{epoxy} = 1.5$ and $n_{Si} = 3.77$. c) A simplified bulk Au model along with its simulation results shown in d). Model dimensions used are $\Lambda = 530$ nm, $d = 320$ nm, and $s = 190$ nm.

5.3 Nanocup theoretical analysis

The response of these devices is closely linked to the physics governing transmission of light through metallic films perforated with periodic apertures. The theory governing these devices is reviewed by Garcia-Vidal et al. [91], where the extraordinary transmission phenomenon is explained through the coupling of diffracted surface waves to surface plasmon modes. The plasmon modes are both classical dielectric-metal interface surface plasmon polaritons (SPPs) [87] as well as effective “spoof” plasmons created by the periodic surface modulation [92]. The coupling to these plasmon modes allows the transmission of energy through periodically perforated metallic films several times the skin depth in thickness that would otherwise be optically opaque.

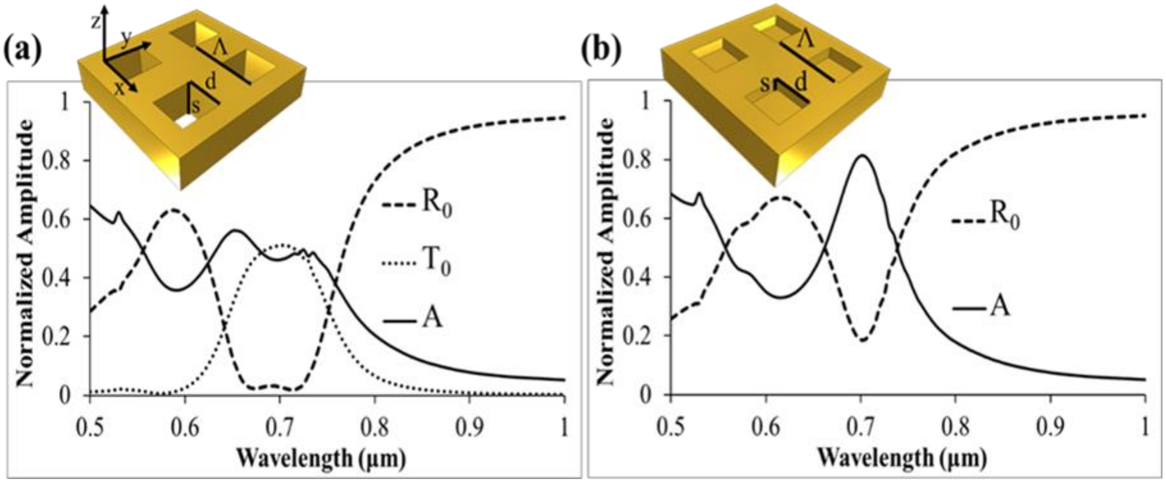

Figure 5.3 - Metallic hole and nanocup array comparison. Shown is zero-order reflection (R_0), transmission (T_0), and absorption (A) for a) a gold film with square hole array, and b) a gold surface with square cup array in air. For both arrays, Λ = 530 nm, d = 273 nm, and s = 400 nm.

Figure 5.3 shows a comparison between the spectrum of a perforated square hole array and an array of square cups. The dimensions are defined as film thickness and cup depth s, side length d, and array period Λ, where for this example s = 400 nm, d = 273 nm, and Λ = 530 nm. Both devices are assumed to be surrounded by air, n = 1. The thickness, s = 400 nm, is chosen as a deliberately large value in which no amount of evanescent field would penetrate through a solid slab. The dimensions of the square opening are also such that if the cutoff wavelength of a square metallic waveguide with side d = 273 nm is calculated using the relation $\omega_c = \frac{\pi c}{d\sqrt{\varepsilon_r \mu_r}}$ where ω_c is the cutoff frequency, the cutoff wavelength, $\lambda_c = \frac{2\pi c}{\omega_c}$ = 546 nm. Nevertheless, we see that in Fig. 5.3 a) there is a strong transmission peak centered at 700 nm. This transmission cannot be explained as simple transmission through the waveguide apertures, as one can calculate the propagation constant of an air filled square waveguide using the expression $k_{wg} = j\sqrt{\frac{\pi^2}{d^3} - k_o^2}$, which when combined with a propagation expression for the electric field traveling in the z direction defined as $\boldsymbol{E} = \hat{y}Ee^{jk_{wg}z}$ results penetration depth $\delta = 1/k_{wg}$ of the waveguide at 700 nm free-space wavelength to be 139 nm.

With a slab nearly three times the penetration depth in thickness, the expected classical amount of transmitted energy would be only 5%, whereas simulations show results an order of magnitude greater in value. The sources of this increased transmission are diffracted surface waves created by the periodic aperture array that are coupled to surface plasmon polaritons (SPPs). It has been shown that the location of the transmission maxima corresponds to SPP values calculated for the perforated film [93]. The surface waves couple to evanescent cavity modes within the subwavelength waveguides which then couple to similar modes on the opposite side of the film and are then diffractively radiated in the inverse of the coupling process.

The connection between the cup and aperture geometries is demonstrated in Fig. 5.3 b) where it is seen that instead of transmission, there is now a large absorption resonance at the 700 nm point. The source of this absorption lies in the cavity modes where now the coupled energy is no longer able to transmit through the film and is instead reflected by the bottom of the cup and forced to travel a second time through the evanescent cavity. The same coupling mechanism that creates the transmission resonance in the film is now coupling into an evanescent resonant cavity mode that manifests in the strong absorption resonance.

The shape of the aperture opening plays a strong role in the resonant response of the device. When dealing with metallic surfaces, the Drude model is a classically used approximation that derives the electrical permittivity by applying a kinetic model of motion to the electron “cloud” within the metal [94]. The resulting expression for the permittivity can be approximated as $\varepsilon_r \approx 1 - \frac{\omega_p^2}{\omega^2}$, where ω_p is the plasma frequency and represents a resonant point in the derivation where the material transitions between behaving as a dielectric to a metal. In their derivation for the effective properties of a periodically modulated metallic surface, Pendry et al. show that a surface perforated with square holes will have an effective plasma frequency given by the expression $\omega_p = \frac{\pi c}{a\sqrt{\varepsilon_h \mu_h}}$ [95], where c is the speed of light, a is the length of the side of the square, and ε_h and μ_h are the relative permittivity and permeability of the material filling the holes. This expression is also exactly the cutoff frequency for a square metallic waveguide with the same properties and is a general result for any arbitrary hole shape. This effective plasma frequency behaves the same as the plasma frequency in a solid metal film and can be used to calculate the position of SPP resonances [91].

This confluence of the effective plasma frequency with the waveguide cutoff frequency demonstrates that there is a strong tie between the plasmonic behavior of a periodically modulated metallic film, the cavity modes defined by the shape of the apertures, and the ultimate resonant response. Figure 5.4 shows a spectral comparison for normally incident light between three nanocup array geometries: a square well with side length 273 nm, a cylindrical well with diameter 320 nm, and a spherical well with diameter 320 nm. All three have a well depth of 190 nm and are assumed to be immersed in water, n = 1.33. The aperture dimensions are chosen so that all three have a waveguide cutoff wavelength of 726 nm. All three devices demonstrate a sharp absorption resonance at the 705 nm Rayleigh wavelength, and then a more broad response near 850 nm related to the cavity interactions.

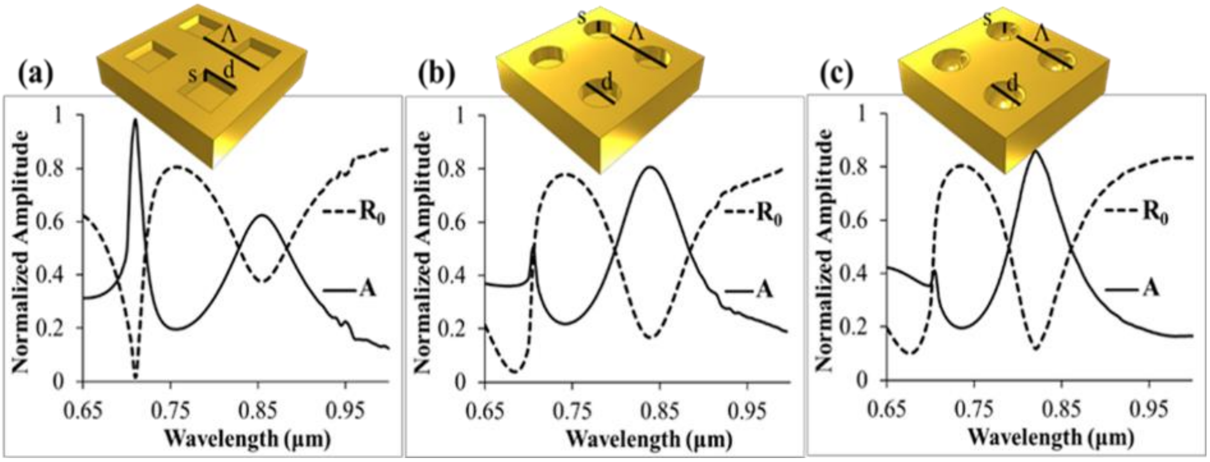

Figure 5.5 - Comparison of nanocup geometry. Reflection and absorption amplitudes are show for **a**) square, **b**) cylindrical, and **c**) hemispherical cup arrays in water. The dimensions are matched such that the cutoff wavelengths of the apertures are the same. Λ = 530 nm and s = 190 nm for all three arrays. For the square array, d = 273 nm, for the cylindrical and spherical array, d = 320 nm.

More insight can be gained into the hybrid SPP-cavity nature of the resonance by examining the device response at off-normal incidence. In Figure 5.5, the spectra are displayed for a square well array with Λ = 530 nm, s = 190 nm, d = 273 nm, and which is immersed in water, n = 1.33. Figure 5.5 a) shows the response at normal incidence, Fig. 5.5 b) shows the response to s-polarized light incident at an angle of 3^0, and Fig. 5.5 c) shows the response for p-

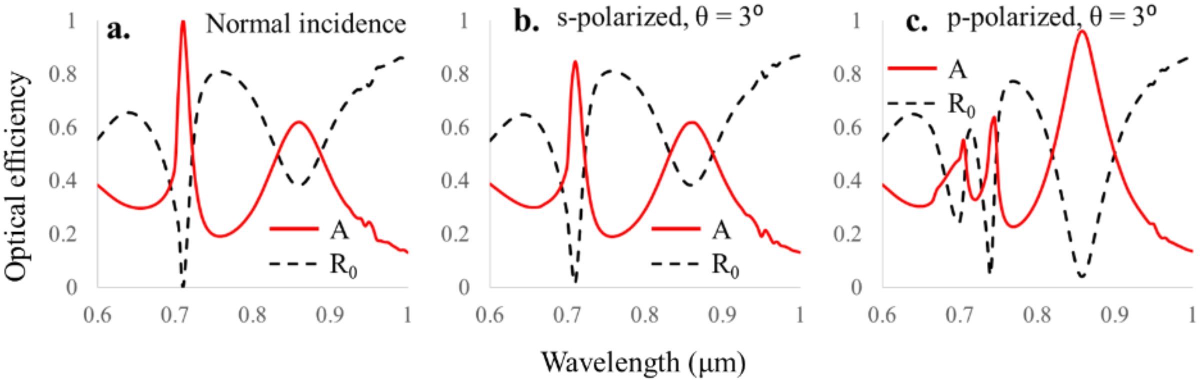

Figure 5.4 - Off-normal incidence resonant response comparison for square cup array. a) Response at normal incidence, b) response to s-polarized light at 3^0 incident angle, c) response to p-polarized light at 3^0 . Array parameters are Λ = 530 nm, d = 273 nm, s = 190 nm, and the array is immersed in water, n = 1.33.

polarized light at 3^0. The normally incident and s-pol responses are virtually identical, but the p-pol response shows two dramatic shifts. The first is the splitting of the response at the Rayleigh point. This is common Rayleigh splitting due to momentum matching of the forward and backward scattered light. More important is the large increase in the absorption resonance at the 850 nm wavelength. SPPs are only able to be excited by p-polarized light, and the sensitivity in the strength of the resonance to the polarization state suggests that it is being driven by increased SPP energy generated by the off-angle incidence.

5.4 Measurement comparisons

A spectral measurement of the fabricated nanocups showing the sensitivity to refractive index shifts is shown in Figure 5.6 a). It is compared to a calculated spherical cup response using Λ = 530 nm, d = 320 nm, and s = 190 nm in Fig. 5.6 b). It is immediately apparent that there is a large discrepancy between the calculated reflection response and the response measured from the device. While the simulations indicate the reflection resonant dip at 820 nm, the measured peak at roughly 720 nm is entirely absent.

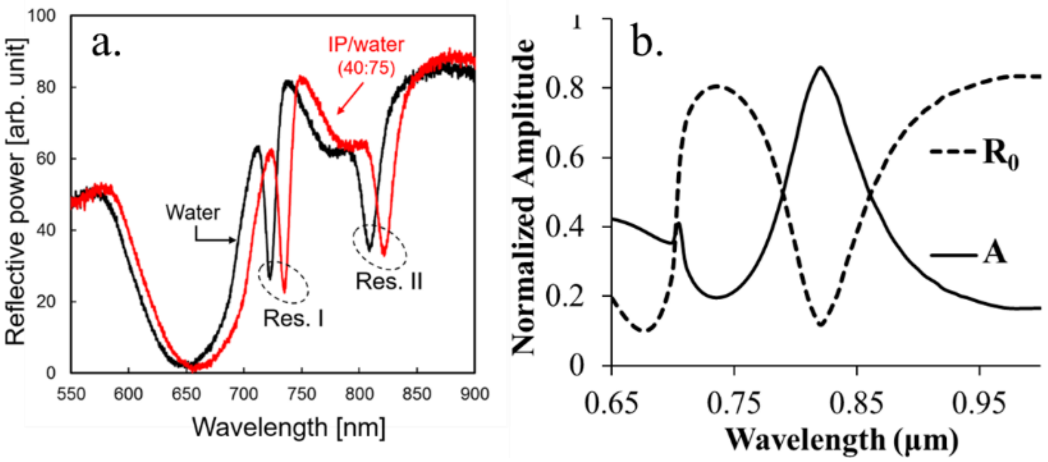

Figure 5.6 - Nanocup measured and calculated spectral comparison. a) Measured response showing two resonant reflection dips. b) calculated response using normally incident uniform plane waves.

The source of the discrepancy is found in the nature of the simulation and by looking back to the results shown for off-angle incidence. The devices are simulated assuming illumination from uniform plane waves, but in reality the beam will take on a curved, Gaussian nature. Misalignments will also affect the resulting spectrum, as shown in Fig. 5.5 c) with a splitting of the Rayleigh resonant point at incident angles off from normal for the square cup geometry.

A Rayleigh spike is present at normal incidence in the spherical geometry as well, but it is masked in the reflection spectrum and is only visible when inspecting the absorption spectrum where a small peak can be seen at 705 nm as shown in Fig. 5.6 b). However, the splitting does become apparent when viewing the spherical device at off normal incidence as shown in Figure 5.7. In Fig. 5.7 a), the calculated reflection response is shown for p-polarized light incident at 1.5^0. Additional resonant features are now apparent, with a sharp reflection dip occurring near 720 nm and another dip appearing near the cavity resonance at 780 nm. This suggests that the

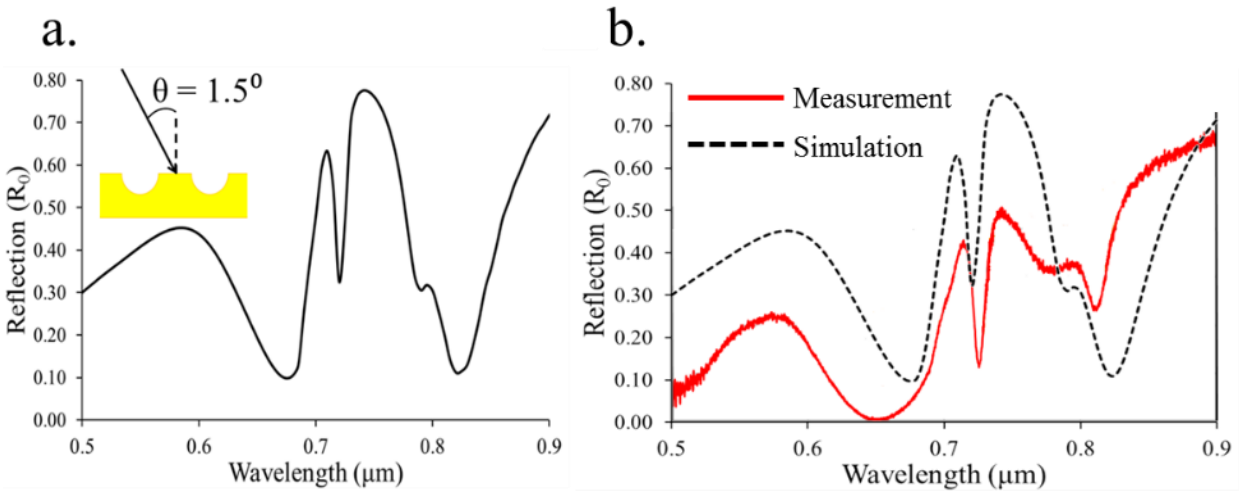

Figure 5.7 - Off-normal incidence and curved wavefront simulations. a) shows a spectrum for a p-polarized planewave with angle of incidence $\theta = 1.5^0$. Inset shows the angle convention used in simulation. b) shows an averaged spectrum from 1^0 to 2^0 and overlays it with measured results.

original measurements may have been slightly out of alignment, or that in order to arrive at a true representation, a more accurate curved wavefront model must be used. Figure 5.7 b) begins to approximate a curved wavefront approach with a calculation made by averaging 11 separate simulations made with incident angles from 1^0 to 2^0. This is overlaid with a measured spectrum in red to demonstrate that similar spectral markers now appear in both results. There is the first reflect dip around 720 nm, a slight shoulder around 780 nm due to the Rayleigh splitting, and the final cavity response near 820 nm.

5.5 Conclusion

This chapter saw a departure from the previous GMR discussions to pursue a theoretical review of diffractively coupled nanocup plasmonic devices. The gold nanocups that were analyzed were shown to have spectral markers related to previous work on extra-ordinary transmission of light through perforated metallic films stemming from the diffractive coupling of SPPs to evanescent waveguide modes. The nanocups in this instance form a parallel branch of study where instead of the formation of waveguide modes, there are evanescent cavity modes formed within the cups that account for the increased absorption observed in the samples. These cavity modes were shown to be sensitive to the SPP generation on the film surface, but also relatively robust to cavity geometries which would be of potential benefit to sensor manufacturing. Lastly it was shown that additional spectral markers observed in the device measurements are likely attributable to alignment errors in the experiment resulting in diffractive splitting of the resonances. However, due to the shared sensitivity of these additional markers, this could also be of benefit as a second point of measurement in a practical plasmonic sensor.

Chapter 6 Future research directions

6.1 ZnS hard mask development

Chapters 2 and 3 presented the blueprints for the reliable fabrication of germanium based MWIR and LWIR resonant devices. But as was pointed out, there still exists some shortcomings to be overcome and room for further development. One area of issue was the significant fill factor losses incurred when deep etching a device that occurred largely due to limitations in the photoresist exposure step. The required thickness of the photoresist combined with the exposure method used and the density of the feature sizes results in a trapezoidal profile in the developed pattern. This non-ideal photoresist mask results in losses in the final etched grating profile. An attempt could be made to adjust the exposure mask dimensions to compensate, but the linewidths being exposed are already very close to the resolution limits of the EVG-620 mask aligner and any attempts to increase the fill factor with the positive photoresist mask may have limited success.

When tight control of device dimensions is required, a hard mask consisting of a highly etch resistant material is often employed. These can be inorganic type materials such as SiO_2, SiN, or TiN, or metallic masks made most commonly using Cr. The hard masks are generally placed on the target substrate using a form of deposition-liftoff, spin-on coating [96], or even membrane transfer [97]. Whatever the method employed, another key consideration is the removal of the mask after etching. For silicon processing, this is often done using an acidic solution that will dissolve the mask while not attacking the underlying substrate, but this can often be a nontrivial matter [98], and in the case of an IR device based on a ceramic substrate such as ZnS or ZnSe, acidic methods would be impossible as the ceramic substrate would be highly attacked.

One method considered to implement a hard mask is to use a deposition-liftoff process that would utilize ZnS as the hard mask. This would offer two potential benefits. One would be the additional etch control gained by using a mask highly resistant to the etch process and sidewall erosion. The second would stem from zinc sulfide's low-index and high IR transparency that could eliminate the necessity of removing it after the etch step. Figure 6.1 shows two ZCG GMR wideband reflector designs. The design shown in Fig. 6.1 a) with its corresponding spectrum in b) is Ge on ZnS based with d_g = 2.2 μm, d_h = 1.8 μm, Λ = μm, and f = 0.66. The design shown in Fig. 6.1 c) is identical except that it also contains a 100 nm layer of

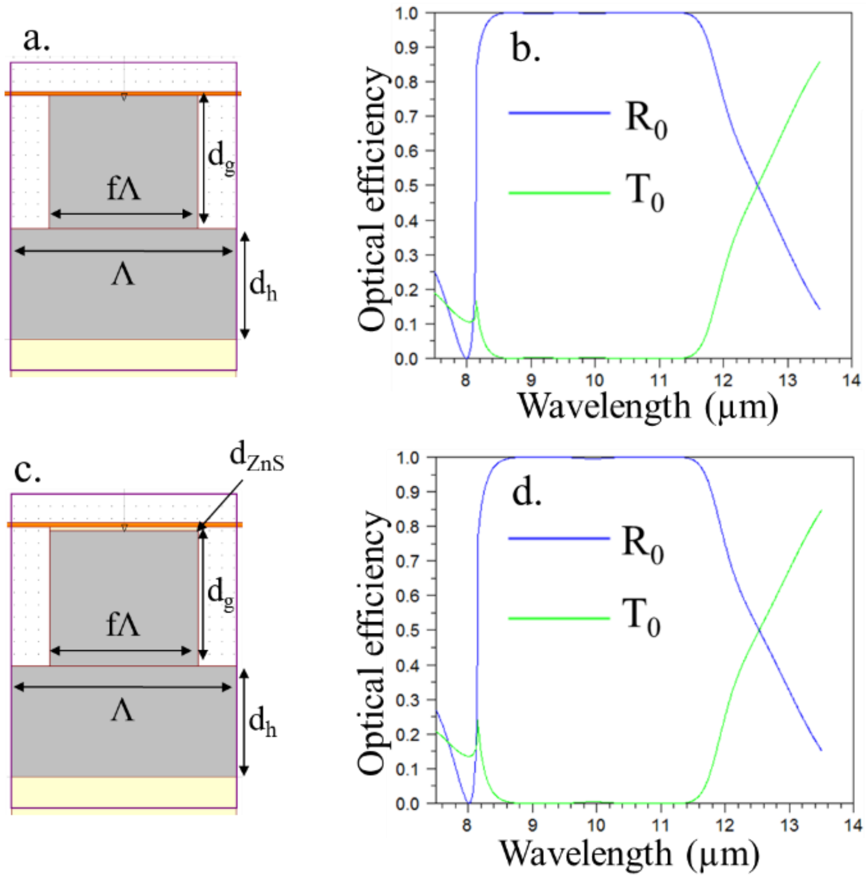

Figure 6.1 – ZnS hard mask device impacts. a) ZCG grating design with d_g = 2.2 μm, d_h = 1.8 μm, Λ = μm, and f = 0.66. b) TM wideband spectrum from device a). c) ZCG grating design with an additional ZnS hardmask layer, d_{ZnS} = 100 nm. d) spectrum for device with ZnS hardmask.

ZnS on top of the grating. As can be seen in Fig. 6.1 d), the spectrum is slightly modified, but the overall wideband nature is largely maintained.

Of greater potential benefit would be the utilization of a ZnS hardmask to produce a two-dimensional design. Fill factor losses in these cases are often more severe due to the increased surface area exposed during the photoresist exposure and etching processes, but by using a mask process as shown in Figure 6.2, it may be possible to create a robust, high fill-factor unpolarized design.

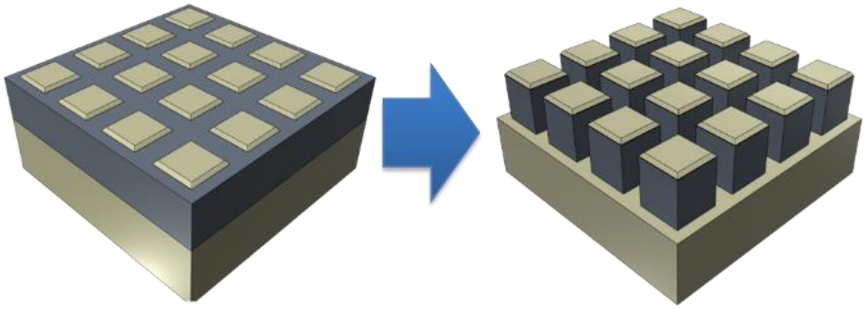

Figure 6.2 – Schematic for two-dimensional device fabrication using ZnS hardmask.

6.2 Additional IR device designs

Several possibilities exist for the implementation of additional wideband MWIR and LWIR GMR reflectors. A MWIR device could be straight forwardly implemented by taking advantage of the relatively low dispersion of Ge and ZnS throughout the IR band through a simple scaling of the device dimensions to fit a new center wavelength of 4 µm. Figure 6.3 shows the calculated spectrum for such a device along with the atmospheric transmission chart highlighting the region where the device would function. With a period Λ = 1470 nm, this device should be readily fabricable using UV interference lithography.

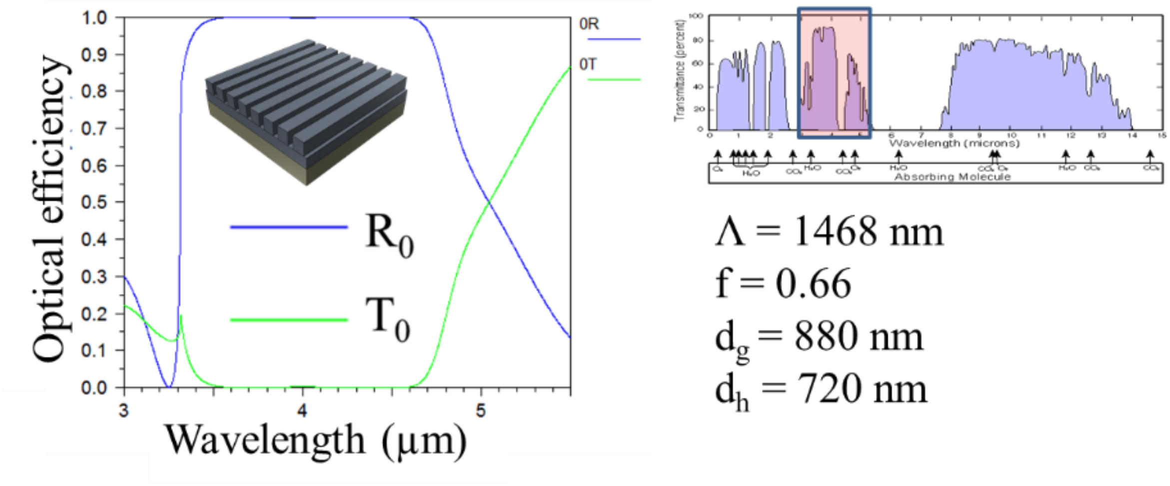

Figure 6.3 – MWIR wideband GMR reflector designed through scaling dimensions of LWIR device.

Another avenue of potential research lies in exploiting the heightened index of refraction measurements of the sputtered germanium films. If the precise mechanism behind the increase in index can be categorized and controlled, it could prove beneficial for a range of devices. Figure 6.4 shows examples of wideband device designs using such a high-index film with static index n = 4.5. The high mode confinement created by the increased index allows for a HCG structure with a bandwidth greater than previously displayed ZCG designs as shown in Fig. 6.4 b), and by working with a ZCG design incorporating the high-index film, a wideband reflector that covers the entire LWIR band is achievable as shown in Fig. 6.4 d). These devices would demonstrate the performance of designs incorporating such high-index materials as PbTe or PbSe, but without the material toxicity concerns.

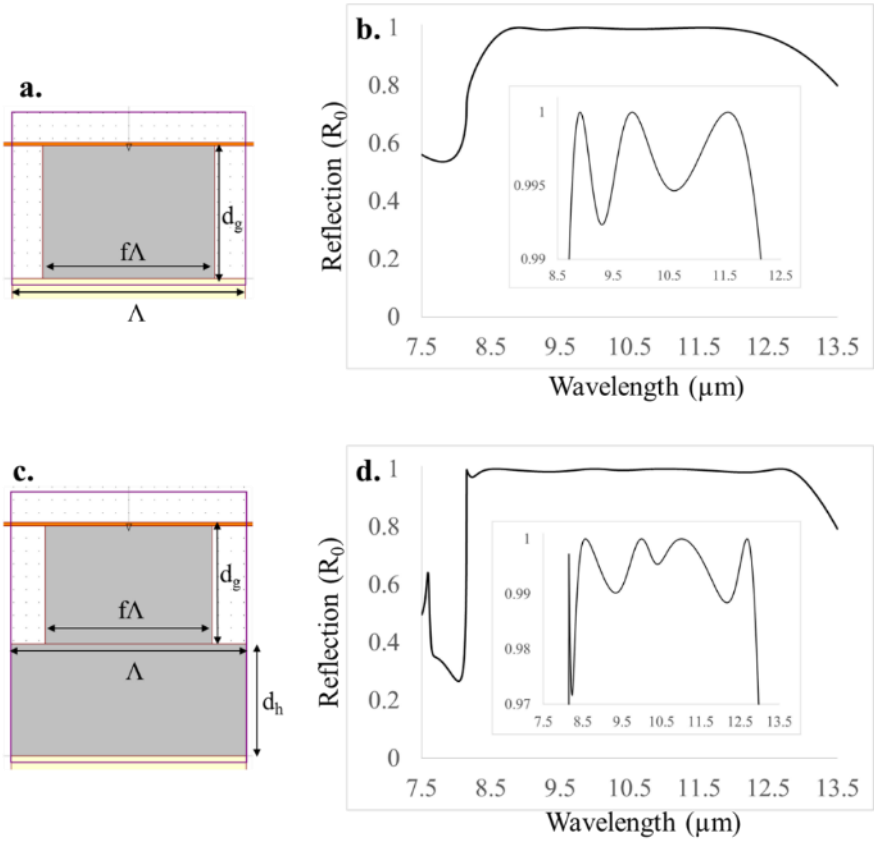

Figure 6.4 – High refractive index grating designs. a) HCG design with d_g = 2.04 μm, Λ = 3.67 μm, f = 0.74. b) HCG spectrum with %BW = 32.8. c) ZCG design with d_g = 1.875 μm, d_h = 1.75 μm, Λ = 3.67 μm, f = 0.71. d) ZCG spectrum covering the entire LWIR with %BW ≈ 50.

6.3 Further plasmonic investigations

The nanocup designs examined also leave room for further investigation into their physical underpinnings. The cavity resonance connection becomes most apparent when one examines a periodic array that goes from being an array of posts to an array of holes as shown in Figure 6.5. Here is shown the absorption spectrum as a function of wavelength and the post height/hole depth. The top half of the graph from s = 0 to s = 2 depicts the absorption spectrum for a 2D array of square gold posts with period Λ = 530 nm, side length d = 273 nm, height s, and assumed to be immersed in water, n = 1.33. The height is decreased moving down the figure such that the center line at s = 0 is representative of a flat gold slab, and the very bottom of the image at s = -2 is the spectrum for a 2D array of 2 μm deep square holes.

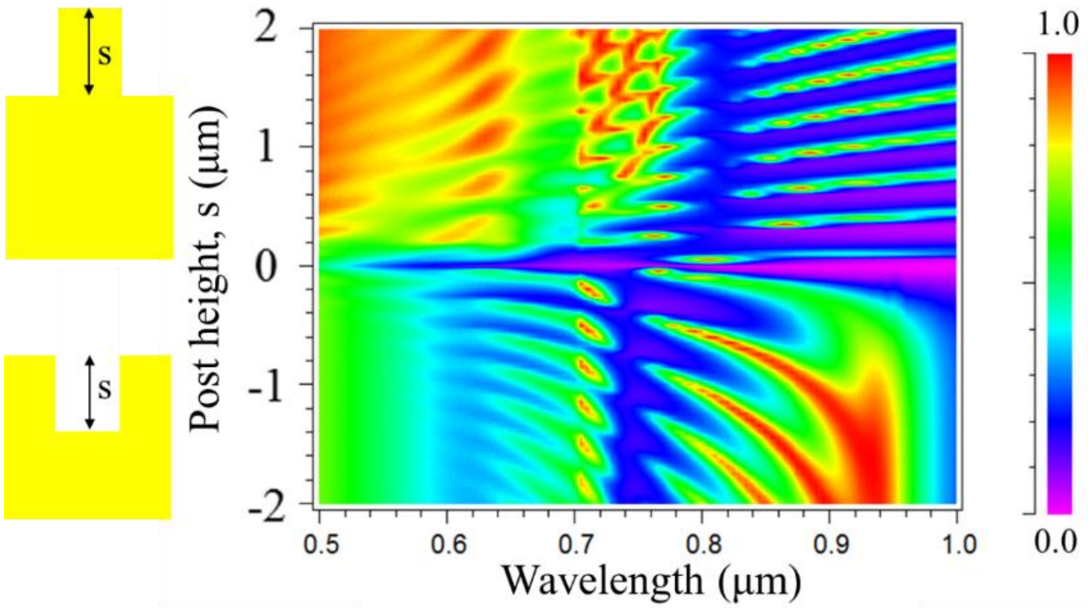

Figure 6.5 – Absorption response of an array of square posts and holes. Positive height corresponds to a post array, negative height corresponds to a hole array.

As is seen, there is a definite periodic effect to the resonant response that is a function of the post height / hole depth. This Fabry-Perot-like response shows a strong connection to the cavity height and cannot be explained purely through plasmonics. The top half of the image likely shows the response to TEM modes propagating between the conductive posts which behave as two-wire transmission lines. The TEM modes form standing waves that account for the response bands showing up after roughly 820 nm. The bottom half shows the response to the evanescently cutoff cavities where not only is there a periodic response, but we see also that the absorption resonances seem to converge at a point centered around 940 nm. The measured response of the nanocup devices in Chapter 5 was for a relatively shallow device and fell within the first arm of the graph at around 0.850 µm and s = -0.180. The complete physics explaining the overall cavity response is as yet unresolved.

6.4 Concluding remarks

The body of this work encompasses the design, modeling, and fabrication of micro- and nano-photonic devices operating through subwavelength guided-mode resonance waveguide gratings and diffractively coupled gold nanocup evanescent cavities. It presents new tools useful for the fabrication of germanium based mid and long wave infrared resonant devices, and offers designs and demonstrated proof of concept for wideband LWIR GMR reflectors. The course of the research also uncovered properties of sputtered germanium films that seem to offer enhanced optical characteristics that may have potential for a range of photonic devices where creating high field confinement is beneficial. Lastly, the work finishes with a study of gold nanocup plasmonics that investigates the connection between the measured resonant response of the devices, previous literature on the subject and newly derived modeling and simulations. And as seen in this chapter, much potential remains for future research and device applications in any number of areas of pursuit.

List of publications and presentations

D. J. Carney and R. Magnusson, “Refractive index of sputtered germanium films in the 2.5-13 μm spectral region,” Optics Materials Express (in progress) (2019)

D. J. Carney, H. G. Svavarsson, H. Hemmati, A. Fannin, J. W. Yoon, and R. Magnusson, “Refractometric Sensing with Periodic Nano-Indented Arrays: Effect of Structural Dimensions,” Sensors 19, 897, (2019)

D. J. Carney and R. Magnusson, “Fabrication methods for infrared resonant devices,” Optics Letters 43, 21, pp. 5198-5201 (2018)

D. J. Carney and R. Magnusson, “Design and Fabrication of Germanium-Zinc Sulfide Mid-IR Photonic Devices,” Frontiers in Optics 2018, 16 – 20 September 2018, Washington, DC

D. J. Carney and R. Magnusson, “Wideband Mid-IR Semiconductor Resonant Reflectors,” 2018 IEEE Research and Applications of Photonics In Defense Conference (RAPID), 22-24 August 2018, MIRAMAR BEACH, FL

D. J. Carney and R. Magnusson, “Ge-ZnS Mid-IR Wideband Resonant Reflectors,” Frontiers in Optics 2017, 17 - 21 September 2017, Washington, DC

D. J. Carney and R. Magnusson, “Broadband Mid-Infrared and Terahertz Band Guided-Mode Resonance Devices,” 3rd Nanosmat-USA 2016, May 18-20, 2016, Arlington, TX

Robert Magnusson, Hafez Hemmati, Daniel John Carney, Kyu Jin Lee, Yeong Hwan Ko, and Sun-Goo Lee, “Fundamentals and applications of resonant leaky-mode photonic lattices,” IEEE Aerospace Conference, 2-9 March 2019, Big Sky, Montana.

Robert Magnusson, Sun-Goo Lee, Kyu J. Lee, Hafez Hemmati, Daniel J. Carney, Pawarat Bootpakdeetam, and Yeong Hwan Ko, "Principles of leaky-mode photonic lattices: Band flips and Bloch mode dynamics," *Proc. SPIE 10921,* Integrated Optics: Devices, Materials, and Technologies XXIII, 109211E (Presented at SPIE OPTO: February 07, 2019; Published: 4 March 2019)

References

[1] F. Cajori, A History of Physics in its elementary branches including the evolution of physical laboratories, London: The Macmillan Company, 1899.

[2] John Wallis, John Flamsteed, Sir Isaac Newton, Isaac Barrow and Augustus De Morgan, Correspondence of Scientific Men of the Seventeenth Century: Including Letters of Barrow, Flamsteed, Wallis, and Newton, Printed from the Originals in the Collection of the Right Honourable the Earl of Macclesfield, Volume 2, University Press, 1841.

[3] D. D. Wawro, P. Priambodo and R. Magnusson, "Resonating periodic waveguides as ultraresolution sensors in biomedicine," in *Proceedings Volume 5515, Nanoengineering: Fabrication, Properties, Optics, and Devices*, Denver, 2004.

[4] J. Homola, I. Koudela and S. S. Yee, "Surface plasmon resonance sensors based on diffraction gratings and prism couplers: sensitivity comparison," *Sensors and Actuators B: Chemical,* vol. 54, no. 1-2, pp. 16-24, 1999.

[5] J. Brand, Lines of Light: The Sources of Dispersive Spectroscopy, 1800-1930, Gordon & Breach, 1995.

[6] G. Roelkens, D. Vermeulen, D. Van Thourhout, R. Baets, S. Brision, P. Lyan, P. Gautier and J. M. Fedeli, "High efficiency diffractive grating couplers for interfacing a single mode optical fiber with a nanophotonic silicon-on-insulator waveguide circuit," *Applied Physics Letters,* vol. 92, no. 13, p. 131101, 2008.

[7] G. Roelkens, D. Van Thourhout and R. Baets, "High efficiency grating coupler between silicon-on-insulator waveguides and perfectly vertical optical fibers," *Optics Letters,* vol. 32, no. 11, pp. 1495-1497, 2007.

[8] I. A. Avrutsky, A. S. Svakhin and V. A. Sychugov, "Interference Phenomena in Waveguides with Two Corrugated Boundaries," *Journal of Modern Optics,* vol. 36, no. 10, pp. 1303-1320, 1989.

[9] Y. H. Ko and R. Magnusson, "Wideband dielectric metamaterial reflectors: Mie scattering or leaky Bloch mode resonance?," *Optica,* vol. 5, no. 3, pp. 289-294, 2018.

[10] Y. Ding and R. Magnusson, "Resonant leaky-mode spectral-band engineering and device applications," *Optics Express,* vol. 12, no. 23, pp. 5661-5674, 2004.

[11] D. Rosenblatt, A. Sharon and A. A. Friesem, "Resonant Grating Waveguide Structures," *IEEE Journal of Quantum Electronics,* vol. 33, no. 11, p. 2038, 1997.

[12] "Infrared window," [Online]. Available: https://en.wikipedia.org/wiki/Infrared_window#/media/File:Atmosfaerisk_spredning.png.

[13] D. Chandler-Horowitz and P. M. Amirtharaj, "High-accuracy, midinfrared (450 cm−1 ≤ ω ≤ 4000 cm−1) refractive index values of silicon," *Journal of Applied Physics,* vol. 97, no. 12, p. 123526, 2005.

[14] Icenogle et al., "Refractive indexes and temperature coefficients of germanium and silicon," *Applied Optics,* vol. 15, no. 10, pp. 2348-2351, 1976.

[15] S. Adachi, "Optical dispersion relations for GaP, GaAs, GaSb, InP, InAs, InSb, AlxGa1−xAs, and In1−xGaxAsyP1−y," *J. Appl. Phys.,* vol. 66, no. 12, pp. 6030-6040, 1989.

[16] J. N. Zemel, J. D. Jensen and R. B. Schoolar, "Electrical and optical properties of epitaxial films of PbS, PbSe, PbTe, and SnTe," *Physical Review,* vol. 140, no. 1A, pp. A330-A342, 1965.

[17] F. Weiting and Y. Yixun, "Temperature effects on the refractive index of lead telluride and zinc selenide," *Infrared Physics,* vol. 30, no. 4, pp. 371-373, 1990.

[18] M. R. Querry, "Optical constants of minerals and other materials from the millimeter to the ultraviolet," *Contractor Report CRDEC-CR-88009,* pp. 71-81, 1987.

[19] L. Rodríguez-de Marcos, J. I. Larruquert, J. A. Aznárez, M. Fernández-Perea, R. Soufli, J. A. Méndez, S. L. Baker and E. M. Gullikson, "Optical constants of SrF2 thin films in the 25–780-eV spectral range," *Journal of Applied Physics,* vol. 113, no. 14, p. 143501, 2013.

[20] H. H. Li, "Refractive index of alkaline earth halides and its wavelength and temperature derivatives," *Journal of Physical and Chemical Reference Data,* vol. 9, no. 1, pp. 161-289, 1980.

[21] Z. Han, V. Singh, D. Kita, C. Monmeyran, P. Becla, P. Su, J. Li, X. Huang, L. C. Kimerling, J. Hu, K. Richardson, D. T. H. Tan and A. Agarwal, "On-chip chalcogenide glass waveguide-integrated mid-infrared PbTe detectors," *Applied Physics Letters,* vol. 109, no. 7, p. 071111, 2016.

[22] W. F. Brinkman, "A History of the Invention of the Transistor and Where It Will Lead Us," *IEEE Journal of Solid-State Circuits,* vol. 32, no. 12, pp. 1858-1865, 1997.

[23] F. Y. Gardes, C. G. Littlejohns, J. Soler Penades, C. J. Mitchell, A. Z. Khokhar, G. T. Reed and G. Z. Mashanovich, "Germanium for photonic applications," in *2014 7th International Silicon-Germanium Technology and Device Meeting (ISTDM)*, Singapore, 2014.

[24] A. A. Zulkefle, M. Zainon, z. Zakaria, S. A. Shahahmadi, M. A. M. Bhuiyan, M. M. Alam, K. Sopian and N. Amin, "Effects of germanium layer on silicon/germanium superlattice solar cells," in *2013 IEEE 39th Photovoltaic Specialists Conference (PVSC)*, Tampa, 2013.

[25] G. H. Wang, C. Y. Shi, L. Zhao, H. W. Diao and W. J. Wang, "Fabrication of amorphous silicon–germanium thin film solar cell toward broadening long wavelength response," *Journal of Alloys and Compounds,* vol. 658, no. 15, pp. 543-547, 2016.

[26] V. Sorianello, L. Colace, C. Maragliano, D. Fulgoni, L. Nash and G. Assanto, "Germanium-on-Glass solar cells: fabrication and characterization," *Optical Materials Express,* vol. 3, no. 2, pp. 216-228, 2013.

[27] D. Wang, T. Maekura, S. Kamezawa, K. Yamamoto and H. Nakashima, "Direct band gap electroluminescence from bulk germanium at room temperature using an asymmetric fin type metal/germanium/metal structure," *Aplied Physics Letters,* vol. 106, no. 7, p. 071102, 2015.

[28] S. Huang, W. Lu, C. Li, W. Huang, H. Lai and S. Chen, "Room temperature photoluminescence from tensile-strained germanium-on-insulator fabricated by a Ge condensation technique," in *Asia Communications and Photonics Conference 2012*, Guangzhou, 2012.

[29] H. T. Chen, P. Verheyen, P. De Heyn, G. Lepage, J. De Coster, P. Absil, G. Roelkens and J. Van Campenhout, "High-Responsivity Low-Voltage 28-Gb/s Ge p-i-n Photodetector With Silicon Contacts," *Journal of Lightwave Technology,* vol. 33, no. 4, pp. 820-824, 2015.

[30] J. Simon, L. Escoubas, M. Lo Monaco, R. Willey, Z. Elalamy, S. Enoch and G. Hugues, "Design and fabrication of infrared anti-reflective Germanium gratings," in *Optical Interference Coatings*, Tucson, 2004.

[31] G. Z. Mashanovich, C. J. Mitchell, J. S. Penades, A. Z. Khokhar, C. G. Littlejohns, W. Cao, Z. Qu, S. Stankovic, F. Y. Gardes, T. Ben Masaud, H. M. H. Chong, V. Mittal, G. Senthil Murugan, J. S. Wilkinson, A. C. Peacock and M. Nedeljkovic, "Germanium Mid-Infrared Photonic Devices," *Journal of Lightwave Technology,* vol. 35, no. 4, pp. 624-630, 2017.

[32] J. Kang, M. Takenaka and S. Takagi, "Novel Ge waveguide platform on Ge-on-insulator wafer for mid-infrared photonic integrated circuits," *Optics Express,* vol. 24, no. 11, pp. 11855-11864, 2016.

[33] T.-H. Xiao, Z. Zhao, W. Zhou, M. Takenaka, H. K. Tsang, Z. Cheng and K. Goda, "High-Q germanium optical nanocavity," *Photonics Research,* vol. 6, no. 9, pp. 925-928, 2018.

[34] T.-H. Xiao, Z. Zhao, W. Zhou, C.-Y. Chang, S. Y. Set, M. Takenaka, H. K. Tsang, Z. Cheng and K. Goda, "Mid-infrared high-Q germanium microring resonator," *Optics Letters,* vol. 43, no. 12, pp. 2885-2888, 2018.

[35] J. A. Aguilera, J. Aguilera, P. Baumeister, A. Bloom, D. Coursen, J. A. Dobrowolski, F. T. Goldstein, D. E. Gustafson and R. A. Kemp, "Antireflection coatings for germanium IR optics: a comparison of numerical design methods," *Applied Optics,* vol. 27, no. 14, pp. 2832-2840, 1988.

[36] I. Hosako, "Antireflection coating formed by plasma-enhanced chemical-vapor deposition for terahertz-frequency germanium optics," *Applied Optics,* vol. 42, no. 19, pp. 4045-4048, 2003.

[37] M. Ritter, M. Stindtmann, K. Farle and K. Baberschke, "Nanostructuring of the Cu(001) surface by ion bombardment: a STM study," *Surface Science,* vol. 348, no. 3, pp. 243-252, 1996.

[38] D. Hegemann, H. Brunner and C. Oehr, "Plasma treatment of polymers for surface and adhesion improvement," *Nuclear Instruments and Methods in Physics Research Section B: Beam Interactions with Materials and Atoms,* vol. 208, pp. 281-286, 2003.

[39] H. Hemmati and R. Magnusson, "Development of tuned refractive-index nanocomposites to fabricate nanoimprinted optical devices," *Optical Materials Express,* vol. 8, no. 1, pp. 175-183, 2018.

[40] Y. J. Kaufman, "Operational remote sensing of tropospheric aerosol over land from EOS moderate resolution imaging spectroradiometer," *Journal of Geophysical Research,* vol. 102, no. D14, p. 17051– 17067, 1997.

[41] D. Ouzounov and F. Freund, "Mid-infrared emission prior to strong earthquakes analyzed by remote sensing data," *Advances in Space Research,* vol. 33, no. 3, pp. 268-273, 2004.

[42] S. Sugawara, Y. Nakayama, H. Taniguchi and I. Ishimaru, "Wide-field mid-infrared hyperspectral imaging of adhesives using a bolometer camera," *Scientific Reports,* vol. 7, no. 12395, pp. 1-7, 2017.

[43] A. Pope, R. Chary, D. M. Alexander, L. Armus, M. Dickinson, D. Elbaz, D. Frayer, D. Scott and H. Teplitz, "Mid-Infrared Spectral Diagnosis of Submillimeter Galaxies," *The Astrophysical Journal,* vol. 675, no. 2, pp. 1171-1193, 2008.

[44] Strategies Unlimited, "Mid-IR Lasers Market Review and Forecast 2010," Strategies Unlimited, Mountain View, 2010.

[45] V. A. Serebryakov, É. V. Boĭko, N. N. Petrishchev and A. V. Yan, "Medical applications of mid-IR lasers. Problems and prospects," *Journal of Optical Technology,* vol. 77, no. 1, pp. 6-17, 2010.

[46] B. Jean and T. Bende, "Mid-IR Laser Applications in Medicine," in *Solid-State Mid-Infrared Laser Sources (Topics in Applied Physics),* Springer, 2003, p. 511.

[47] P. Werle, F. Slemr, K. Maurer, R. Kormann, R. Mücke and B. Jänker, "Near- and mid-infrared laser-optical sensors for gas analysis," *Optics and Lasers in Engineering,* vol. 37, no. 2-3, pp. 101-114, 2002.

[48] A. V. Kildishev, A. Boltasseva and V. M. Shalaev, "Planar Photonics with Metasurfaces," *Science,* vol. 339, no. 6125, p. 1232009, 2013.

[49] R. Magnusson, "Wideband reflectors with zero-contrast gratings," *Optics Letters,* vol. 39, no. 15, pp. 4337-4340, 2014.

[50] Y. Ding and R. Magnusson, "Resonant leaky-mode spectral-band engineering and device applications," *Optics Express,* vol. 12, no. 23, pp. 5661-5674, 2004.

[51] L. Verslegers, P. B. Catrysse, Z. Yu, J. S. White, E. S. Barnard, M. L. Brongersma and S. Fan, "Planar Lenses Based on Nanoscale Slit Arrays in a Metallic Film," *Nano Letters,* vol. 9, no. 1, pp. 235-238, 2009.

[52] K. J. Lee, J. Curzan, M. Shokooh-Saremi and R. Magnusson, "Resonant wideband polarizer with single silicon layer," *Optics Letters,* vol. 41, no. 21, pp. 5130-5133, 2016.

[53] Y. Zhao, M. A. Belkin and A. Alù, "Twisted optical metamaterials for planarized ultrathin broadband circular polarizers," *Nature Communications,* vol. 3, no. 870, pp. 1-7, 2012.

[54] Y. Ding and R. Magnusson, "Doubly resonant single-layer bandpass optical filters," *Optics Letters,* vol. 29, no. 10, pp. 1135-1137, 2004.

[55] P. Sah and B. K. Das, "Photonic bandpass filter characteristics of multimode SOI waveguides integrated with submicron gratings," *Applied Optics,* vol. 57, no. 9, pp. 2277-2281, 2018.

[56] M. Niraula, J. W. Yoon and R. Magnusson, "Single-layer optical bandpass filter technology," *Optics Letters,* vol. 40, no. 21, pp. 5062-5065, 2015.

[57] Y. H. Ko and R. Magnusson, "Flat-top bandpass filters enabled by cascaded resonant gratings," *Optics Letters,* vol. 41, no. 20, pp. 4704-4707, 2016.

[58] B. Hogan, S. P. Hegarty, L. Lewis, J. Romero-Vivas, T. J. Ochalski and G. Huyet, "Realization of high-contrast gratings operating at 10 μm," *Optics Letters,* vol. 41, no. 21, p. 5130, 2016.

[59] M. L. Lee, J. Rodier, P. Lalane, P. Gallais, C. Germain and J. Rollin, "Blazed-binary diffractive gratings with antireflection coating for improved operation at 10.6 μm," *Optical Engineering,* vol. 43, no. 11, pp. 2583-2588, 2004.

[60] R. Magnusson and M. Shokooh-Saremi, "Physical basis for wideband resonant reflectors," *Optics Express,* vol. 16, no. 5, pp. 3456-3462, 2008.

[61] M. Shokooh-Saremi and R. Magnusson, "Particle swarm optimization and its application to the design of diffraction grating filters," *Optics Letters,* vol. 32, no. 8, pp. 894-896, 2007.

[62] V. Karagodsky, F. G. Sedgwick and C. J. Chang-Hasnain, "Theoretical analysis of subwavelength high contrast grating reflectors," *Optics Express,* vol. 18, no. 16, pp. 16973-16988, 2010.

[63] R. Magnusson, "Wideband reflectors with zero-contrast gratings," *Optics Letters,* vol. 39, no. 15, pp. 4337-4340, 2014.

[64] Z. Iqbal and S. Veprek, "Raman scattering from hydrogenated microcrystalline and amorphous silicon," *Journal of Physics C: Solid State Physics,* vol. 15, no. 2, p. 377, 1982.

[65] F. Greuter and G. Blatter, "Electrical properties of grain boundaries in polycrystalline compound semiconductors," *Semiconductor Science and Technology,* vol. 5, no. 2, p. 111, 1990.

[66] S. Heiroth, R. Ghisleni, T. Lippert, J. Michler and A. Wokaun, "Optical and mechanical properties of amorphous and crystalline yttria-stabilized zirconia thin films prepared by pulsed laser deposition," *ScienceDirect,* vol. 59, no. 6, pp. 2330-2340, 2011.

[67] M. S. Amin, N. Hozhabri and R. Magnusson, "Effects of solid phase crystallization by rapid thermal annealing on the optical constants," *Thin Solid Films,* vol. 545, pp. 480-484, 2013.

[68] E. Pihan, A. Slaoui, P. Roca i Cabarrocas and A. Focsa, "Polycrystalline silicon films by aluminium-induced crystallisation: growth process vs. silicon deposition method," *Thin Solid Films,* Vols. 451-452, pp. 328-333, 2004.

[69] H. Matsumura, "Formation of Polysilicon Films by Catalytic Chemical Vapor Deposition (cat-CVD) Method," *Japanese Journal of Applied Physics,* vol. 30, no. 2, 8B, pp. 1522-1524, 1991.

[70] P. Roy, J. R. Ota and S. K. Srivastava, "Crystalline ZnS thin films by chemical bath deposition

method and its characterization," *Thin Solid Films,* vol. 515, no. 4, pp. 1912-1917, 2006.

[71] R. B. Bergmann, "Crystalline Si thin-film solar cells: a review," *Applied Physics A Materials Science & Processing,* vol. 69, no. 2, pp. 187-194, 1999.

[72] L. J. Pilione, K. Vedam, J. E. Yehoda and R. Messier, "Thickness dependence of optical gap and void fraction for sputtered amorphous germanium," *Physical Review B,* vol. 35, no. 17, pp. 9368-9371, 1987.

[73] J. C. G. de Sande, C. N. Afonso, J. L. Escudero, R. Serna, F. Catalina and E. Bernabeu, "Optical properties of laser-deposited a-Ge films: a comparison with sputtered and e-beam-deposited films," *Applied Optics,* vol. 31, no. 28, pp. 6133-6138, 1992.

[74] J. R. Blanco, P. J. McMarr, J. E. Yehoda, K. Vedam and R. Messier, "Density of amorphous germanium films by spectroscopic ellipsometry," *Journal of Vacuum Science & Technology A,* vol. 4, no. 3, p. 577, 1986.

[75] R. Magnusson, D. Wawro, S. Zimmerman and Y. Ding, "Resonant Photonic Biosensors with Polarization-Based Multiparametric Discrimination in Each Channel," *Sensors,* vol. 11, no. 2, pp. 1476-1488, 2011.

[76] A. Perot and C. Fabry, "On the application of interference phenomena to the solution of various problems of spectroscopy and metrology," *Astrophysical Journal,* vol. 9, p. 87, 1899.

[77] H. E. Swanson and R. K. Fuyat, "Standard X-ray Diffraction Patterns," *NBS Circular,* vol. 539, pp. 16-21, 1953.

[78] Z. P. Lu, C. T. Liu, J. R. Thompson and W. D. Porter, "Structural Amorphous Steels," *Physical Review Letters,* vol. 92, no. 24, p. 245503, 2004.

[79] S. Q. Ren, L. Q. Weng, S. H. Song, F. Li, J. G. Wan and M. Zeng, "BaTiO3/CoFe2O4 particulate composites with large high frequency magnetoelectric response," *Journal of Materials Science,* vol. 40, no. 16, pp. 4375-4378, 2005.

[80] B. Liedberg, C. Nylander and I. Lundstrom, "Surface Plasmon Resonance for Gas Detection and Biosensing," *Sensors and Actuators,* vol. 4, pp. 299-304, 1983.

[81] C. Nylander, B. Liedberg and T. Lind, "Gas Detection by Means of Surface Plasmon Resonance," *Sensors and Actuators,* vol. 3, pp. 79-88, 1982.

[82] R. H. Ritchie, "Plasma Losses by Fast Electrons in Thin Films," *Physical Review,* vol. 106, no. 5, p. 874, 1957.

[83] E. Kretschman and H. Raether, "Radiative decay of nonradiative surface plasmons excited by light," *Zeitschrift für Naturforschung A,* vol. 23, no. 12, p. 2135–2136, 1968.

[84] A. Otto, "Excitation of nonradiative surface plasma waves in silver by the method of frustrated total reflection," *Zeitschrift für Physik,* vol. 216, no. 4, p. 398, 1968.

[85] B. Hecht, H. Bielefeldt, L. Novotny, Y. Inouye and D. W. Pohl, "Local Excitation, Scattering, and Interference of Surface Plasmons," *Physical Review Letters,* vol. 77, no. 9, pp. 1889-1892, 1996.

[86] R. H. Ritchie, E. T. Arakawa, J. J. Cowan and R. N. Hamm, "SURFACE-PLASMON RESONANCE EFFECT IN GRATING DIFFRACTION," *Physical Review Letters,* vol. 21, no. 22, pp. 1530-1533, 1968.

[87] J. M. Pitarke, V. M. Silkin, E. V. Chulkov and P. M. Echenique, "Theory of surface plasmons and surface-plasmon polaritons," *Reports on Progress in Physics,* vol. 70, no. 1, pp. 1-87, 2007.

[88] D. J. Carney, H. G. Svavarsson, H. Hemmati, A. Fannin, J. W. Yoon and R. Magnusson, "Refractometric Sensing with Periodic Nano-Indented Arrays: Effect of Structural Dimensions," *Sensors,* vol. 19, no. 4, p. 897, 2019.

[89] H. G. Svavarsson, J. W. Yoon, M. Shokooh-Saremi and R. Magnusson, "Fabrication and characterization of large, perfectly periodic arrays of metallic nano cups," *Plasmonics,* vol. 7, no. 4, pp. 653-657, 2012.

[90] H. G. Svavarsson, J. W. Yoon, M. Shokoh-Saremi, S. H. Song and R. Magnusson, "Fabrication of large plasmonic arrays of gold nanocups using inverse periodic templates," *Plasmonics,* vol. 6, pp. 741-744, 2011.

[91] F. J. Garcia-Vidal, L. Martin-Moreno, T. W. Ebbesen and L. Kuipers, "Light passing through subwavelength apertures," *Reviews of Modern Physics,* vol. 82, no. 1, pp. 729-787, 2010.

[92] F. J. Garcia-Vidal, L. Martin-Moreno and J. B. Pendry, "Surfaces with holes in them: New plasmonic metamaterials," *Journal of Optics A: Pure and Applied Optics,* vol. 7, no. 2, pp. 97-101, 2005.

[93] P. Lalanne, J. C. Rodier and J. P. Hugonin, "Surface plasmons of metallic surfaces perforated by nanohole arrays," *Journal of Optics A: Pure and Applied Optics,* vol. 7, no. 8, pp. 422-426, 2005.

[94] P. Drude, "Zur Elektronentheorie der Metalle," *Annalen der Physik,* vol. 306, no. 3, p. 566, 1900.

[95] J. B. Pendry, L. Martin-Moreno and F. J. Garcia-Vidal, "Mimicking Surface Plasmons with Structured Surfaces," *Science,* vol. 305, no. 5685, pp. 847-848, 2004.

[96] M. Padmanaban, J. Cho, T. Kudo, D. Rahman, H. Yao, K. Yamamoto, Y. Cao and Y. Her, "Progress in Spin-on Hard Mask Materials for," *Journal of Photopolymer Science and Technology,* vol. 27, no. 4, pp. 503-509, 2014.

[97] L. Li, I. Bayn, M. Lu, C. Nam, T. Schroder, A. Stein, N. C. Harris and D. Englund, "Nanofabrication on unconventional substrates using transferred hard masks," *Scientific Reports,* vol. 5, no. 7802, pp. 1-6, 2015.

[98] A. Iwasaki, K. Courouble, S. Lippy, F. Buisine, H. Ishikawa, E. Cooper, E. Kennedy, S. Zoll and L. Broussous, "Industrial Challenges of TiN Hard Mask Wet Removal Process for 14nm Technology Node," *Solid State Phenomena,* pp. 213-216, 26 September 2014.